



**Bruno Jordão Lopes**

**Comparing Ultrasound and Shearography  
inspections as methods to monitor and predict  
long-term damage propagation of composite  
pipeline repairs**

**Tese de Doutorado**

Thesis presented to the Programa de Pós-graduação em Engenharia de Materiais e de Processos Químicos e Metalúrgicos of PUC-Rio in partial fulfillment of the requirements for the degree of Doutor em Engenharia de Materiais e de Processos Químicos e Metalúrgicos.

Advisor: Prof. José Roberto Moraes d'Almeida

Co-advisor: Prof. Daniel Carlos Taissum Cardoso

Rio de Janeiro

May 2023



**Bruno Jordão Lopes**

**Comparing Ultrasound and Shearography inspections as methods to monitor and predict long-term damage propagation of composite pipeline repairs**

Thesis presented to the Programa de Pós-graduação em Engenharia de Materiais e de Processos Químicos e Metalúrgicos of PUC-Rio in partial fulfillment of the requirements for the degree of Doutor em Engenharia de Materiais e de Processos Químicos e Metalúrgicos. Approved by the Examination Committee.

**Prof. José Roberto Moraes d'Almeida**

Advisor

Departamento de Engenharia Química e de Materiais – PUC-Rio

**Prof. Daniel Carlos Taissum Cardoso**

Co-advisor

Departamento de Engenharia Civil e Ambiental – PUC-Rio

**Dr. Mauro Eduardo Benedet**

UFSC

**Dra. Ana Lúcia Fampa Seabra d'Almeida**

Petroleo Brasileiro S.A.

**Dr. Cesar Giron Camerini**

COPPE/UFRJ

**Prof. Norberto Cella**

IPRJ/UERJ

**Dr. Lucio Rossi de Souza**

Departamento de Ciência e Engenharia Macromolecular – Case Western Reserve University (CWRU)

Rio de Janeiro, May 2<sup>th</sup>, 2023

Todos os direitos reservados. A reprodução, total ou parcial do trabalho, é proibida sem a autorização da universidade, do autor, do orientador e do co-orientador.

## **Bruno Jordão Lopes**

Graduated in Mechanical Engineering at the Rio de Janeiro State University (UERJ) in 2015 and obtained his M.Sc. Degree in Materials Engineering from the Pontifical University of Rio de Janeiro (PUC-Rio) in 2018.

### Bibliographic data

Lopes, Bruno Jordão

Comparing ultrasound and shearography inspections as methods to monitor and predict long-term damage propagation of composite pipeline repairs / Bruno Jordão Lopes ; advisor: José Roberto Moraes d'Almeida ; co-advisor: Daniel Carlos Taissum Cardoso. – 2023.

128 f. : il. color. ; 30 cm

Tese (doutorado)–Pontifícia Universidade Católica do Rio de Janeiro, Departamento de Engenharia Química e de Materiais, 2023.

Inclui bibliografia

1. Engenharia Química e de Materiais – Teses. 2. Reparos em tubos. 3. Shearografia. 4. Ultrassom. 5. Materiais compósitos. 6. Envelhecimento acelerado. I. Almeida, José Roberto Moraes d'. II. Cardoso, Daniel Carlos Taissum. III. Pontifícia Universidade Católica do Rio de Janeiro. Departamento de Engenharia Química e de Materiais. IV. Título.

CDD: 620.11

For Bet, André,  
Fernando, Therezinha, Martha,  
D'artagnan & Kimi.

## Acknowledgements

To my advisor d'Almeida, for almost a decade of guidance and patience. Thank you for believing in me. The main reason to finish this thesis was to not let you down.

To my co-advisor and boss Daniel, for all the guidance, knowledge shared and understanding throughout both this thesis and the research project. I've learnt so much.

To Giulia for your relentless support and partnership.

To my colleagues, past and present, at the Composite Materials Laboratory who helped me so much during this time. This thesis would not have happened without you!

To the teams at BAWSF and LNDC for being such good professionals and human beings.

To CENPES/Petrobras for believing in our small team and your continued support.

To my family for all the support, patience and confidence in me.

To Ju, wherever you may be, you are part of this and very much missed.

To my godmother Martha, for everything.

To my father. I wish you were here.

This study was financed in part by the Coordenação de Aperfeiçoamento de Pessoal de Nível Superior - Brasil (CAPES) - Finance Code 001.

## Abstract

Lopes, Bruno Jordão; d'Almeida, José Roberto Moraes (Advisor); Cardoso, Daniel Carlos Taissum (Co-advisor). **Comparing Ultrasound and Shearography inspections as methods to monitor and predict long-term damage propagation of composite pipeline repairs.** Rio de Janeiro, 2023. 128p. Tese de Doutorado – Departamento de Engenharia Química e de Materiais, Pontifícia Universidade Católica do Rio de Janeiro.

Pipeline integrity is one of the key aspects for safe and efficient operation of offshore structures. Pipeline failures can result in significant economic and environmental consequences, making pipeline integrity management a top priority for the industry. One of the most effective tools for managing in-service pipelines is non-destructive testing (NDT). In this study, ultrasound and shearography inspections were performed on composite pipeline repairs over the course of approximately two years and their results were compared. The test samples evaluated were steel pipes with composite repairs and were submitted to just over 13,500 hours of salt-spray accelerated ageing, under three different temperatures. Test samples were removed from the salt-spray chambers at regular intervals and inspected by using field inspection apparatus. The results showed that both techniques provided consistent results between each inspection, although not always being consistent with each other. Maps comparing detections and accuracy of each technique were provided. The feasibility of each technique as a field tool for monitoring pipeline integrity was also evaluated with positive results. Furthermore, a modified Arrhenius methodology was proposed as a first step towards predicting long-term damage propagation.

## Keywords

Pipeline repairs; Shearography; Ultrasound; Composite Materials; Accelerated Ageing

## Resumo

Lopes, Bruno Jordão; d'Almeida, José Roberto Moraes; Cardoso, Daniel Carlos Taissum. **Comparando Ultrassom e Shearografia como ferramentas para monitorar e prever a propagação a longo prazo de danos em reparos compósitos em tubos.** Rio de Janeiro, 2023. 128p. Tese de Doutorado – Departamento de Engenharia Química e de Materiais, Pontifícia Universidade Católica do Rio de Janeiro.

A integridade de tubulações é um dos aspectos-chave para a operação segura e eficiente das estruturas *offshore*. Falhas em tubulações podem resultar em consequências econômicas e ambientais significativas, tornando a gestão da integridade de tubulações uma prioridade importante para a indústria. Uma das ferramentas mais eficazes para gerenciar tubulações em serviço é através de testes não destrutivos (NDT, na sigla em inglês). Neste estudo, inspeções de ultrassom e shearografia foram realizadas em tubulações metálicas com reparos compósitos ao longo de aproximadamente dois anos e seus resultados foram comparados. As amostras de tubos de aço com reparos compósitos foram submetidas a pouco mais de 13.500 horas de envelhecimento acelerado por névoa salina, em três diferentes temperaturas. As amostras foram removidas das câmaras de névoa salina em intervalos regulares e inspecionadas usando aparelhos de inspeção em campo. Os resultados mostraram que ambas as técnicas forneceram resultados consistentes entre cada inspeção, embora nem sempre fossem consistentes entre si. Mapas comparando as detecções e a precisão de cada técnica foram fornecidos. A viabilidade de cada técnica como ferramenta de campo para monitorar a integridade das tubulações também foi avaliada com resultados positivos. Além disso, uma metodologia de Arrhenius modificada foi proposta como um primeiro passo para prever a propagação de danos a longo prazo.

## Palavras-chave

Reparos em tubos; Shearografia; Ultrassom; Materiais Compósitos; Envelhecimento Acelerado

## Table of Contents

|  |    |
|--|----|
| 1. Introduction  | 17 |
| 1.1. Objectives  | 22 |
| 2. Literature Review   | 23 |
| 2.1. Composite Materials   | 23 |
| 2.2. Composite pipeline repair systems                               | 26 |
| 2.2.1. Fiber Reinforced Polymer (FRP) repairs degradation mechanisms | 28 |
| 2.3. Salt Spray Accelerated Ageing                                   | 34 |
| 2.4. Shearography  | 37 |
| 2.5. Ultrasound  | 43 |
| 3. Materials and Methods   | 47 |
| 3.1. Fabrication of test pipes                                       | 47 |
| 3.1.1. Reference pipe fabrication                                    | 50 |
| 3.2. Salt Spray ageing   | 52 |
| 3.3. NDT Calibration procedures                                      | 56 |
| 3.3.1. Shearography  | 56 |
| 3.3.2. Ultrasound  | 59 |
| 4. Results and Discussion  | 66 |
| 4.1. NDT Inspections   | 67 |
| 4.1.1. Reference Pipe  | 67 |
| 4.1.2. Aged Pipes Monitoring   | 69 |
| 4.1.2.1. Shearography  | 71 |

|                                      |     |
|--------------------------------------|-----|
| 4.1.2.2. Ultrasound                  | 80  |
| 4.1.3. Comparison                    | 86  |
| 4.2. Life in service prediction      | 91  |
| 5. Conclusions                       | 98  |
| 6. Proposals for Future Developments | 100 |
| 7. References                        | 102 |
| Appendix A                           | 119 |

## List of Figures

- Figure 1: Technician applying a composite repair to a pipeline in an offshore vessel. The composite material is wrapped around the defective section of pipe, after the surface has been cleaned and prepared. The technician applies layers of the repair material until the desired thickness is reached. Source: [10] 18
- Figure 2: Corrosion beneath the repaired area after removal of the composite wrap. The green area is where the composite repair was applied and the red arrows show the corrosion propagation that lead to the repair being reprovved upon NDT inspection. Source: BAWSF, used with permission. 19
- Figure 3: Ultrasound inspection in a composite part, using a field deployable equipment. The technique has been used with composite materials with success, showing potential to work as a tool to monitor composite repairs as well. Source: [21] 20
- Figure 4: Classic representation of a composite material. Dispersed and matrix phases are represented in different configurations of orientation, distribution and shapes. The dispersed phase arrangement is very important for the final properties of the composite and it is a very important aspect to be considered in the design and/or material selection stages. Adapted from Callister [7]. 24
- Figure 5: Ashby plot of different families of materials. Composites show comparatively high moduli while having density in the same magnitude as polymers or elastomers. Source: Granta Design (<https://www.grantadesign.com/education/students/charts/>) 25
- Figure 6: Ferrari SF-23 Formula 1 car. In a modern F1 car, composites are widely used because of its lightweight and high performance. Most of the bodywork, aero, suspension and even parts of the engine are made out of carbon fiber reinforced composites. Furthermore, brake discs use high temperature carbon reinforced ceramic matrix composites that can withstand continuous 1000 °C+ temperatures. Source: Ferrari.com 26
- Figure 7: Flowchart of the decision making process involved in repairing a pipeline. After initial inspection, in the case of damage detection, a sequence of decisions must be made. Adapted from [20]. 27
- Figure 8: Effects of moisture uptake in a fiber-reinforced composite material, such as a FRP repair - Adapted from Vieira et al [54]. 30
- Figure 9: Comparison between three proposed methods by Wang et al. a) Arrhenius-based model; b) Phani-Bose model with property retention reaching zero; Phani-Bose model with property retention reaching a stable threshold at infinity. Source: Wang et al. [78]. 34

- Figure 10: Typical salt-spray test equipment. Source: Equilam 35
- Figure 11: Steel/composite double-lap shear samples after being through salt-spray testing. Source: [2] 36
- Figure 12: Shearography setup, adapted from [93]. The main components of the setup are the laser source, the modified interferometer, the camera, the computer with dedicated software and a device to stress the sample. 38
- Figure 13: Example of an area of unadhered composite and metallic substrate, a typical use case for shearography inspections [13]. 39
- Figure 14: a) Pair of laterally dislocated images; b) phase map constructed using 4 pairs of laterally dislocated images; c) interferogram showing in red fringe interference patterns that indicate a rectangular shaped defect. Source: BAWSF, used with permission. 41
- Figure 15: Example of a pipe bend: a) image of the repaired pipe bend; b) shearography image showing three kinds of fringe patterns indicating defects. Source: BAWSF Archive – Used with permission. 42
- Figure 16: Shearography fringe patterns overlaid on a test subject. The technique detected flaws in a composite elevator flap, from an Airbus A330 aircraft, previously inspected by thermography. Drawn markings indicate thermography detections. Source: Author's own archive. 42
- Figure 17: The reflected signal strength is displayed versus the time from signal generation to when an echo was received. Adapted from [19] 44
- Figure 18: A-Scan signal with a gate set at the red marked region. The gate is set, in this case, between the front and back echoes, which represent the upper and bottom surfaces of the sample, respectively, in order to detect internal damages in the material. Adapted from [111]. 45
- Figure 19: Simplified flowchart of the experimental program. 47
- Figure 20: Some of the steps of applying a composite repair to a steel pipe: a) preparing the surface: removing paint and corrosion with a plastic pipe insert used as support; b) applying a discrete adhesive layer; c) applying the wrap; d) finished pipe with repair. Source: author's own archive. 49
- Figure 21: Artificial defect map. The Y axis represents the edges of the repaired area, while the X axis represents the length of the repair. 51
- Figure 22: Artificial defects positioned on the surface of the steel pipe, according the artificial defect map. 52
- Figure 23: 3 large-scale salt-spray chambers, with the respective control panels in the foreground. In the background, it is possible to observe the solution tanks next to one of the air/water saturators. 53
- Figure 24: Pipes positioned inside one of the chambers. The samples marked by the red parallelograms are from the same manufacturer and

- were the ones used for this work. It is also possible to see the black end protection on each one. 55
- Figure 25: Shearography setup with most of the componentes displayed. Only the LASER source and the lamp used for thermal loading are not shown in this image. 57
- Figure 26: Positioning of the specimen in relation to the originally acquired images and the directions of the lateral displacements used. 58
- Figure 27: Ultrasound inspection setup: a) Pipe support with water being used as coupling medium being pumped from below; b) Omniscan MX2 data acquisition device. 61
- Figure 28: A-Scan obtained from defect free areas of the repair. In yellow, red and green are the gates selected for analysis. In blue is the region of the signal that represents the water/composite interface. 62
- Figure 29: A-Scan representation of the area indicated in red, in the C-Scan: a) Area in the C-Scan showing no defects appears as an amplitude valley in the indicated area of the A-Scan; b) Area in the C-Scan showing defects appears as an amplitude peak in the indicated area of the A-Scan. 64
- Figure 30: Steel pipes with FRP repairs in different states of degradation after salt-spray ageing: left: unaged pipe; middle: pipe conditioned for approx. 3.400h at 55°C; pipe conditioned for the same amount of time, but at 70°C showing signs of higher degradation. 66
- Figure 31: Ultrasound and shearography results overlaid in the artificial defect map. The numbers inside the indications represent the area of each defect in mm<sup>2</sup>. 68
- Figure 32: Samples used for water uptake measurements. 69
- Figure 33: Mass gain % as a function of time. Chambers 2 and 3 reached saturation before chamber 1. 70
- Figure 34: Example of a sample (#2) with the three different defect indications seen in shearography inspection: red markings indicate defective areas; yellow markings indicate potential defective areas; blue markings indicate minor surface defects. 72
- Figure 35: Shearography results showing the evolution of detections through time. Grey dashed lines represent past detections, while red dashed lines represent the last inspection performed. Blue dashed lines are surface defects. (a) Pipe 6, position 240°; (b) Pipe 7, position 0°; (c) Pipe 12, position 0° - blue arrow at the bottom indicates an area of possible defect detections in the future, based on fringe movements; d) Pipe 16, position 240°. 79

|   |    |
|---|----|
| Figure 36: Ultrasound image processing workflow: a) C-Scan straight out of the equipment; b) binarized image; c) binarized image with defect indications.   | 81 |
| Figure 37: Comparison between UT and SH detections at a) T0; b) T9.   | 87 |
| Figure 38: Evolution of detections for pipe number 6 as seen by Shearography, in orange, and Ultrasound, in blue. Numbers inside indications represent the defective area in mm <sup>2</sup> .  | 90 |
| Figure 39: Experimental data and fitted curves for property retentions as a function of time in: a) UT inspection; b) SH inspection. The points for chambers 1 and 2 are almost completely overlapped, due to the similarity of the undamaged area retention values for both. | 93 |
| Figure 40: $S_{\infty}$ and $\tau$ plots based on data from: a) UT inspection; b) SH inspection   | 95 |
| Figure 41: Property retention tool for DLS samples calculating both retention as a function of temperature and time and time to reach a certain retention as a function of temperature.   | 96 |
| Figure 42: Initial attempts at developing a property retention tool for effective repair length, based on the Phani-Bose methodology.   | 97 |

## List of Tables

|   |    |
|---|----|
| Table 1: Steel pipe and repair nominal dimensions.  | 48 |
| Table 2: Composite laminate properties. Data obtained from the Type Approval process carried out by the American Bureau of Shipping (ABS) and provided by the manufacturer.   | 49 |
| Table 3: Measurements of the repaired pipe samples as fabricated. Measurements made by BAWSF before shearography inspection at T0. Listed are the samples which were aged, thus excluding pipe 0 (reference, not aged) and pipe 4, which was discarded. | 50 |
| Table 4: Set, average temperature and standard deviation for each salt spray chamber.   | 53 |
| Table 5: Salt spray preparation parameters reference values.  | 54 |
| Table 6: Maximum allowable amounts of impurities in the sodium chloride compositions.   | 54 |
| Table 7: Intervals between NDT inspections and accumulated ageing time.   | 55 |
| Table 8: Samples and their respective chambers.   | 55 |
| Table 9: Software, equipment and loading parameters.  | 56 |
| Table 10: Results for each technique segmented by defect size and position. Units in mm.  | 67 |
| Table 11: Shearography defect detections pre-ageing in samples to be conditioned in chamber 1.  | 73 |
| Table 12: Shearography defect detections pre-ageing in samples to be conditioned in chamber 2.  | 73 |
| Table 13: Shearography defect detections pre-ageing in samples to be conditioned in chamber 3.  | 73 |
| Table 14: Shearography detections during periodic inspections.  | 75 |
| Table 15: Ultrasound defect detections in pipes pre-ageing, for pipes to be conditioned in chamber 1.   | 82 |
| Table 16: Ultrasound defect detections in pipes pre-ageing, for pipes to be conditioned in chamber 2.   | 82 |
| Table 17: Ultrasound defect detections in pipes pre-ageing, for pipes to be conditioned in chamber 3.   | 83 |
| Table 18: Ultrasound detection during periodic inspections in chamber 1.  | 84 |
| Table 19: Ultrasound detection during periodic inspections in chamber 2.  | 85 |
| Table 20: Ultrasound detection during periodic inspections in chamber 3.  | 85 |

|   |    |
|---|----|
| Table 21: NDT quantitative analysis.  | 91 |
| Table 22: Average remaining area and property retention over time for UT inspected samples. | 92 |
| Table 23: Average remaining area and property retention over time for SH inspected samples. | 92 |
| Table 24: Phani-Bose model parameters for Shearography and Ultrasound inspected samples.    | 94 |
| Table 25: Linear regression parameters and $R^2$ for $S_{\infty}$ and $\tau$ in each NDT.   | 95 |

*And all that is now  
And all that is gone  
And all that's to come*

*And everything under the sun is in tune  
But the sun is eclipsed by the moon*

*Pink Floyd, Eclipse*

## 1. Introduction

Pipelines are critical to most operations in the oil and gas industry, transporting liquid hydrocarbons, gases and liquids from production sites to refineries and other facilities. Pipeline repair failures can result in significant economic and environmental consequences, making pipeline integrity management a top priority for the industry [1].

Traditional pipeline repair methods, such as welding, have been widely used for decades, but have limitations. Welding requires skilled labor, is time-consuming, can be expensive, and dangerous especially for offshore pipelines [2]. The development of new repair technologies, has therefore become crucial for the industry to increase pipeline safety, reduce downtime, and minimize repair costs.

Composite materials have emerged as a promising technology for pipeline repairs due to their high strength-to-weight ratio, corrosion resistance, and durability [3–6]. Composite materials are made of two or more constituent materials with different physical or chemical properties, combined to create a material with improved properties than either material alone [7]. Composite materials have been extensively used in other industries due to their high strength, low weight, and excellent fatigue resistance [8]. The unique properties of polymeric matrix composite materials make them ideal for pipeline repairs, as seen in Figure 1, offering a faster, less expensive, and less disruptive alternative to traditional repair methods [2].

During operation, pipelines repaired with composites can be subjected to harsh conditions, especially in a marine/offshore environment. Thus, salt spray accelerated ageing tests can be used to simulate the effects that such conditions cause in materials and components. This method involves exposing the test samples to a salt spray fog, which accelerates the corrosion process and simulates the long-term effects of exposure to harsh environmental conditions such as saltwater, and high humidity in a short time period [9]. For pipeline repairs, salt spray tests can be especially useful because they can affect both the steel substrate and the composite repair at the same time, causing metal corrosion and moisture absorption in the composite and at the interface between the pipe and the repair, if the repair is not adequately applied.



Figure 1: Technician applying a composite repair to a pipeline in an offshore vessel. The composite material is wrapped around the defective section of pipe, after the surface has been cleaned and prepared. The technician applies layers of the repair material until the desired thickness is reached. Source: [10]

The degradation suffered by the repairs during operation needs to be identified and, if possible, monitored over time. Non-destructive testing (NDT) techniques are essential for pipeline repair integrity management, as they allow assessing the condition of the pipelines without causing any damage to the pipeline itself and without interrupting operation. NDTs can detect defects both at the surface and along the thickness of the material, including cracks, corrosion (Figure 2), and material degradation, which can compromise the integrity of pipelines [11,12].



Figure 2: Corrosion beneath the repaired area after removal of the composite wrap. The green area is where the composite repair was applied and the red arrows show the corrosion propagation that lead to the repair being reprovved upon NDT inspection. Source: BAWSF, used with permission.

The use of NDTs in pipeline repairs can also ensure that pipelines are repaired correctly and indicate the level of degradation that could occur during operation, reducing the risk of future failures and increasing pipeline safety and reliability. Two NDT techniques that show potential for pipeline repair inspections are ultrasound (UT) and shearography (SH). Ultrasound and shearography are non-intrusive methods that can detect and locate flaws in composite materials and can be well suited to applications in composite repairs in the field. Shearography has been successfully used for this purpose [13–15], while ultrasound has shown great potential for composite inspection [16–18], but applications in composite repairs over steel pipes are not yet common practice.

Ultrasound (Figure 3) is a widely used NDT technique that uses high-frequency sound waves to detect internal and external defects in pipelines. Ultrasound can detect defects such as cracks, corrosion, and wall thickness variations, as well as being able to determine the size and depth of defects. The technique works by emitting ultrasonic waves from a transducer, which travel through the material and are reflected by the

opposite surface or by a flaw. The reflected waves are then detected by the same or another transducer, and the data is processed to determine the location and severity of the flaw [19].

Shearography is an NDT technique that measures surface strains induced by mechanical or thermal loading to detect defects in repairs applied to pipelines. Shearography uses a laser and an interferometer to measure the surface strain of a material, and it is capable of detecting surface and subsurface defects. The technique works by directing a laser beam onto the surface of the material and recording the deformation of the surface caused by the loading. By comparing the strain patterns of a defect-free area with an area with a defect, the location and size of the defect can be determined [20].



Figure 3: Ultrasound inspection in a composite part, using a field deployable equipment. The technique has been used with composite materials with success, showing potential to work as a tool to monitor composite repairs as well. Source: [21]

With proper NDT monitoring, repair life could be extended with a strong basis for safe operation, both from the mechanical properties and defect propagation standpoints. Consequently, operation and repair costs can be lowered with fewer pipeline replacements or repairs.

Creating a model based on property retention of composite pipeline repairs is crucial to integrity management and can help engineers in the design phase. Models based on the Arrhenius equation have been proposed over the years to predict the long-term performance of composite materials [22–25]. These models can be used or modified to provide a better understanding of the long-term performance and durability of composite repairs, enabling engineers to design and select appropriate materials and repair techniques. Although composite repairs represent a viable solution for pipeline repairs, the long-term performance of composite materials can be affected by many factors such as ageing, and environmental conditions. Therefore, it is essential to evaluate the property retention of composite repairs over time to ensure their effectiveness and reliability.

A model can also be used to revalidate in-service repairs. Pipeline operators can periodically assess the condition of composite repairs using NDT techniques, and the data obtained can be used to update the model. By updating the model, pipeline operators can evaluate the effectiveness of the repairs and determine if any further repairs or maintenance are required.

In addition to helping with integrity management, the model can also assist engineers in the design phase by providing a better understanding of the long-term performance of composite repairs. The model can help engineers to design composite repairs that will meet the required performance standards and maintain their properties throughout the service life of the pipeline, already considering the degradation over the expected period.

This study is part of a much larger technical cooperation between PUC-Rio and Petrobras, where several aspects of composite repairs in steel pipelines are evaluated. The project includes samples of the repair material and composite-steel double-lap shear joints being subjected to destructive, thermo-mechanical, gravimetric and non-destructive testing, as well as analysis of materials from different repair manufacturers, in a broad research and development approach. This work focuses on the field deployable aspect of the technical cooperation, analyzing repaired pipe samples with test methods that are being and/or could be developed to be used in the field.

## 1.1. Objectives

The objectives of this work are:

- I) Perform accelerated ageing tests by salt-spray on steel pipes with composite repairs under three different temperatures;
- II) Evaluate the effectiveness of ultrasound and shearography inspections in detecting changes in the component's behavior over time;
- III) Compare the results of the two inspection techniques and assess their viability as field tools to monitor pipeline integrity;
- IV) Understand and correlate the mechanisms of degradation and damage propagation in the repairs;
- V) Propose a modified Arrhenius methodology to predict long-term damage propagation based on the results of the study.

## 2. Literature Review

### 2.1. Composite Materials

Callister [7] defines composite materials as “multiphase materials that exhibit a significant proportion of the properties of both constituent phases such that a better combination of properties is realized”. Composite materials can be further differentiated from other multiphase materials by the fact that, in the present context, the combination of properties must not be naturally occurring, such as in the case of some ceramic materials and metallic alloys, for example.

Composite materials are usually constituted of two distinct phases, with an interface between them. These phases are often called matrix phase and dispersed or reinforcement phase. Both play very distinct roles in the final properties of the material: the matrix is a continuous phase that gives the material its structure, surrounding and, to an extent, protecting and holding the dispersed phase in place. The dispersed phase or reinforcement will affect the properties of the final material as a function of its geometry, quantity – more often referred to as volumetric or volume fraction, orientation, distribution and so forth [7]. Typical configurations of the dispersed phase can be seen in Figure 4. The interface between the two phases is also a very important aspect of composite materials because it determines how much load can be transferred among phases.

A wide range of materials can be used for both phases of the composite material. For the matrix, polymers, ceramics and metals can be used. Polymers are by far the more common mainly due to its ease of processability and low cost [26]. In a polymer matrix composite, the matrix phase tends to play a minor role in the load bearing capacity of the material but is essential to provide protection from the environment and to keep the reinforcements in place. In thermoplastic matrix composites, the polymer provides increased ductility to the overall composite, which is important to prevent brittle failures, as reinforcements are usually fragile.

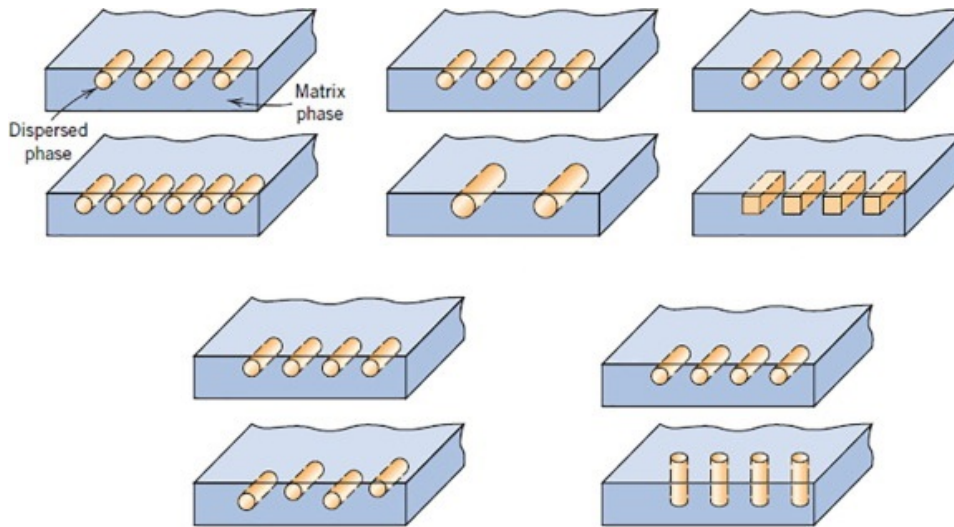


Figure 4: Classic representation of a composite material. Dispersed and matrix phases are represented in different configurations of orientation, distribution and shapes. The dispersed phase arrangement is very important for the final properties of the composite and it is a very important aspect to be considered in the design and/or material selection stages. Adapted from Callister [7].

Reinforcements can be found mainly in the form of particles or fibers. Particles and fibers differ mainly in their geometry, with particles having roughly the same dimensions in every direction and fibers having a more elongated form factor – usually with a cylindrical shape where the length is longer than the diameter of the fiber. For polymer matrix composites, particles are more often used as fillers to enhance the composite’s stiffness using reinforcements with higher moduli than of the matrix itself. Fiber reinforcements are far more used in higher demanding applications because of the intrinsic characteristics of most high-performance fibers, such as high modulus and/or strength allied with low density and design customization. The combination of polymeric matrices and high-performance fibrous reinforcements creates very desirable properties in what is termed “advanced composites” [8]. Figure 5 shows a

comparison between the specific properties of composites against other families of materials.

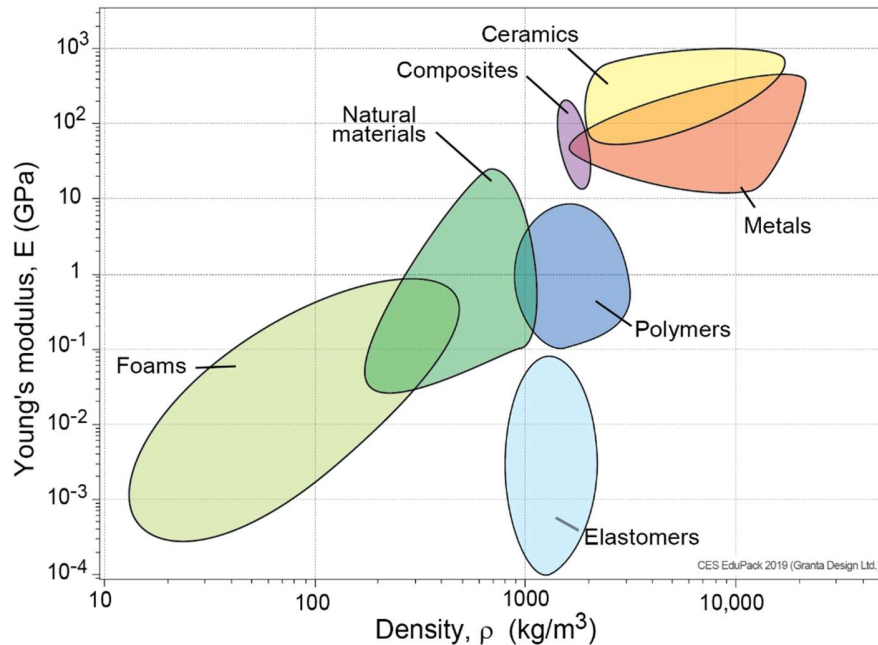


Figure 5: Ashby plot of different families of materials. Composites show comparatively high moduli while having density in the same magnitude as polymers or elastomers. Source: Granta Design (<https://www.grantadesign.com/education/students/charts/>)

Although usually more expensive than other structural materials, the performance, flexibility of design and lightness of composites often justify their use in high performance applications. Much can be customized in the way of fiber orientation, distribution, and bias, stacking of layers, selection of polymeric matrix and more. Furthermore, different fabrication methods can yield different properties and can be more or less suitable to a specific design requirement or project constraint. Industries that include aerospace, transportation, oil & gas, renewables, sports (Figure 6) and industry 4.0 make great use of the unique properties of these materials [27–32], creating an ever-increasing demand for new developments in material characterization, manufacturing and modelling.



Figure 6: Ferrari SF-23 Formula 1 car. In a modern F1 car, composites are widely used because of its lightweight and high performance. Most of the bodywork, aero, suspension and even parts of the engine are made out of carbon fiber reinforced composites. Furthermore, brake discs use high temperature carbon reinforced ceramic matrix composites that can withstand continuous 1000 °C+ temperatures. Source: Ferrari.com

## 2.2. Composite pipeline repair systems

Composite pipeline repairs refer to the use of composite materials to repair damaged or corroded sections of pipelines. These repairs involve wrapping the damaged area of the pipe with a composite material that has high strength, high modulus and durability, providing a cost-effective and reliable solution to extend the life of the pipeline.

The use of composite materials for pipeline repairs has been extensively studied and documented in scientific literature. Researchers have investigated the mechanical properties, such as tensile strength, compressive strength, and flexural strength, of various composite materials for pipeline repairs [5, 6, 33]. They have also evaluated the performance of composite repairs under different conditions, including internal pressure, bending, cyclic fatigue and high temperatures [33–37]. Other than composite materials, common repair techniques include substitution of the damaged segment, clamps, welded sleeves and cladding [38]. The selected method of repair will be

determined as a function of the risk a defect poses to the pipeline [20]. A chart of the decision-making process is shown in Figure 7.

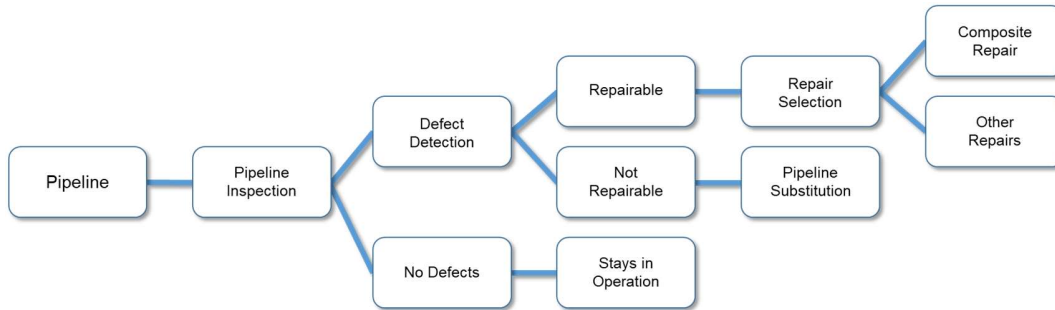


Figure 7: Flowchart of the decision making process involved in repairing a pipeline. After initial inspection, in the case of damage detection, a sequence of decisions must be made.

Adapted from [20].

Studies have shown that composite repairs can significantly enhance the structural integrity of pipelines, especially in areas where traditional repair methods are difficult or impossible to use [5, 29]. However, the effectiveness of composite repairs depends on several factors, including the design of the repair system, the quality of the materials used, and the application process. Therefore, it is crucial to follow industry standards and guidelines for composite pipeline repairs to ensure their long-term reliability, such as the ISO/TS 24817 [39] and ASME PCC-2 [40].

The process of applying composite repairs to steel pipes usually present the following steps [20]:

- I) Surface preparation of the steel pipe;
- II) Application of compatibilizing agent, such as silane (optional);
- III) Application of a discrete adhesive layer, usually with similar composition to the laminate matrix (optional);
- IV) Application of the wrap until desired thickness is reached;
- V) Application of a protective layer against severe weathering and UV radiation (optional).

Some of the advantages of composite repairs include ease of application, do not require welding, can be applied over any extension of damage and over bends, do not require stoppage of operation and its installation costs are relatively low [20].

### **2.2.1. Fiber Reinforced Polymer (FRP) repairs degradation mechanisms**

Fiber reinforced repair systems have gained popularity in the repair and rehabilitation of pipelines due to their high strength, corrosion resistance, and durability. However, FRP pipeline repair systems are also subject to environmental and/or operational conditions that can affect their long-term performance. The mechanisms by which degradation affects the life in service of the repair vary as a function of what conditions are analyzed. For example, the degradation mechanisms that occur due to environmental exposure are not the same as mechanical loads being applied to the material, although both can occur at the same time [41, 42].

In marine and offshore applications, FRP repairs can be exposed to harsh environmental conditions such as saline atmospheres, elevated humidity, temperature variations, UV radiation, and chemical exposure. Sustained exposure to these conditions can cause damage to the FRP composite material, mainly to the interface between repair and pipeline, leading to delamination, cracking, and loss of strength, which has been widely reported in literature [43–50]. Furthermore, FRP repair systems can suffer from operational loads such as high internal pressures and conditions like corrosive fluids. In addition, fatigue degradation can also occur, caused by repeated loading and unloading cycles, which, although not covered by this work, has been also extensively reported in literature [51–53].

One of the main degradation mechanisms is caused by external corrosion in the steel pipe along the edges of the repaired area. According to Perrut [2], the transition area between FRP repair and steel pipeline is critical, even in areas where the composite repair has been painted over (polymeric coating). The critical nature of this area is mainly due to a stiffness difference between the two materials causing out-of-plane stresses and differential thermal expansion, thus making this region prone to defects on the medium to long terms. Damage in this area can lead to moisture infiltration along

the edges of the repair, which weakens the interface between repair and metallic substrate. This weakened interface can suffer from loss of adhesion, making way for corrosion to spread underneath the repaired area. It can also cause moisture uptake in the interface itself, which could lead to effects like plasticization, hydrolysis and crazing.

Perrut [2] in his work performed a series of tests on double-lap shear specimens to simulate the effects of hygrothermal ageing in FRP repaired pipelines, using salt-spray fog and water immersion. The author found that both static and dynamic mechanical properties of the system were significantly affected by the ageing process. The work also showed that most of the performance lost by the joints was caused by changes in the interface between repair and steel substrate area and an adequate surface preparation of the substrate is very important to longevity. These changes caused loss of adhesion, changes in adhesive failure mode, delamination and further corrosion of the steel.

Environmental conditions may also affect the composite material itself as consequence of hygrothermal exposure. Temperature and humidity can degrade the performance of the repair, mainly due to the plasticization of the matrix phase of the composite and long-term fiber/matrix interface degradation. Some of the possible effects of hygrothermal exposure are showed in Figure 8 [54]. Tual et al. [55] tested three types of carbon-reinforced composites, without any substrate, and evaluated the effects of hygrothermal ageing. The authors found that in-plane strengths were far more affected than moduli, with plasticization, and subsequent deterioration of fiber/matrix interface being the main culprits. They also observed that, upon drying, most of the effects of initial plasticization and swelling due to moisture uptake were reversible, whereas the effects on the fiber/matrix interface were not.

A recent study by Guo et al. [56] confirmed the observations of Tual et al., using pultruded glass, carbon and glass/carbon hybrid reinforced epoxy samples under three different temperatures over 135 days. According to the authors, the effects of plasticization caused by water ingress were reversible upon drying, but the long-term effects of resin relaxation due to hygrothermal exposure may lead to irreversible damage, such as interface debonding of fiber or resin and fiber damage. The authors

further expand on the effects on the glass transition temperatures of the matrices, which decreased significantly over exposure time, but were also reversible. Other authors found similar results [50, 52, 53, 57–68].

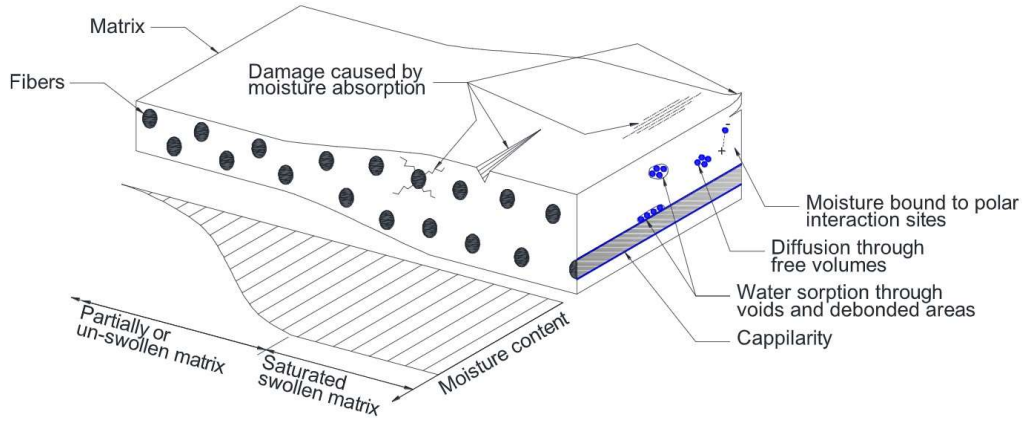


Figure 8: Effects of moisture uptake in a fiber-reinforced composite material, such as a FRP repair - Adapted from Vieira et al [54].

In both Tual et al. [55] and Guo et al. [56] studies, damage is caused by moisture diffusion through the polymer/resin, either in the adhesive/interface area of repair and steel substrate or the matrix phase of the composite. This phenomenon is generally described by Fick's first law (Eq. 1). In this equation,  $J$  is the flux of diffusion,  $D$  is the coefficient of diffusion and  $\left(\frac{\partial C}{\partial x}\right)$  is the concentration gradient.

$$J = -D \left(\frac{\partial C}{\partial x}\right) \quad (\text{Eq. 1})$$

The coefficient  $D$  is described by Eq. 2, where  $D_0$  is the pre-exponential factor,  $E_a$  is the activation energy,  $R$  is the universal gas constant and  $T$  is the temperature in kelvin.

$$D = D_0 e^{\left(\frac{-E_a}{RT}\right)} \quad (\text{Eq. 2})$$

As seen in Eq. 2, the coefficient of diffusion is directly dependent of temperature, following an Arrhenius-like relationship. Thus, if diffusion is the main factor causing degradation in FRP repairs, material behavior could be predicted over time with increased temperatures using Arrhenius-like plots. Bank et al. [69] used a model where the degradation rate was expressed by an Arrhenius relationship, as seen in Eq. (3). In this equation,  $k$  is the degradation rate with unit as 1/time and  $A$  is a constant of the material and degradation process.

$$k = A \exp\left(\frac{-E_a}{RT}\right) \quad \text{Eq. 3}$$

As seen in Wu et al. [22], Eq. 3 can be rearranged to fit a commonly used degradation model format (Eq. 4). The resulting equation is Eq. 5, where the logarithm of the amount of time for a property to reach a certain threshold is a linear function of the inverse of temperature with an angular coefficient of  $(E_a/R)$ . Many authors [22, 54, 67, 69–77] have used these relations with varying degrees of success to predict properties or to establish acceleration factors for ageing tests.

$$Y = a \log(t) + b \quad \text{Eq. 4}$$

$$\ln\left(\frac{1}{k}\right) = \frac{E_a}{R} \frac{1}{T} - \ln(A) \quad \text{Eq. 5}$$

Although useful for many applications, this approach fails in some aspects when long-term behavior is investigated. According to Davalos et al. [23], models based solely on Arrhenius-like relations assumes that the degradation mechanism will not change over time and that temperature exposure would only accelerate the process, which does not always agree with the experimental data.

Research shows that, for longer periods of hygrothermal exposure, the degradation mechanism does indeed change to a non-Fickian response, thus a simple Arrhenius-like model is not enough to provide a reliable prediction. Guo et al. [56] modelled the water absorption behavior of FRPs as a two-stage diffusion response,

which is initially described by Fick's law (first stage) and a non-Fickian second stage, in which the water absorption rate decreased due to changes in the degradation mechanism. This second stage is governed by resin relaxation and interface debonding of fiber and resin, which affects long-term deterioration and causes permanent damage to the material.

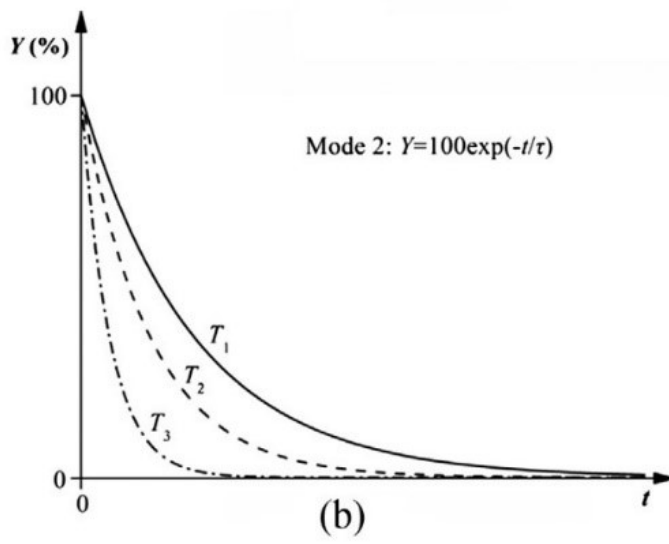
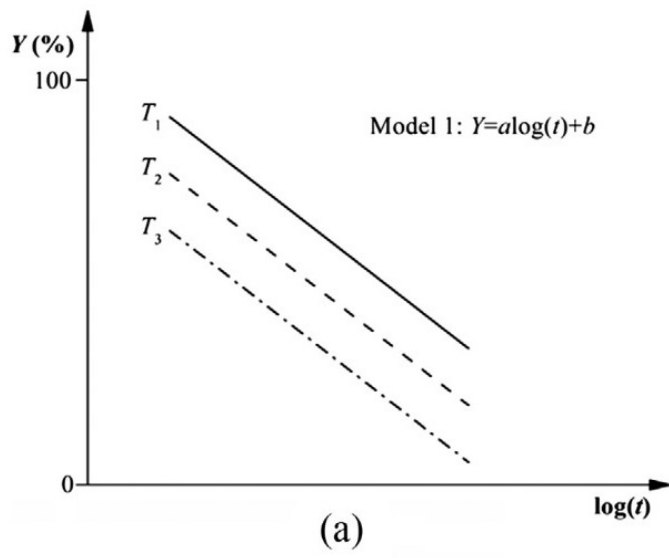
Wang et al. [78] compared three different models to evaluate their effectiveness in predicting long-term material behavior (Figure 9). The first one was a simple Arrhenius-like model (Figure 9a), in which the authors confirmed shortcomings previously mentioned by Wu et al. [22]. The remaining two (Figure 9b and 9c) were based on the work of Phani and Bose [24, 25], and proved to correlate much better with experimental data.

The Phani and Bose model represents a superposition of the effects of temperature and time on the degradation of the material and is described by Eq. 6:

$$Y = (Y_0 - Y_\infty) \exp\left(\frac{-t}{\tau}\right) + Y_\infty \quad \text{Eq. 6}$$

Where  $Y$  is the property retention,  $Y_\infty$  is the property retention at infinity,  $Y_0$  is the initial value of the property, before ageing,  $t$  is exposure time and  $\tau$  is the fitted time parameter. The parameter  $\tau$  represents the amount of time necessary for the property investigated to reach a certain value, and may be directly correlated to the temperature through an Arrhenius relationship (Eq. 7).

$$\frac{1}{\tau} = \frac{1}{\tau_0} \exp\left(\frac{-E_a}{RT}\right) \quad \text{Eq. 7}$$



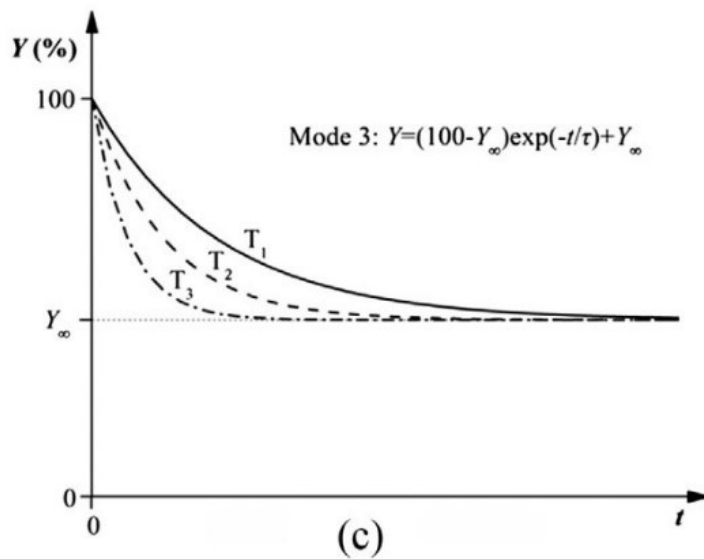


Figure 9: Comparison between three proposed methods by Wang et al. a) Arrhenius-based model; b) Phani-Bose model with property retention reaching zero; Phani-Bose model with property retention reaching a stable threshold at infinity. Source: Wang et al. [78].

The experimental property retention % as a function of ageing time is fitted to a curve using regression and then plotted in an Arrhenius plot. The Arrhenius plot gives the logarithm of the time necessary to reach a certain value of property retain as a function of  $1000/T$  in kelvin. Hence it is possible to predict the amount of time necessary to reach a certain threshold of property retention given a certain temperature or vice-versa. This model has been used with good correlation with experimental data as reported in the literature [22–25, 56, 76–79].

### 2.3. Salt Spray Accelerated Ageing

Salt spray accelerated ageing tests, as defined by the ASTM B117 standard [9], are commonly used to evaluate the corrosion resistance of metallic materials. The test involves exposing the sample to a salt spray fog in a controlled environment for a specified period, and then assessing the degree of corrosion that has occurred. The standard also provides guidelines for evaluating the degree of corrosion that has occurred on the sample surface after exposure to the salt spray mist. This can be done

using a variety of techniques, including visual inspection, mass loss measurement, and electrochemical testing.

The salt spray mist used in the test is typically a solution of sodium chloride in water, with a concentration of 5% by weight. The samples are placed in a chamber (Figure 10) that is heated to a set temperature (ASTM B-117 specifies 35°C) and maintained at a relative humidity of 95%. The salt spray mist is then continuously sprayed into the interior of the chamber for a specified number of hours, usually ranging from 24 to 1000 hours and beyond [9].

Although this test is more often used to evaluate the corrosion resistance of metallic materials, it can also be used to evaluate the long-term behavior of non-metallic materials such as fiber-reinforced polymers (FRPs), which are increasingly used in various applications due to their high strength-to-weight ratio, corrosion resistance, and durability. A myriad of industries, such as aerospace [80], civil engineering [79, 81–84], automotive [85] and Oil & Gas [34, 36, 86], for example, often use accelerated ageing tests to investigate the changes in properties of composite materials in a compressed timeline. Tests such as this can simulate conditions closely related to what the material would find in, for example, a marine environment. Figure 11 shows an example of the evolution of the degradation suffered by a FRP repair subjected to salt-spray ageing, in conditions similar to what would be found in offshore applications.



Figure 10: Typical salt-spray test equipment. Source: Equilam

The effects of salt spray on mechanical properties are related to several factors, including the type and composition of the composite materials, the duration of the test, and the environmental conditions during the test. For instance, a study by Chakraverty et al. [87] found that the mechanical properties of fiber-reinforced polymer composites were more affected negatively by salt spray exposure and that the rate of moisture absorption changed from Fickian to non-Fickian with increased exposure time. Furthermore, a study by Sousa et al. [88] found that test temperature was a major factor on the properties of adhesively bonded joints, with higher temperatures leading to a more pronounced degradation.



Figure 11: Steel/composite double-lap shear samples after being through salt-spray testing.

Source: [2]

However, it is important to note that the results of salt spray accelerated ageing tests should be interpreted with caution. Test conditions may not accurately simulate the actual environmental conditions that the material will be exposed to and material variables such as curing or post-curing could play an important role when trying to predict long-term behavior [89]. As such, it is recommended that these tests be used as a screening tool to identify materials likely to perform well in corrosive environments, rather than as a definitive measure of corrosion resistance. Furthermore, the effects of temperature must only be of accelerating the test and must not cause any thermal degradation to the material itself.

## 2.4. Shearography

Shearography is a non-destructive, optical test method that can measure displacement field gradients on the surface of materials [90] using principles of speckle interferometry [20,91]. During a shearography inspection, the specimen is stressed to create very small deformations while being lit up by a LASER source, in order to generate a speckle pattern. Images are captured using a special optical device that produces laterally dislocated pairs of images, as if a shear force has been applied – hence the name shearography – from which a phase map of the displacement derivatives of the stressed specimen is generated [92].

Some of the advantages of this technique include simple setups and lower sensibility to vibrations especially when compared to other optical techniques, the possibility of direct measurement of the deformation gradient on the surface of the sample, lack of coupling media and possibility of measuring large areas at once [20].

In Figure 12, a typical shearography setup is shown. The setup consists of a LASER source, used to illuminate the sample and generate the speckle pattern, a modified Michelson interferometer with adjustable mirrors to produce laterally dislocated pairs of images, a digital camera to acquire the data and a computer with dedicated software to process and analyze the images. In addition, some form of stress

producing device must be used to cause the necessary deformations in the test object [13].

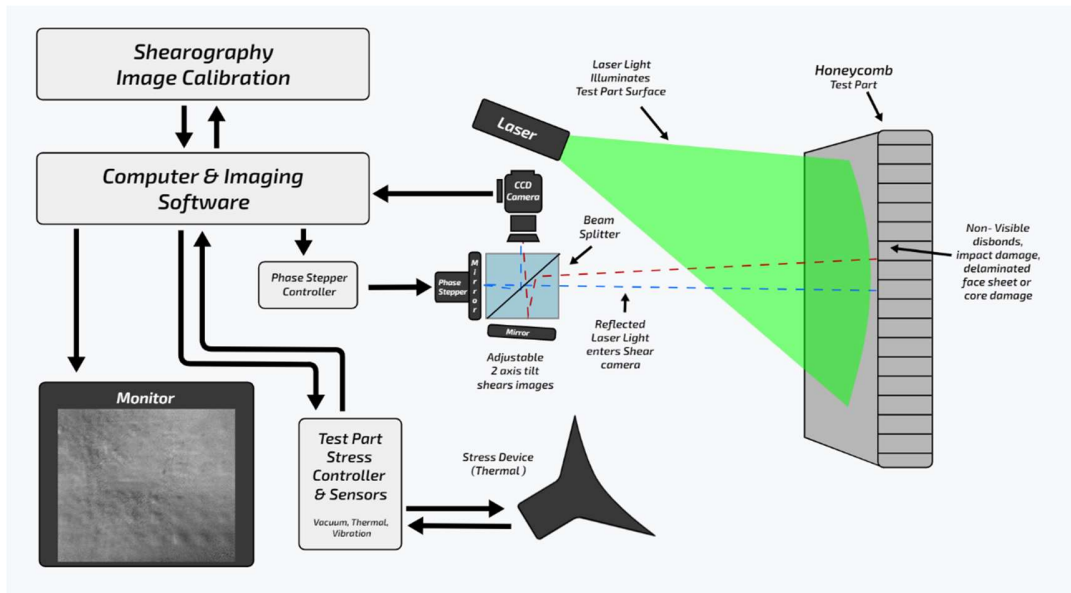


Figure 12: Shearography setup, adapted from [93]. The main components of the setup are the laser source, the modified interferometer, the camera, the computer with dedicated software and a device to stress the sample.

Most defects found in composite materials structures are caused by discontinuities within the material or with the substrate it is adhered to (Figure 13). These can be traced to problems during lamination or throughout the lifetime of the material and manifest themselves as voids, porosity, delaminations and loss of adhesion. These unadhered areas will deform differently from its surroundings once stress is applied, causing discontinuities in the deformation fields, which in turn, will cause anomalies in the interference patterns observed by the operator [20].

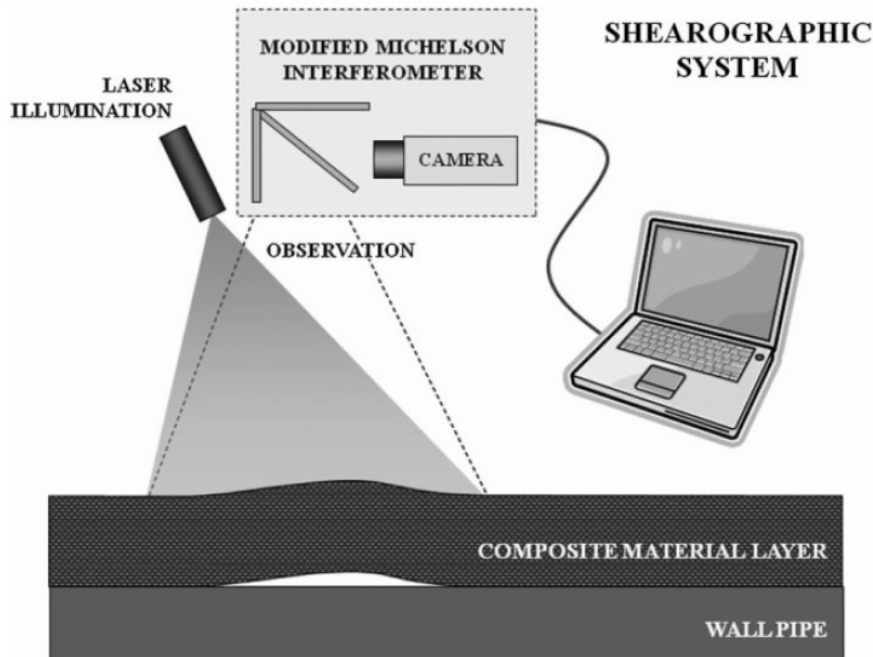
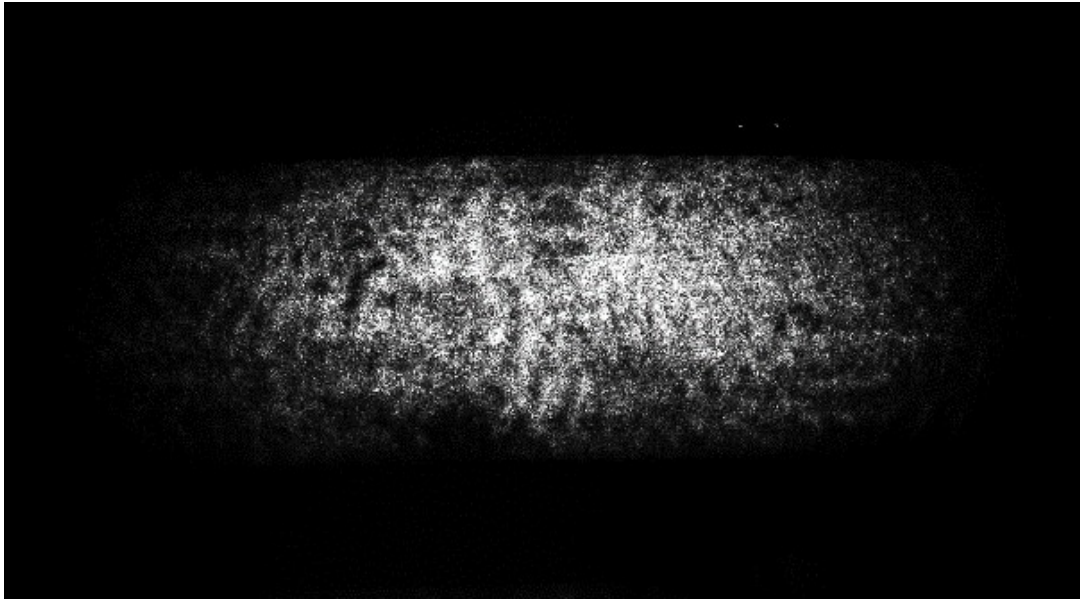
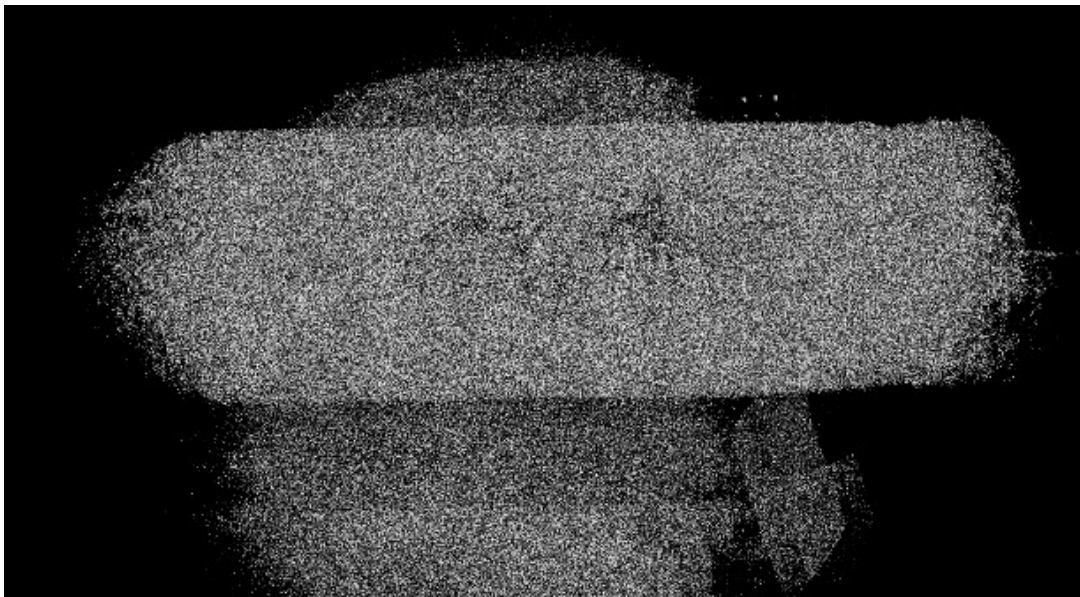


Figure 13: Example of an area of unadhered composite and metallic substrate, a typical use case for shearography inspections [13].

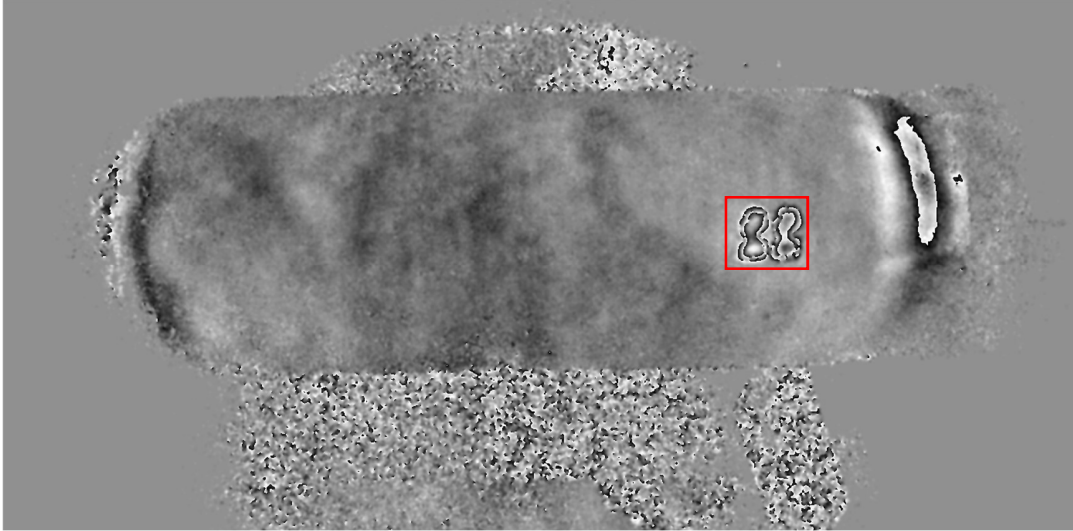
Usually, during a shearography inspection, the first step is to illuminate the test object with a LASER source to generate a speckle pattern. Then, a pair of laterally dislocated images is generated using the modified interferometer to control the amount of dislocation applied. Before loading, a phase map (usually 4 or 8 pairs of images per map) of the material before any stress has been applied is obtained as reference. Upon loading, new pairs of images are acquired to generate phase maps of the stressed state of the object. The data is then analyzed via a dedicated software, where an algorithm will generate interferograms that display the differences in the phase maps acquired. Defects will show up as interference fringe patterns on the interferograms, which represent the first derivative of the out-of-plane displacements, perpendicular to the plane that is being measured [20]. The interferograms appear to the operator as an animation, instead of static images, which makes the identification of the fringe patterns easier. An example of each stage of the image processing on an inspection of a steel pipe with composite repair is shown in Figure 14.



a)



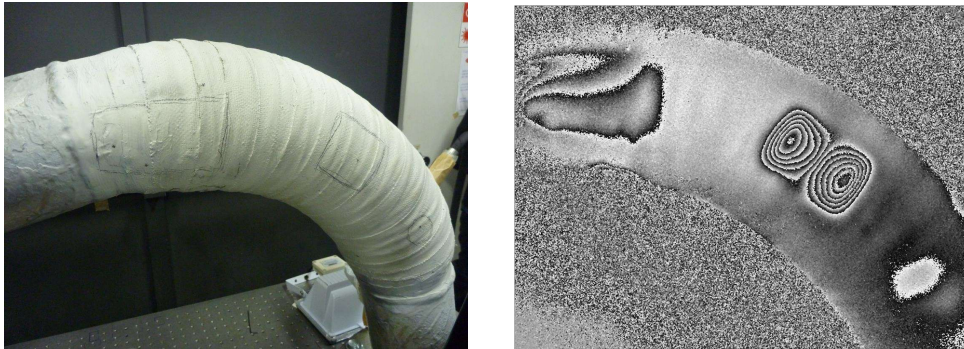
b)



c)

Figure 14: a) Pair of laterally dislocated images; b) phase map constructed using 4 pairs of laterally dislocated images; c) interferogram showing in red fringe interference patterns that indicate a rectangular shaped defect. Source: BAWSF, used with permission.

During the inspection, the object is stressed either via thermal, mechanical or vibrational excitation [20]. Most common forms of excitation are thermal and pressure application and only light loads or temperature variation are enough to acquire data – about 4°C or 1 bar. Over-excitation of the test object and excessive vibration during testing can cause problems, since large object movements can make image correlation difficult [13]. Figure 15 shows examples of defects found using shearography inspection in the field.



a)

b)

Figure 15: Example of a pipe bend: a) image of the repaired pipe bend; b) shearography image showing three kinds of fringe patterns indicating defects. Source: BAWSF Archive – Used with permission.

This technique has been shown to detect some of the most common defects found in composite materials, with applications in a great variety of industries [13, 91, 94–98]. Some examples are tire manufacturers [99], aerospace [18,100,101] (Figure 16) and, more recently, Oil & Gas in such applications like bonded composite pipelines joints [15], composite repairs on metallic pipes [13, 14, 20, 102, 103], pressure vessels [102] and ship hulls [104].



Figure 16: Shearography fringe patterns overlaid on a test subject. The technique detected flaws in a composite elevator flap, from an Airbus A330 aircraft, previously inspected by thermography. Drawn markings indicate thermography detections. Source: Author's own archive.

Soares et al. [11] evaluated the feasibility of using shearography to inspect steel pipelines repaired with composite materials in the field. Tests were performed both at laboratory conditions with samples containing artificial flaws and in field conditions. Laboratory tests showed positive results, which were later confirmed in the field, both on and offshore. Although vibrations and difficulties to reach some of the repaired areas due to space constraints caused some challenges, the technique showed good results and was recommended to deployment in the field. Růžek et al. [105] compared the performance of shearography and ultrasound to assess impact damage in composite structures. The authors found that shearography was more suited to the application, due to limitations of the UT technique to detect impacted areas where the composite material was deformed but not completely broken.

## 2.5. Ultrasound

Ultrasound (UT) inspection is a non-destructive test method which uses mechanical waves to penetrate the material and provide information about its internal structure. In an ultrasonic inspection, high frequency sound waves are emitted through a transducer at the surface of the material and acoustic impedance differences across the thickness of the inspected sample will generate reflections, often called echoes, which can be detected. The reflected waves can be analyzed to detect any defects or anomalies in the material, such as delaminations, voids, cracks, or general lack of homogeneity. UT has been widely used throughout the aerospace [18], renewable energies [106], and Oil & Gas industries [12, 107] and industry 4.0 initiatives [108].

One of the most common methods for UT inspections is the pulse-echo technique [17]. In a typical pulse-echo UT setup, the inspection is carried out on only one of the surfaces (contrary to the transmission technique) and the main components are the emitter/receiver, the transducer and a monitor for viewing the signals (Figure 17). The emitter/receiver is an electronic device that can produce high voltage electrical pulses and works together with the transducer. The transducer often uses the piezoelectric principle to convert the electrical pulses into mechanical waves and vice-versa. If there are any anomalies along the path of the wave, a reflection will occur,

which will be detected and converted to an electric signal by the transducer and displayed in a monitor. The information on the monitor is used by the operator to analyze the different reflections detected by the transducer, whether caused by defects in the material (defect echo) or natural reflections caused, for example, by the opposite surface of the material (back surface echo). The time it takes for a wave to travel through the material and be reflected back to the transducer is called time-of-flight and provides important information about the defect detected, such as location, size and orientation, for example [19].

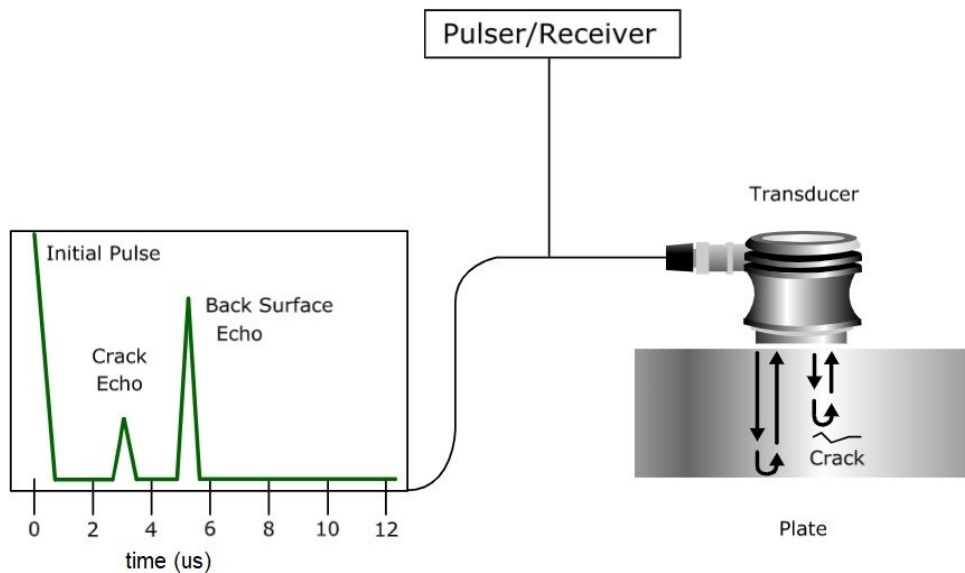


Figure 17: The reflected signal strength is displayed versus the time from signal generation to when an echo was received. Adapted from [19]

The information gathered during the UT inspection comprises a wide variety of signals from different reflections from within the inspected part. Signal processing is an important part of the UT workflow and includes gating procedures (Figure 18), in which a specific reflection (or echo) is separated for further signal processing [109]. Then, automated detection criteria can be applied using algorithms in dedicated software, such as MatLab [110].

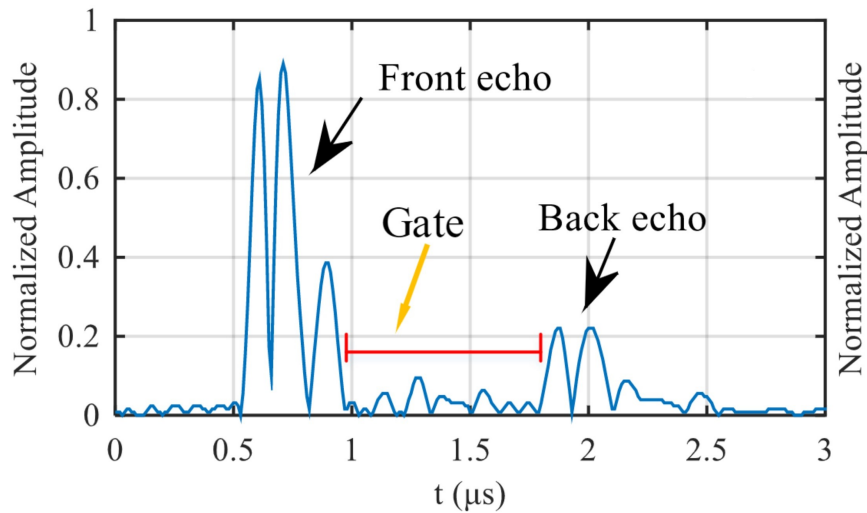


Figure 18: A-Scan signal with a gate set at the red marked region. The gate is set, in this case, between the front and back echoes, which represent the upper and bottom surfaces of the sample, respectively, in order to detect internal damages in the material. Adapted from [111].

Some of the advantages of UT inspection include highly accurate defect positioning and measuring it can be performed even if only one side of the inspected object is accessible, requires minimal surface preparation, it is easy to automate and there is the possibility of characterizing properties in addition to defect detection [19]. The limitations of UT include the necessity of a coupling medium between the transducer and the surface of the inspected part. The ultrasonic waves need a medium in which to propagate, which is usually water or gels, since air causes severe attenuation, although in some cases it is possible to perform contactless inspections [112, 113]. Also, linear defects parallel to the sound beam can be difficult to detect and irregular shaped surfaces can cause problems to the inspection [19].

More recently, UT techniques have been developed to be able to inspect composite materials such as laminates, pultruded structures, composite pipes, joints and repairs [16, 17, 112–120]. Tamborrino et al. [116] were able to successfully detect defects in adhesive bonded composite single-lap joints using the pulse-echo method. The authors compared the results of UT inspection with thermography analysis and found similar results between the two techniques. Tsao and Hocheng [120] used UT and computerized tomography to evaluate delaminations caused by drilling in carbon

fiber/epoxy composites. The authors found that both techniques were successful in their detections and that both performed similarly.

One of the main challenges for the inspection of composites using UT is the anisotropic and heterogeneous nature of the material, which causes absorption of the ultrasonic waves by the polymeric matrix, resulting in energy loss due to scattering, skewing and absorption [121]. Many authors [122–124] have also used UT to evaluate the elastic properties of composite materials, such as Young's modulus and Poisson's ratio.

UT has also been successfully used to inspect composite joints as seen in the work of de Almeida et al. [125] and de Almeida and Pereira [121]. In the study of de Almeida et al. [125], the authors tested different single frequency transducers to detect artificial flaws in bonded composite joints, simulating lack of adhesion. The results showed that frequencies around 1.0 MHz gave the best results among the tested frequencies, with accuracy above 60% in all samples. In de Almeida and Pereira [121], the authors successfully employed the phased array technique to inspect glass fiber reinforced polymer (GFRP) laminated joints with thicknesses up to 30 mm, being able to detect all inserted artificial flaws and also other non-artificial flaws. The results were later confirmed by computerized tomography, showing the effectiveness of the technique for this kind of inspection.

### 3. Materials and Methods

Samples of steel pipeline with composite repairs were fabricated and analyzed using NDTs both in as fabricated and aged conditions. A simplified flowchart is shown in Figure 19. Repair application was done by one of the manufacturers with the most number of repairs currently in the field, following the specification of those repairs already in operation. Shearography was performed by BAWSF, a service provider already deployed by Petrobras to inspect repairs in the field, whereas ultrasound was performed by LNDC to test their methodology and evaluate the feasibility of use in the real-life scenarios. The ageing process was done in salt-spray chambers custom made for this project, in three different temperatures.

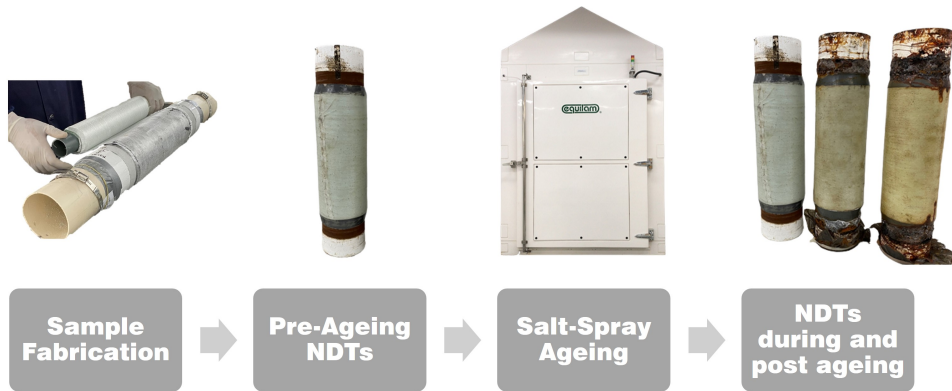


Figure 19: Simplified flowchart of the experimental program.

#### 3.1. Fabrication of test pipes

Steel pipes with the specifications shown in Table 1 were used to fabricate all pipeline repair samples. The steel pipes were received cut-to-length and were painted according to the Petrobras standard N-442 [126]. The paint procedure consisted of a surface preparation and two stages of paint. Surface preparation was performed according to the ST3 (ISO 8501-1) standard to remove any rust or contaminants. The painting steps were done in accordance to N-442 condition 1, using N-2680 certified paint as a base layer and N-2677 certified paint as a topcoat.

Table 1: Steel pipe and repair nominal dimensions.

| <b>Parameter</b>    | <b>Values</b> |
|---------------------|---------------|
| Steel Grade         | API 5L Gr. B  |
| Pipe Outer Diameter | 114.3 mm      |
| Pipe Wall Thickness | 6.02 mm       |
| Pipe Inner Diameter | 102.26 mm     |
| Pipe Length         | 500 mm        |
| Repair Length       | 300 mm        |
| Repair Thickness    | 6.0 mm        |

Once painted, the pipes were sent to the repair manufacturer. Both to-be-tested and reference repaired pipes were fabricated by the same manufacturer at its facility by their field repair technicians. The first steps of the process were paint removal and surface preparation according to the specified conditions. Paint was removed from the area where the repair was going to be applied, plus 20 mm on each side for tapering of the edges of the repair and plus 25 mm further on each side to force corrosion to occur on an unprotected area. The surface of each pipe was prepared according to four different types of treatments and their rugosity measured, the analysis of which is not part of the scope of this work.

The repair itself was applied using a hand layup process, with nominal dimensions listed in Table 1. A polymer matrix composite material was used, composed of a bidirectional fiberglass fabric with a 2:1 weave and a weight of 365g/m<sup>2</sup>, impregnated with the lamination resin through the manual lamination process. Table 2 shows the properties of the laminate after curing.

The glass fiber was wrapped around the pipe with epoxy resin being simultaneously applied until the final thickness was achieved. Figure 20 shows some of the steps during the lamination of one of the test samples used in this work.

Table 2: Composite laminate properties. Data obtained from the Type Approval process carried out by the American Bureau of Shipping (ABS) and provided by the manufacturer.

| Parameter                                     | Value  |
|---|--|
| Ply Thickness                                 | 0.3 mm   |
| Circumferential Young's Modulus               | 23.1 GPa   |
| Axial Young's Modulus                         | 12.4 GPa   |
| Poisson's Ratio ( $\nu_{12}$ )                | 0.16   |
| Shear Modulus ( $G_{12}$ )                    | 3.755 GPa  |
| Circumferential Thermal Expansion Coefficient | $11.6 \times 10^{-6} \text{ } ^\circ\text{C}^{-1}$ |
| Axial Thermal Expansion Coefficient           | $11.6 \times 10^{-6} \text{ } ^\circ\text{C}^{-1}$ |
| Energy Release Rate ( $\gamma_{LCL}$ )        | 146,44 J/m <sup>2</sup>                            |
| Glass Transition Temperature                  | 116 °C   |
| Curing Time                                   | 6 h  |

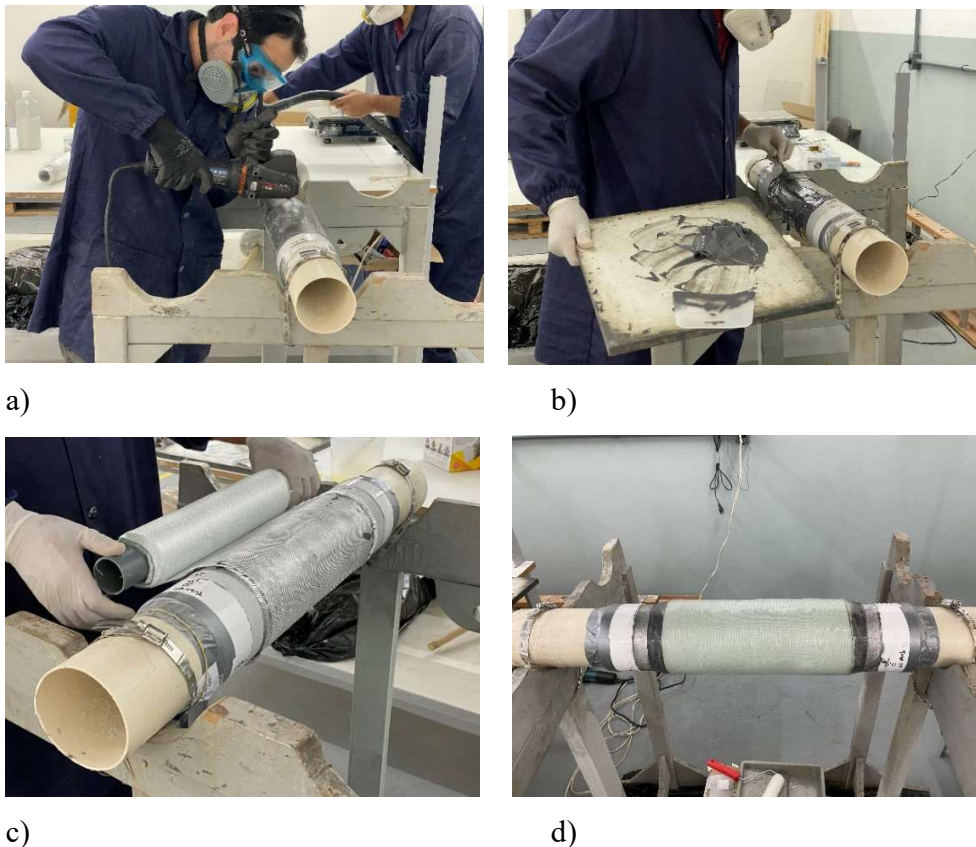


Figure 20: Some of the steps of applying a composite repair to a steel pipe: a) preparing the surface: removing paint and corrosion with a plastic pipe insert used as support; b) applying a discrete adhesive layer; c) applying the wrap; d) finished pipe with repair. Source: author's own archive.

In total, 25 samples were fabricated, of which, 24 were used during the accelerated ageing test. Additionally, markings indicating the 0 position and direction of inspection were made on all samples.

A reference pipe with artificial defects was also fabricated and the details can be found in the next section. The measurements of each sample are listed in Table 3.

Table 3: Measurements of the repaired pipe samples as fabricated. Measurements made by BAWSF before shearography inspection at T0. Listed are the samples which were aged, thus excluding pipe 0 (reference, not aged) and pipe 4, which was discarded.

| Sample | Steel Pipe Perimeter (mm) | Repaired Area Perimeter (mm) | Repair Thickness (mm) | Repair Length (w/o borders) (mm) | Repair Length (w/ borders) (mm) |
|--------|---------------------------|------------------------------|-----------------------|----------------------------------|---------------------------------|
| 1      | 362                       | 406                          | 7.0                   | 284                              | 344                             |
| 2      | 362                       | 404                          | 6.7                   | 288                              | 338                             |
| 3      | 362                       | 406                          | 7.0                   | 288                              | 344                             |
| 5      | 362                       | 404                          | 6.7                   | 294                              | 349                             |
| 6      | 362                       | 404                          | 6.7                   | 288                              | 346                             |
| 7      | 362                       | 404                          | 6.7                   | 286                              | 344                             |
| 8      | 362                       | 404                          | 6.7                   | 287                              | 346                             |
| 9      | 362                       | 404                          | 6.7                   | 290                              | 341                             |
| 10     | 362                       | 402                          | 6.4                   | 293                              | 343                             |
| 11     | 362                       | 403                          | 6.5                   | 290                              | 344                             |
| 12     | 362                       | 405                          | 6.8                   | 290                              | 340                             |
| 13     | 362                       | 404                          | 6.7                   | 282                              | 344                             |
| 14     | 362                       | 404                          | 6.7                   | 282                              | 342                             |
| 15     | 362                       | 402                          | 6.4                   | 288                              | 351                             |
| 16     | 362                       | 402                          | 6.4                   | 286                              | 346                             |
| 17     | 362                       | 404                          | 6.7                   | 290                              | 344                             |
| 18     | 362                       | 406                          | 7.0                   | 294                              | 350                             |
| 19     | 362                       | 402                          | 6.4                   | 290                              | 346                             |
| 20     | 362                       | 402                          | 6.4                   | 288                              | 346                             |
| 21     | 362                       | 402                          | 6.4                   | 290                              | 342                             |
| 22     | 362                       | 402                          | 6.4                   | 288                              | 340                             |
| 23     | 362                       | 404                          | 6.7                   | 290                              | 344                             |
| 24     | 362                       | 401                          | 6.2                   | 288                              | 344                             |
| 25     | 362                       | 403                          | 6.5                   | 288                              | 346                             |

### 3.1.1. Reference pipe fabrication

A reference pipe was fabricated to simulate defects in the interface between pipe and composite repair. The defects were made out of Teflon tape, folded to create

a pocket of air, similar to what would happen in case of localized lack of adhesion. The positioning and size of the artificial defects can be seen in Figure 21.

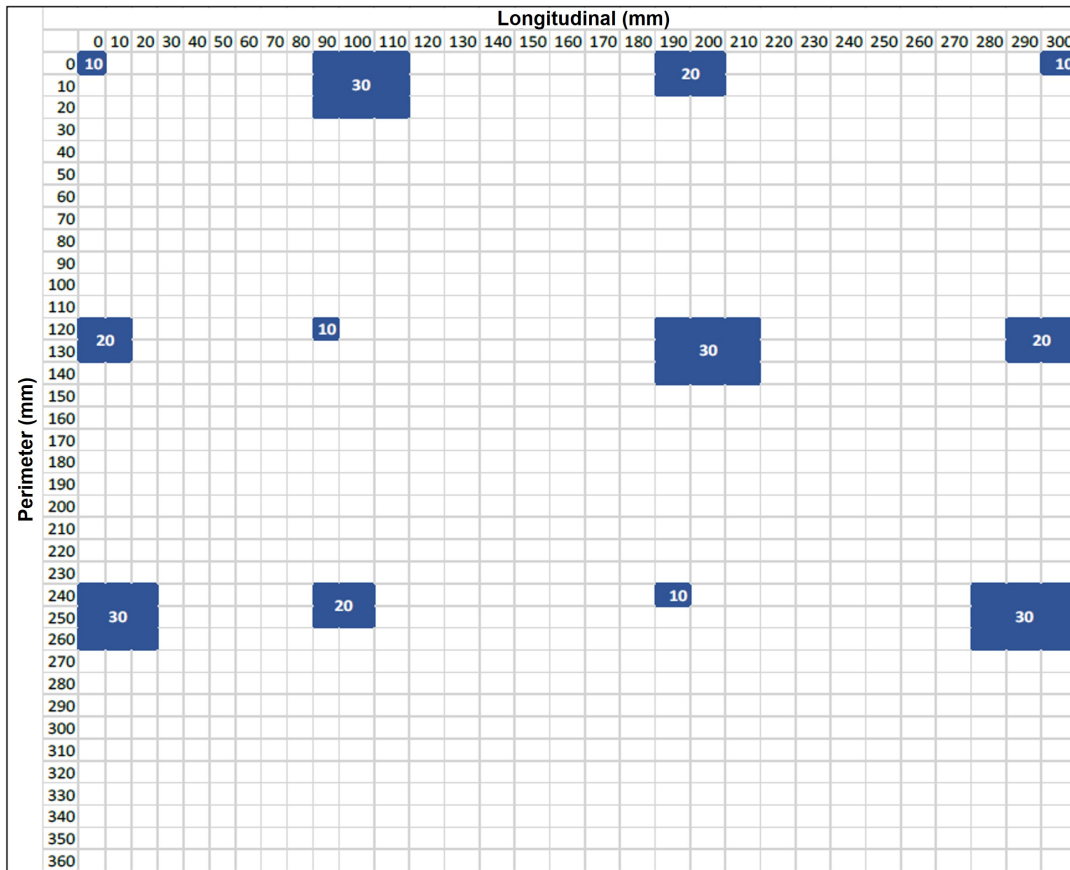


Figure 21: Artificial defect map. The Y axis represents the edges of the repaired area, while the X axis represents the length of the repair.

The artificial defects were positioned directly on the surface of the pipe, before the adhesive layer was applied, as seen in Figure 22. After all the defects were positioned, lamination occurred as all the other pipe samples.



Figure 22: Artificial defects positioned on the surface of the steel pipe, according the artificial defect map.

### 3.2. Salt Spray ageing

The salt-spray accelerated ageing was performed at the Composite Materials Laboratory of PUC-Rio from December 2020 to January 2023. Over the course of a little over two years, the repaired pipes were exposed to approximately 13,510 h of continuous ageing inside the salt-spray chambers. During the test, both extremities of the pipes were sealed to prevent water ingress and corrosion on the inner walls of the samples. At designated dates, the pipes were removed from the chambers for a period of two weeks in which the NDTs were performed. During this period outside the chambers, the pipes were protected with plastic film as best as possible from the dry environment of the laboratory in order to avoid excessive desorption and with bubble wrap to avoid accidental impact damage.

Three large scale chambers (Figure 23) were used and each one was set a different temperature. The objective was to evaluate how degradation occurred in different ageing rates and to have enough data to predict life in service of the repair.

The temperatures selected were of 35 °C, 55 °C and 70 °C. The first one was the temperature recommended by ASTM B-117 [127] for salt-spray testing. The other two were selected to test different ageing rates, leaving enough difference between temperatures to account for fluctuations in actual test temperatures. The higher temperature of 70 °C proved to be a challenge due to limitations of the equipment used. Thus, many problems and interruptions happened along the duration of the testing done

in this chamber. Table 4 shows the average temperature and standard deviation of each chamber for the duration of the tests.



Figure 23: 3 large-scale salt-spray chambers, with the respective control panels in the foreground. In the background, it is possible to observe the solution tanks next to one of the air/water saturators.

Table 4: Set, average temperature and standard deviation for each salt spray chamber.

|                          | <b>Chamber 1</b> | <b>Chamber 2</b> | <b>Chamber 3</b> |
|--------------------------|------------------|------------------|------------------|
| Set Temperature (°C)     | 35               | 55               | 70               |
| Average Temperature (°C) | 35.6             | 55.6             | 60.9             |
| Std. Deviation (°C)      | 0.9              | 1.6              | 6.1              |

The ASTM B-117 [127] and ASTM D-1193 [128] standards were used as reference for sodium chloride composition, salt water solution and salt spray concentrations and pH and water conductivity. These parameters were monitored during the preparation and maintenance of the tests. Table 5 shows the target values

for each parameter according to the aforementioned standards and Table 6 shows the maximum allowable amount of impurities in the composition of the sodium chloride used for testing.

Table 5: Salt spray preparation parameters reference values.

| Parameter                   | Value                  | Observations                  |
|-----------------------------|------------------------|-------------------------------|
| Salt Solution Concentration | 4-6%                   |                               |
| Salt Solution pH            | 6.5-7.2                | at $23 \pm 3^{\circ}\text{C}$ |
| Water Conductivity          | $< 5.0 \mu\text{S/cm}$ | ASTM D1193 - Type IV          |

Table 6: Maximum allowable amounts of impurities in the sodium chloride compositions.

| Impurity Description                                      | Allowable Amount    |
|---|---------------------|
| Total Impurities  | $\leq 0.3 \%$       |
| Halides (Bromide, Fluoride and Iodide) excluding Chloride | $< 0.1 \%$          |
| Copper  | $< 0.3 \text{ ppm}$ |
| Anti-caking Agents  | None Added          |

Testing was divided into intervals of ten weeks of ageing and two weeks of NDT testing. The only exceptions were the two intervals of ageing which were shorter to account for the more pronounced absorption experienced by the samples when first exposed to the salt spray. Table 7 lists the intervals, named T0 to T9, with their respective ageing time.

In each chamber, 8 pipes were conditioned. The list of where each sample was tested is provided in Table 8. Samples were positioned at the bottom of the chambers, in the same plane, to homogenize the ageing conditions as much as possible. The ends of the pipe were protected and partially sealed to minimize water ingress and internal corrosion. Figure 24 shows the samples positioned inside of the chambers.

Table 7: Intervals between NDT inspections and accumulated ageing time.

|    | Time Interval (h) | Accumulated Time (h) |
|----|-------------------|----------------------|
| T0 | 0                 | 0                    |
| T1 | 570               | 570                  |
| T2 | 1250              | 1820                 |
| T3 | 1670              | 3490                 |
| T4 | 1670              | 5160                 |
| T5 | 1670              | 6830                 |
| T6 | 1670              | 8500                 |
| T7 | 1670              | 10170                |
| T8 | 1670              | 11840                |
| T9 | 1670              | 13510                |



Figure 24: Pipes positioned inside one of the chambers. The samples marked by the red parallelograms are from the same manufacturer and were the ones used for this work. It is also possible to see the black end protection on each one.

Table 8: Samples and their respective chambers.

|        | Chamber 1 | Chamber 2 | Chamber 3 |
|--------|-----------|-----------|-----------|
|        | 1         | 3         | 6         |
|        | 2         | 5         | 11        |
|        | 7         | 9         | 12        |
| Sample | 8         | 10        | 13        |
| Number | 14        | 16        | 18        |
|        | 15        | 17        | 23        |
|        | 19        | 21        | 24        |
|        | 20        | 22        | 25        |

### 3.3. NDT Calibration procedures

#### 3.3.1. Shearography

The shearography inspection was performed by BAWSF Inspeções e Engenharia at PUC-Rio’s composite materials laboratory. The inspection procedure was developed by the company’s Level III inspector and the inspections were performed by the Level III inspector and a qualified technician with the setup shown in Figure 25.

The parameters used during inspection were provided by BAWSF Inspeções e Engenharia in their reports, as presented in Table 9.

Table 9: Software, equipment and loading parameters.

|                   | Parameters                     | Values        |
|-------------------|--------------------------------|---------------|
| Software          | Gain                           | Level 3       |
|                   | Shutter                        | Level 5       |
|                   | Phase Map Acquisition Time     | 40 s          |
|                   | Phase Map Acquisition Rate     | 1 phase map/s |
| Shearography Head | Model                          | N4f           |
|                   | F#                             | 6             |
|                   | Lateral Displacement Amplitude | 10 mm         |
|                   | Distance to Sample             | 320 mm        |
| LASER             | LASER Stabilization Time       | 15 min        |
|                   | LASER Wavelength               | 532 nm        |
|                   | LASER Coherence Length         | 300 m         |
|                   | LASER Power                    | 1 W           |
| Load              | Load Type                      | Thermal       |
|                   | Thermal Exposure Time          | 30 s          |

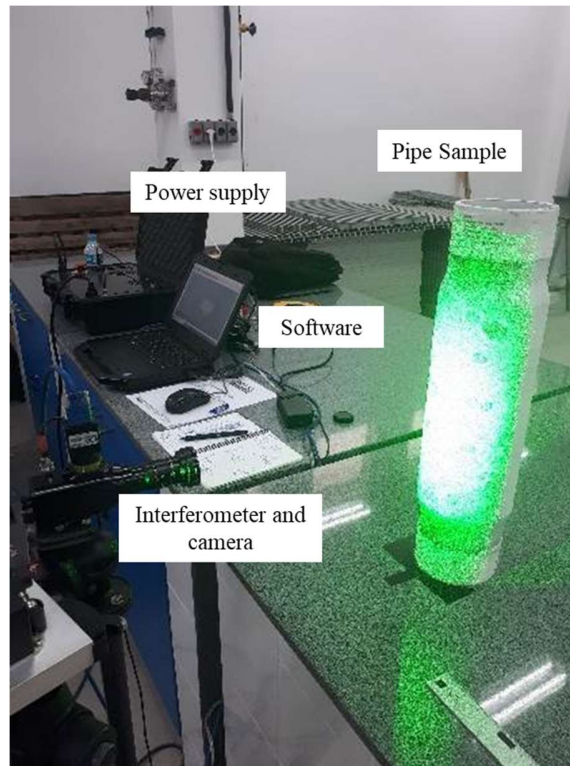


Figure 25: Shearography setup with most of the componentes displayed. Only the LASER source and the lamp used for thermal loading are not shown in this image.

Figure 26 shows the positioning of the samples in relation to the original (as acquired) images. The specimens were kept “upright” during the inspections, but the images were obtained “lying down” to optimize the resolution of the interferometer camera. In the reports, images were rotated by 90° (clockwise), representing the actual positioning of the specimens. The lateral displacements were applied longitudinally, from left to right in the image as captured by the interferometer and transversally, from bottom to top in the original image.

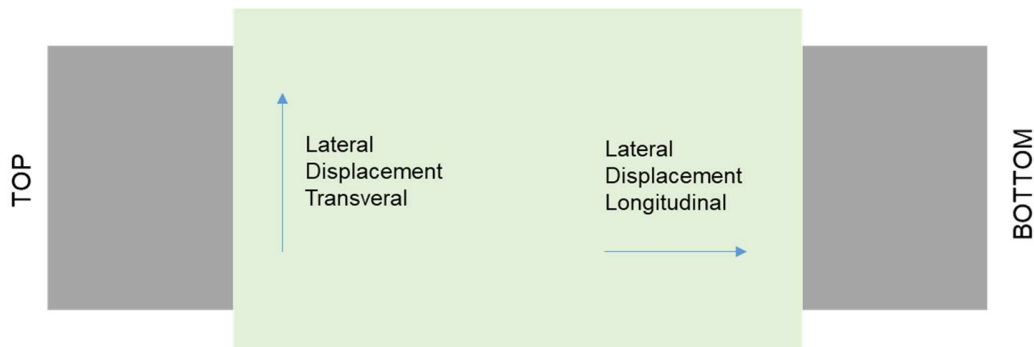


Figure 26: Positioning of the specimen in relation to the originally acquired images and the directions of the lateral displacements used.

The following are the steps of the inspection procedure used:

I) Application of talc powder spray (Metal-Chek™ D70): The repaired surface presented slightly different levels of transparency and reflection. Such characteristics make it difficult to obtain good quality images using the shearography technique. The use of matte white talc powder spray to coat the surface to be inspected solved the problem, without the need for post-painting or permanent painting.

II) Specimen positioning: All inspections were carried out with the same positioning of the specimen, lighting module, and vision module. For this, tripods and a bench available in the PUC-Rio laboratory were used. All positions were measured and referenced, ensuring the repetition of inspection conditions for all specimens. Each specimen was inspected in three distinct positions:  $0^\circ$ ,  $120^\circ$ , and  $240^\circ$ , starting with position  $0^\circ$ .

III) Inspection selection: Inspection selection is carried out in a proprietary software developed by BAWSF, so that all images are saved in the corresponding folder of each inspection. Inspection is understood as the set of information: identification of the specimen (00 to 25), position of the specimen ( $0^\circ$ ,  $120^\circ$ , or  $240^\circ$ ), and lateral displacement (transverse or longitudinal).

IV) Lateral displacement adjustment: The tilting mirror in the interferometer was adjusted to obtain laterally displaced images with an amplitude of 10 mm, both in the longitudinal and transverse directions.

V) Thermal loading: Thermal loading was performed using a 500 W halogen lamp. Loading was applied to ensure homogeneous heating throughout the extent of

the repair. Thermal loading was applied for 30 seconds with oscillatory movement of the lamp (approximately 7 cycles) over the entire extent of the repair.

VI) Obtaining the Reference Image: A phase image (Reference) was obtained for further processing. It is important to note that in this case, the Reference was obtained after thermal loading. The practical effect is that the other Phase Maps were obtained during the cooling of the specimen, making the temperature variation between the Reference and the Phase Maps smaller, reducing the risk of correlation loss during inspection.

VII) Obtaining New Phase Maps: New Phase Maps were acquired for 40 seconds at a rate of one Phase Map per second, for a total of 40 images.

VIII) Selection of Phase Maps: A preliminary analysis of the images was performed, with the selection of Phase Maps whose difference presents the fringes of greatest interest for each inspection.

IX) Application of Filter: A low-pass filter was applied to the Phase Map Difference, improving the image quality and facilitating the interpretation of interference fringes.

X) Fringe Animation and Saving of Phase Map Difference Image: The animation of fringes allowed for, in tandem with the experience of the operator, differentiation of the fringes coming from defects from those coming from inherent interference in the measurement process. In addition, animation allows for the selection of the best images to be analyzed. Subsequently, the best image obtained was archived in the corresponding inspection folder.

### **3.3.2. Ultrasound**

The ultrasound inspections were performed by the Laboratory of Non-Destructive Testing, Corrosion and Welding (Laboratório de Ensaios Não Destrutivos, Corrosão e Soldagem - LNDC) of COPPE/UFRJ. All inspections were performed by the LNDC's senior researcher and qualified technicians at PUC-Rio's composite materials laboratory using the setup shown in Figure 27.

Before the inspection of the pipes, a preliminary study was carried out by LNDC to determine the best configurations to be used regarding the choice of transducer, the geometry of the water column, water flow, methodology for signal analysis, and other parameters under analysis. The parameters chosen for inspection were presented by LNDC in their reports, and can be found below:

- Ultrasound equipment: OLYMPUS OMINISCAN MX2;
- Transducer: Olympus C539-SM Normal Incidence and Longitudinal Wave Transducer
- Frequency: 1 MHz;
- Compact water pump to maintain the water flow through the water column;
- Encoders for measuring the transducer displacement in the longitudinal and circumferential axis and of the pipes;
- Matlab software version 2018.



(a)



(b)

Figure 27: Ultrasound inspection setup: a) Pipe support with water being used as coupling medium being pumped from below; b) Omniscan MX2 data acquisition device.

In order to understand the behavior of the ultrasonic signal in the repaired region, points were chosen from the areas of the reference pipe which did not have artificial defects and the A-Scan was analyzed. Figure 28 shows a typical A-Scan obtained from these areas, where it is possible to observe three distinct regions. The first one is related to the echo generated by the interface between the water column and the upper surface of the composite. The second region refers to the echo coming from the interface between composite and steel pipe and first steel background echo. Finally, the third region comprises the second reflection signal from the steel background echo.

Based on these A-scans, as part of the methodology chosen for the inspection, 3 gates were positioned for the analysis of the signal amplitude, based on the regions previously identified. Gate I (yellow): encompasses the entire signal. Gate A (red): covers the range containing the composite/steel pipe interface signal, first background echo and the region where defects signal would appear. Gate B (green): corresponds to the second steel background echo.

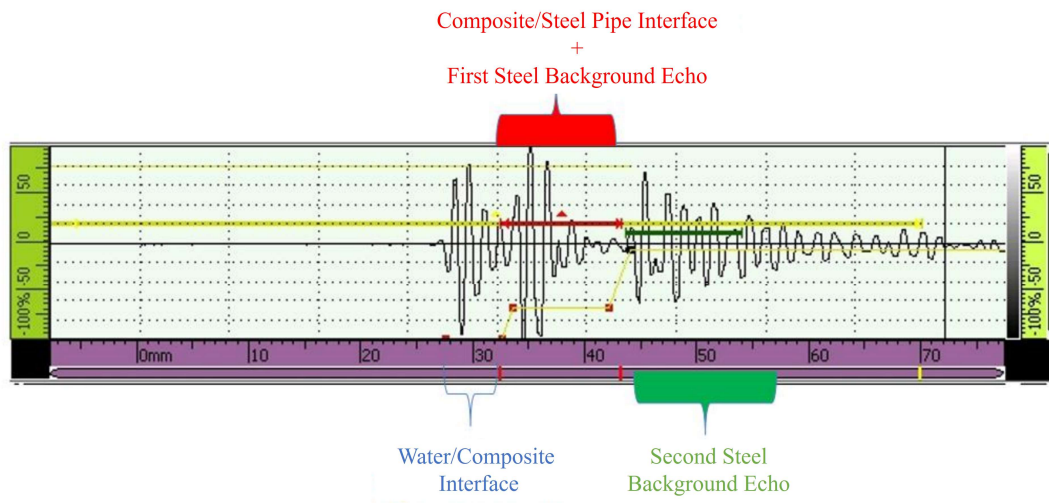
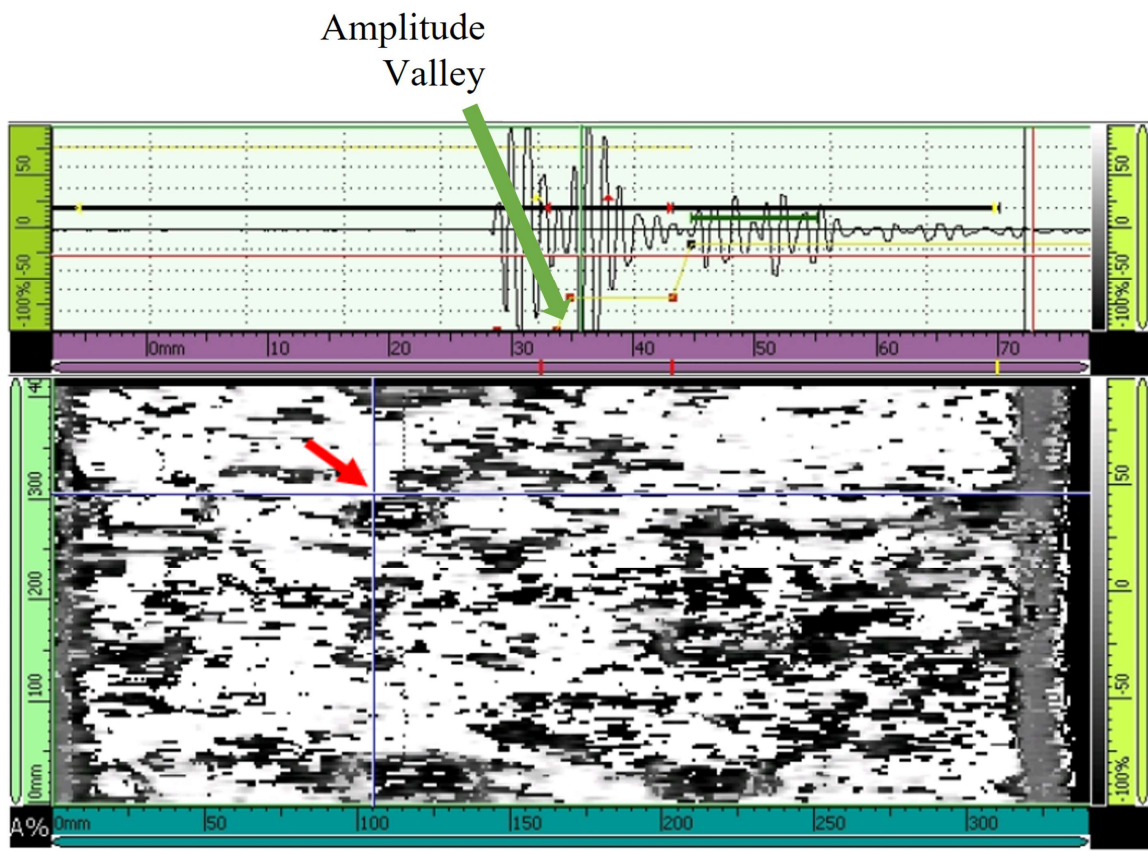


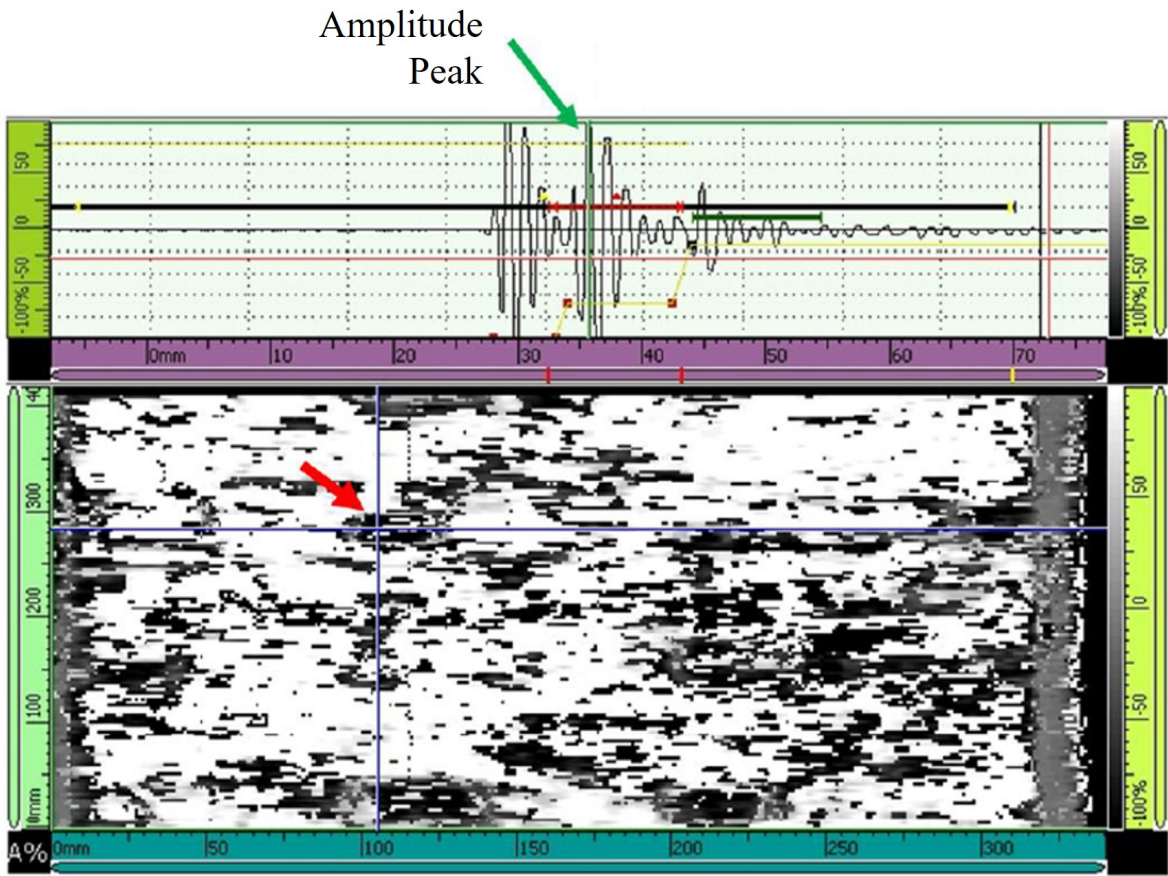
Figure 28: A-Scan obtained from defect free areas of the repair. In yellow, red and green are the gates selected for analysis. In blue is the region of the signal that represents the water/composite interface.

In each inspection, the pipes were inspected in a raster pattern, with the transducer running longitudinally from side to side collecting data. After a complete line has been inspected, an automated system rotated the pipe for a certain amount, measured by the encoder. The direction of rotation was the same in every sample at each inspection.

At each data point acquired, the A-Scan was analyzed. The phase inversion criterion was applied at Gate A to evaluate whether a defect is present. Although the differences in acoustic impedance and signal characteristics between composite and the steel pipe do not cause significant changes in the amplitude of the signal reflected from the interface, the presence of an air gap can cause such changes. An air gap can be caused by a defect at the interface between the composite and the steel pipe and it would cause the amplitude to change from a valley, where there are no defects, to a peak, where there are defects, according to the preliminary testing carried out by LNDC, as can be seen in Figure 29.



(a)



(b)

Figure 29: A-Scan representation of the area indicated in red, in the C-Scan: a) Area in the C-Scan showing no defects appears as an amplitude valley in the indicated area of the A-Scan; b) Area in the C-Scan showing defects appears as an amplitude peak in the indicated area of the A-Scan.



## 4. Results and Discussion

Throughout the periodic inspections, it was possible to observe how severe the effects of the salt-spray ageing were. Figure 30 shows samples during the T3 (approx. 3,400 h) inspection, in comparison with an unaged sample in the far left. It is possible to observe that corrosion had already spread throughout the entirety of the exposed metal area and was “overflowing” to areas of the edges of the composite and areas of painted pipe. Also of note was the changes in color suffered by the polymeric matrix of the composite repair. The light green hue of the unaged samples turned ever so more yellow as the time of test and harshness of condition (temperature, in this case) increased, with chamber 3 samples showing a stronger yellow tint than all of the others. This color change can be attributed to chemical reactions linked to thermo-oxidation of the epoxy resin [129].



Figure 30: Steel pipes with FRP repairs in different states of degradation after salt-spray ageing: left: unaged pipe; middle: pipe conditioned for approx. 3.400h at 55°C; pipe conditioned for the same amount of time, but at 70°C showing signs of higher degradation.

## 4.1. NDT Inspections

### 4.1.1. Reference Pipe

The results for both ultrasound and shearography are shown in Figure 31. Shearography was able to detect 10 out of 12 artificial defects, while ultrasound detected 6 out of 12. Both techniques showed good accuracy regarding the position of each detected defect. Ultrasound was not able to detect any of the 10 x 10 mm defects while shearography did manage to detect 2, one of them at the edge of the repair. Of the 20 x 20 mm defects, shearography was able to detect all of them, while ultrasound detected 3 out of 4, with the undetected one at the edge of the repair. The same results occurred for the 30 x 30 mm defects, with the undetected defect by the ultrasound on one of the edges of the repair. A summary of the results is shown in Table 10.

At the extreme edges of the repair, there is a 20 mm taper to smooth the transition between the thickness of the repaired area and the steel pipe. The tapered area is epoxy coated, with the same epoxy adhesive used between the composite and steel pipe, for protection. As the defects were placed just after the transition of the taper region and the beginning of the repair length, this may have affected the performance of both techniques, but more so in the UT. The single transducer pulse-echo methodology used during UT may not be accurate enough to detect very small defects in regions close to the edges of the repair, especially close to this thickness transition.

Table 10: Results for each technique segmented by defect size and position. Units in mm.

|              | Borders |       |       | Middle |       |       | % detected |
|--------------|---------|-------|-------|--------|-------|-------|------------|
|              | 10x10   | 20x20 | 30x30 | 10x10  | 20x20 | 30x30 |            |
| Shearography | 1       | 2     | 2     | 1      | 2     | 2     | 83%        |
| Ultrasound   | 0       | 1     | 1     | 0      | 2     | 2     | 50%        |

The detection of the artificial flaws using shearography is in agreement with Soares et al. [11], who were also able to detect plastic tapes acting as defects in their experiment. The authors managed to detect artificial flaws ranging from 10x10 mm to 25x25 mm under 6 mm thick repair, similar to those tested in this work. The UT

performance was similar to that observed by de Almeida et al. [125] using a very similar methodology. Hasiotis et al. [16] experienced difficulties when using UT to detect flaws embedded in GFRP composites. Although using not exactly the same configuration as the reference samples in this work, the authors concluded that the glass fibers present in the composite generated reflections that ended up making the determination of the defect location, size and shape less accurate, which may also have occurred in the present case. Generally, the anisotropic nature of the GFRP seemed to affect UT more than SH.

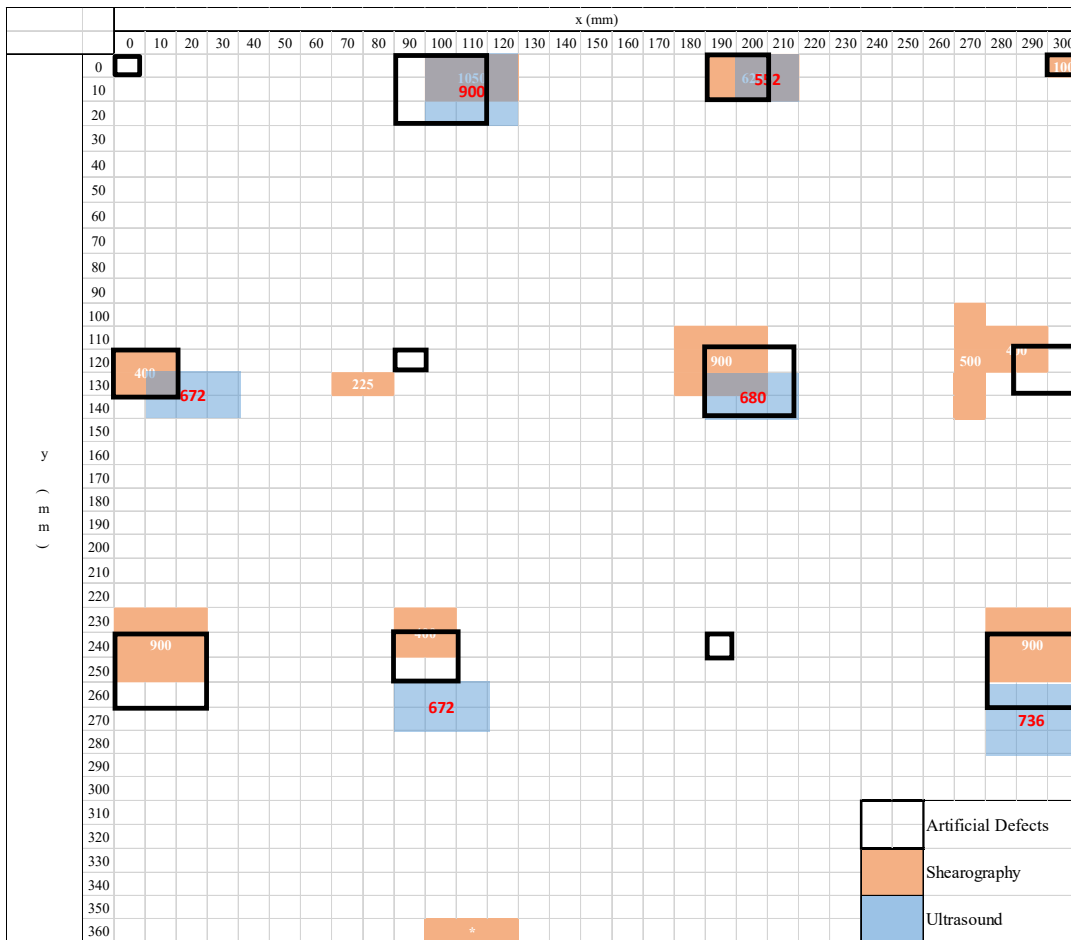


Figure 31: Ultrasound and shearography results overlaid in the artificial defect map. The numbers inside the indications represent the area of each defect in mm<sup>2</sup>.

#### 4.1.2. Aged Pipes Monitoring

From December 2021 to January 2023, 24 samples were inspected by shearography and ultrasound. The time intervals between inspections was of 10 weeks or, approximately 1,670 h. The first two inspections were more closely spaced to account for Fickian absorption occurring in the composite used in the repairs. Composite water uptake was measured according to ASTM D570 and ASTM D5229/5229M [130, 131], using 4 samples (Figure 32) in each chamber which were exposed to the salt spray at the same time as the pipes.

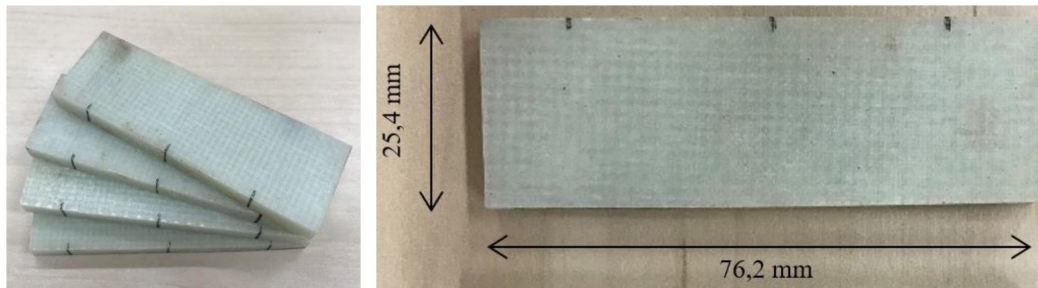


Figure 32: Samples used for water uptake measurements.

Figure 33 shows the mass gain experienced by the absorption samples as a function of time. All chambers showed a very pronounced initial gain, as predicted by the Fickian model. Samples in chamber 1 (35°C) behaved in a very progressive way, with mass gain tapering off with time up until T7 (approx. 10,000 h) when it seemed to have reached saturation. Samples in chamber 2 (55°C) went into a plateau from T2 to T4, after the initial mass gain. Afterwards, mass gain steadily increased until it peaked around T6 (approx. 8,500 h), after which it suffered mass loss, indicating that saturation was already reached and caused permanent damage. The initial mass gain was significantly more pronounced in chamber 3 (70°C) and was followed by a steady apparent mass loss, probably caused by desorption. After T4, similar to chamber 2, mass gain increased until it reached a peak around T6. Again, similar to chamber 2, mass loss followed indicating that saturation has been reached.

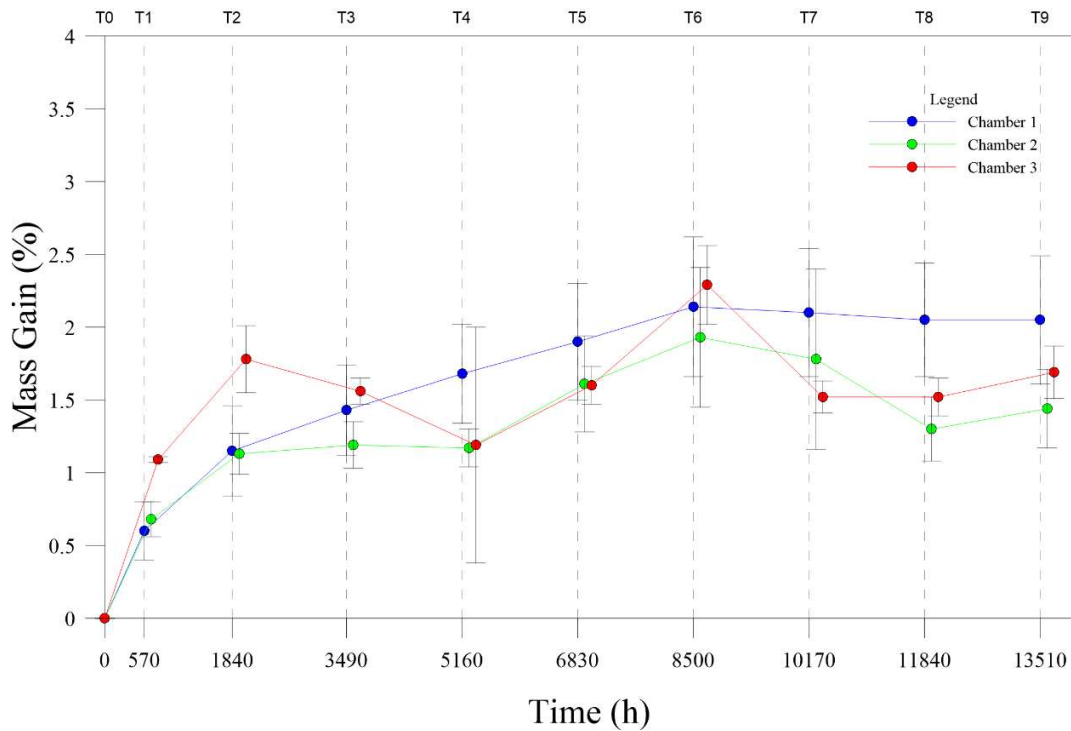


Figure 33: Mass gain % as a function of time. Chambers 2 and 3 reached saturation before chamber 1.

The similar behavior of chambers 2 and 3 could be explained by problems with the equipment used. As the conditions in chamber 3 were very extreme, there were circumstances where testing had to be interrupted momentarily to perform repairs. During these periods, the other two chambers had to be paused as well in order to keep sync between all of the ageing times without compromising NDT schedule. Those periods occurred mainly between T2 and T4, which could explain the unexpected behavior of the samples at this interval. It is likely that the desorption experienced by samples in chamber 3 happened mainly because of high temperature causing evaporation of the moisture when the equipment was paused. Chambers 1 and 2 were less susceptible to this effect because of the lower temperatures, although the plateau behavior displayed by chamber 2 may indicate that some evaporation did occur during this time as well.

In general, the behavior of the samples was similar to the work of Tual et al. [55], in which higher conditioning temperatures produced higher rates of absorption initially and then stabilized over time as saturation approached.

#### 4.1.2.1. Shearography

Shearography defect indications were divided into three categories, as seen in Figure 34: defects (red), areas of interest (yellow) and superficial defects (blue). The areas marked in red were what the operator confirmed as defects, by analyzing the fringe pattern movements. The yellow markings were areas that were considered to be potential defects, as the fringe patterns were present but not as well defined as on the areas marked in red. These areas would not be considered defects in a field inspection, so they were not taken into account when measuring defective areas or counting defects. Blue markings were minor surface defects, which do not affect the performance of the repair and were also not taken into account. When there are grey dashed lines inside a red, yellow or blue area, the marked area grew when compared to previous inspections. The grey dashed lines represent the previously detected region, while the colored marking indicates the region detected in the last inspection performed.

Table 11, Table 12 and Table 13 lists the shearography detections before the accelerated ageing began, with the samples in an as-manufactured condition. As expected, the defect indications were very small with a few exceptions, such as pipes numbers 6, 12 and 18.

Throughout the ageing process, the samples were monitored for growth of existing defects and onset of new ones (Table 14). Of all the pipes with defects at T0, pipes 6, 7, 12 and 16 had defective area growth. Pipes 6, 7 and 12 experienced only growth of existing defects, while in pipe 16 new defects appeared.

Samples 6 and 12 were aged in the chamber 3 (70 °C) under the most severe conditions and suffered the most pronounced defect growth, which happened from T1 to T5, after which it almost completely stopped. The defect peak growth for samples 6 and 12 occurred at T2 and T3. The defect growth period coincided with the time

interval in which mass gain occurred in the absorption samples in chamber 3, which lasted until about T6, where saturation seems to have been reached. Most of the defect growth occurred until around T3, which would also coincide with the period of highest mass gain rate, showing a possible correlation between water uptake and defect propagation rate.

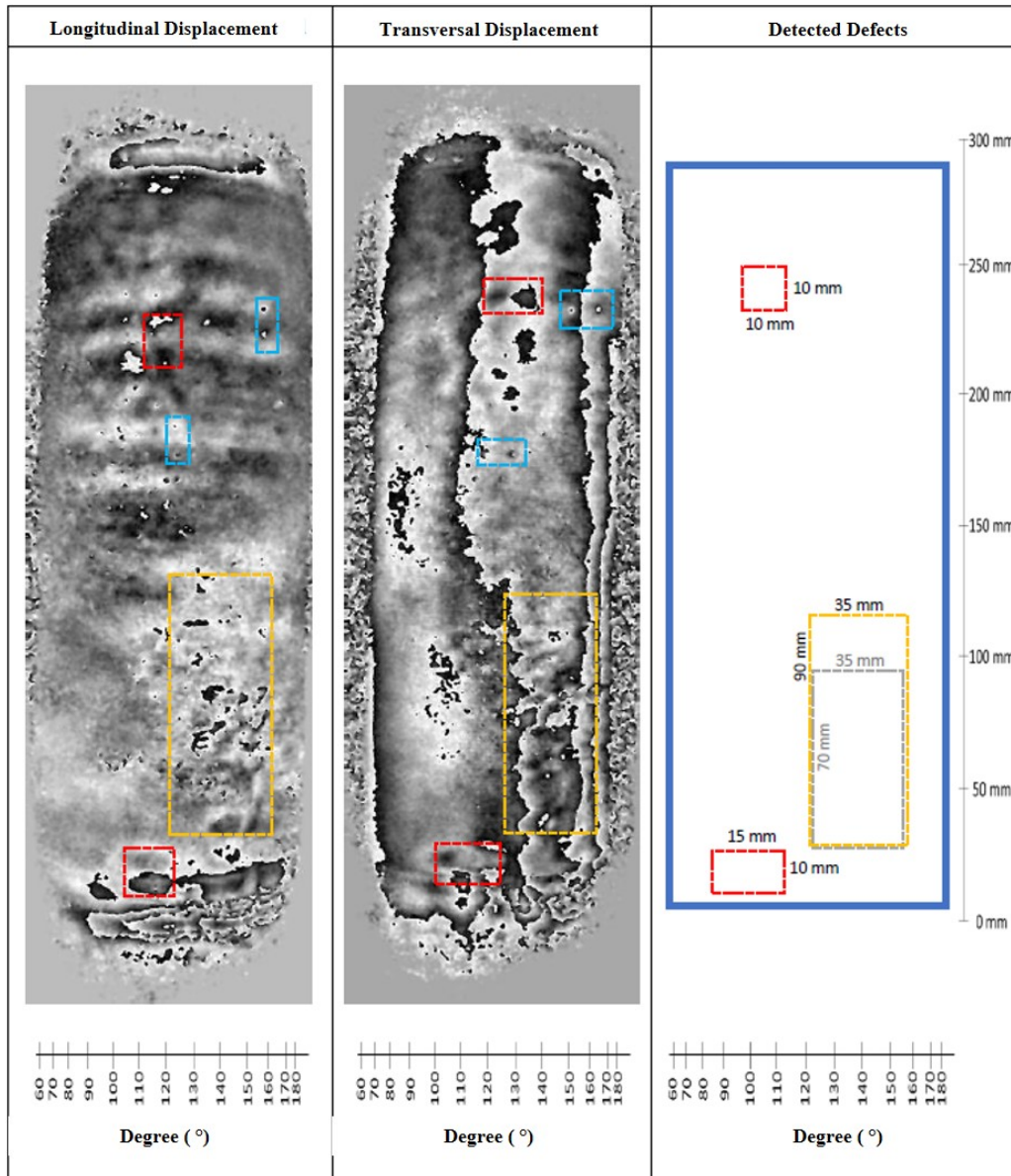


Figure 34: Example of a sample (#2) with the three different defect indications seen in shearography inspection: red markings indicate defective areas; yellow markings indicate potential defective areas; blue markings indicate minor surface defects.

Table 11: Shearography defect detections pre-ageing in samples to be conditioned in chamber 1.

| Pipe | Defects | At/near edges | Towards the middle | Observations                            |
|------|---------|---------------|--------------------|---|
| 1    | Yes     | 1             | 1                  | Two small indications, one at a edge.   |
| 2    | Yes     | 1             | 2                  | Three small indications, one at a edge. |
| 7    | Yes     | 1             | 0                  | A small/medium indication at a edge.    |
| 8    | No      | -             | -                  | -                                       |
| 14   | No      | -             | -                  | -                                       |
| 15   | No      | -             | -                  | -                                       |
| 19   | No      | -             | -                  | -                                       |
| 20   | No      | -             | -                  | -                                       |

Table 12: Shearography defect detections pre-ageing in samples to be conditioned in chamber 2.

| Pipe | Defects | At/near edges | Towards the middle | Observations  |
|------|---------|---------------|--------------------|---|
| 3    | No      | -             | -                  | -   |
| 5    | No      | -             | -                  | -   |
| 9    | No      | -             | -                  | -   |
| 10   | No      | -             | -                  | -   |
| 16   | Yes     | 1             | 0                  | A small indication close to one of the edges.             |
| 17   | Yes     | 0             | 1                  | A very small indication towards the middle of the repair. |
| 21   | No      | -             | -                  | -   |
| 22   | Yes     | 1             | 0                  | A small indication at a edge.                             |

Table 13: Shearography defect detections pre-ageing in samples to be conditioned in chamber 3.

| Pipe | Defects | At/near edges | Towards the middle | Observations  |
|------|---------|---------------|--------------------|---|
| 6    | Yes     | 2             | 0                  | Two very large indications at edge.   |
| 11   | No      | -             | -                  | -   |
| 12   | Yes     | 2             | 1                  | Two large indications close to edges and one smaller indication a little further away.    |
| 13   | No      | -             | -                  | -   |
| 18   | Yes     | 2             | 0                  | A small/medium indication close to one of the edges and a medium indication at the other. |
| 23   | No      | -             | -                  | -   |
| 24   | No      | -             | -                  | -   |
| 25   | Yes     | 2             | 0                  | One small indication at each edge.  |

Pipe 7 was conditioned in chamber 1 (35 °C) and experienced only a slight growth of its existing defect from T0 to T1, which remained stable throughout the experiment. The only defect growth occurred in the period of peak mass gain

experienced by the samples in that chamber. This would also indicate a possible correlation between water uptake and defect propagation, since absorption rate is maximum when the concentration gradient is the greatest, thus causing a significant driving force for defect growth, especially when located in the repair edges.

Pipe 16 was conditioned in chamber 2 (55 °C) and saw two new small indications appearing in T2 and T3, respectively, both in areas near or at edges. All defects remained stable throughout the experiment. This sample was the only one that showed new defects appearing during ageing. Again, it was possible to correlate the appearance of new defects with the initial periods of ageing, which accounted for most of the mass gain for all chambers. The early stages of ageing provided the strongest driving force for moisture propagation at the steel pipe/composite interface through edge defects. Additionally, during this initial period, samples were subjected to significant temperature changes, especially in chambers 2 and 3, which could cause shear forces at the steel/composite interface due to the differences in thermal expansion coefficients between the two materials.

In general, the defect growth phenomenon seems to have been greatly influenced by the differences in moisture concentration between the samples and the ageing environment. Growth peaked between T2 and T3 and then declined as samples got closer to saturation. Additionally, the presence of defects at T0 was an important factor, which can also be linked to water uptake. Samples #6 and #12 showed large areas of defects at T0, especially near or at the edges of the repair, which may have acted as sites for water ingress and corrosion, which may have spread along the interface causing defect growth.

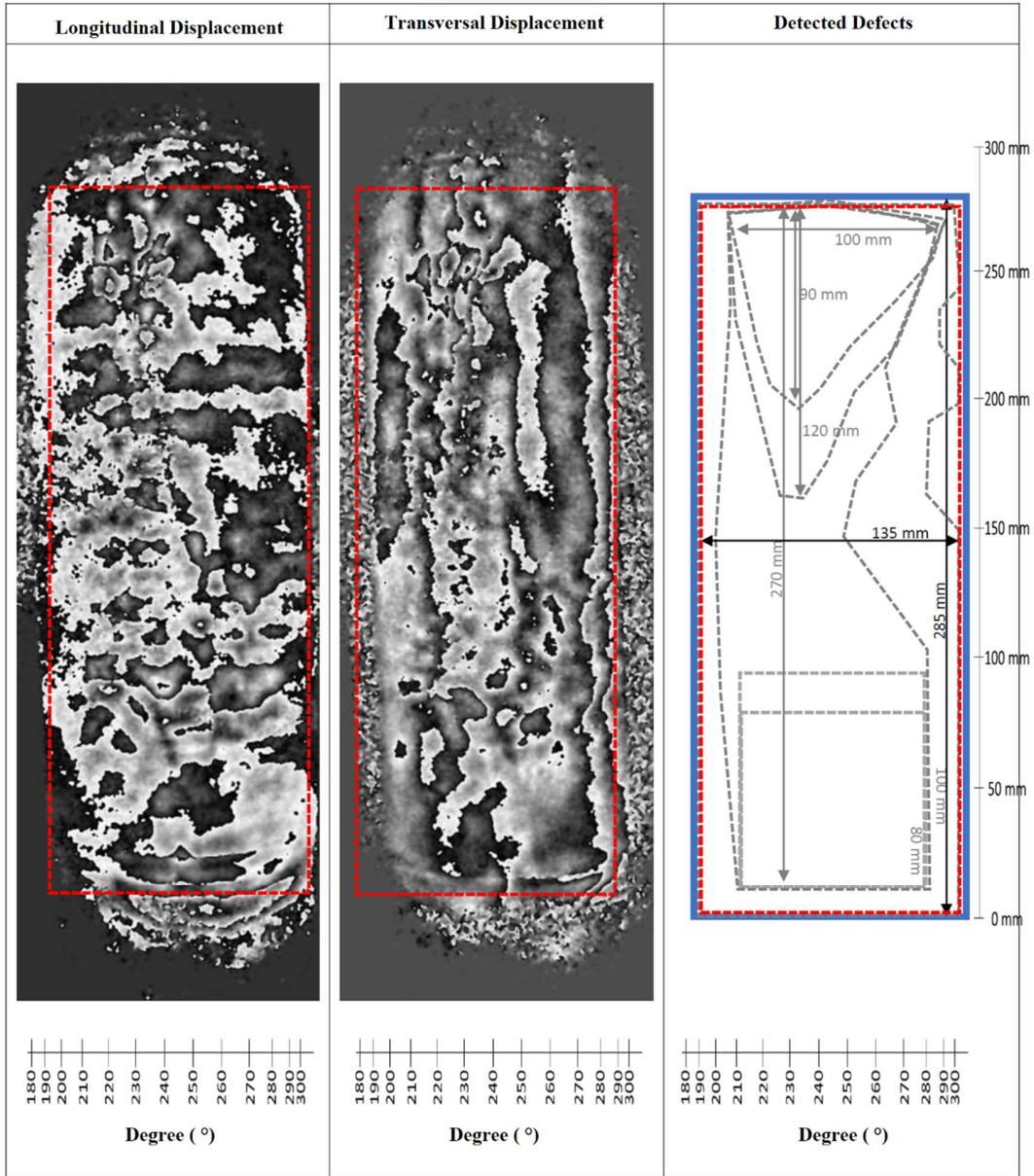
Figure 35 shows the shearography images for the four pipes that showed evolution in detections over time. Each figure is one of three sets of images that compose the whole rotation of the pipe. Images were captured at positions 0°, 120° and 240°, thus, for each sample, that were 6 images, divided in 3 sets of 2 (one with longitudinal and one with transversal displacements). The grey dashed lines and arrows represent the evolution of detections along the inspection intervals and the red dashed line represents the last inspection made on that sample. Blue dashed lines represent

minor surface defects, mainly caused by small resin bubbles gassing out, that were not taken into account.)

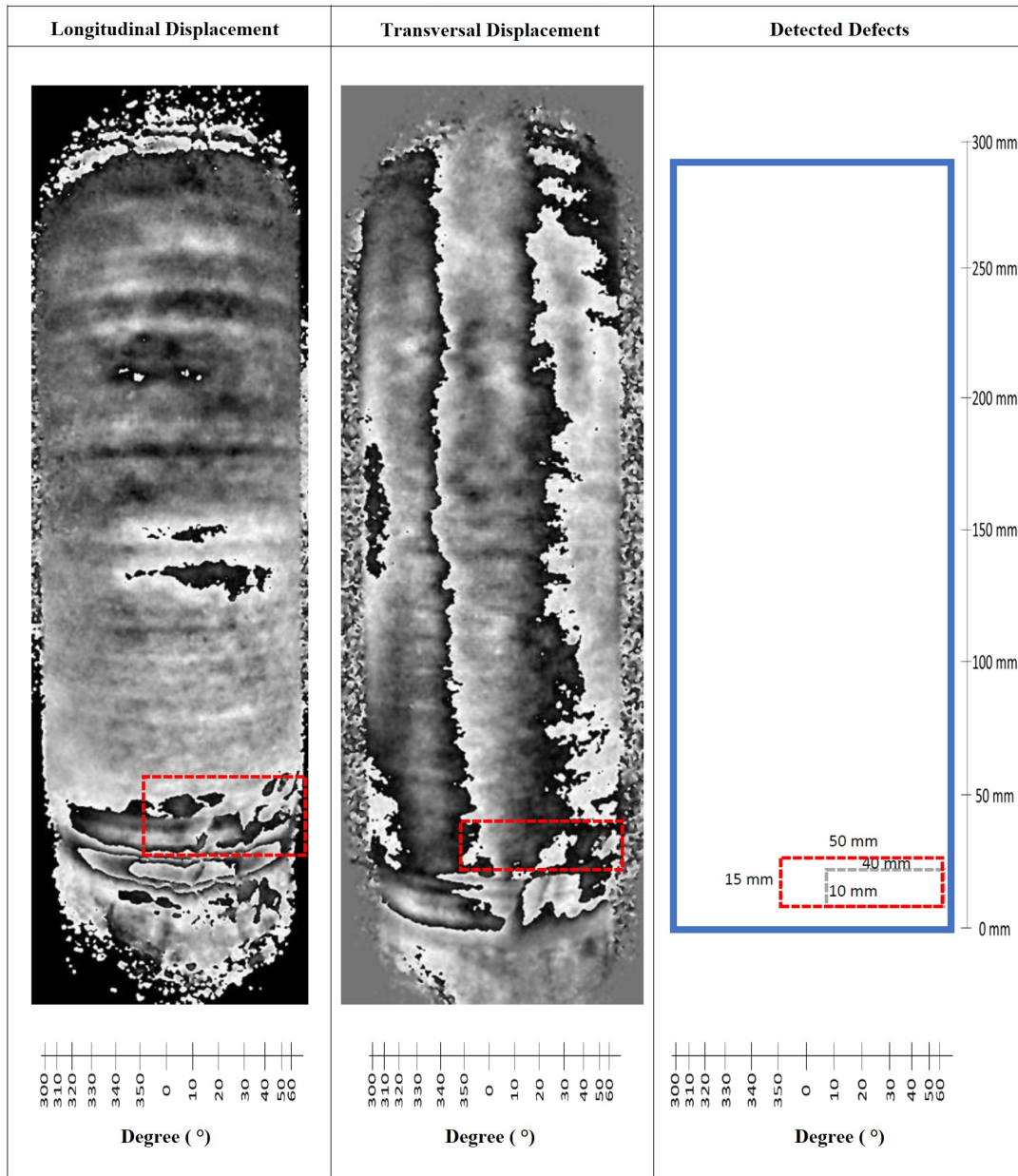
Table 14: Shearography detections during periodic inspections.

| Pipe | Area detected (mm <sup>2</sup> ) |                 |                 |                  |                |                 |       |                |       |       |
|------|----------------------------------|-----------------|-----------------|------------------|----------------|-----------------|-------|----------------|-------|-------|
|      | T0                               | T1              | T2              | T3               | T4             | T5              | T6    | T7             | T8    | T9    |
| 6    | 15400                            | 20000<br>(+30%) | 27000<br>(+35%) | 57000<br>(+111%) | 61275<br>(+8%) | 78450<br>(+28%) | 78450 | 78450          | 78450 | 78450 |
| 7    | 400                              | 750<br>(+88%)   | 750             | 750              | 750            | 750             | 750   | 750            | 750   | 750   |
| 12   | 1850                             | 4625<br>(+150%) | 7475<br>(+62%)  | 25775<br>(+245%) | 28175<br>(+9%) | 29075<br>(+3%)  | 29075 | 30275<br>(+4%) | 30275 | 30275 |
| 16   | 100                              | 100             | 300<br>(+200%)  | 400<br>(+33%)    | 400            | 400             | 400   | 400            | 400   | 400   |

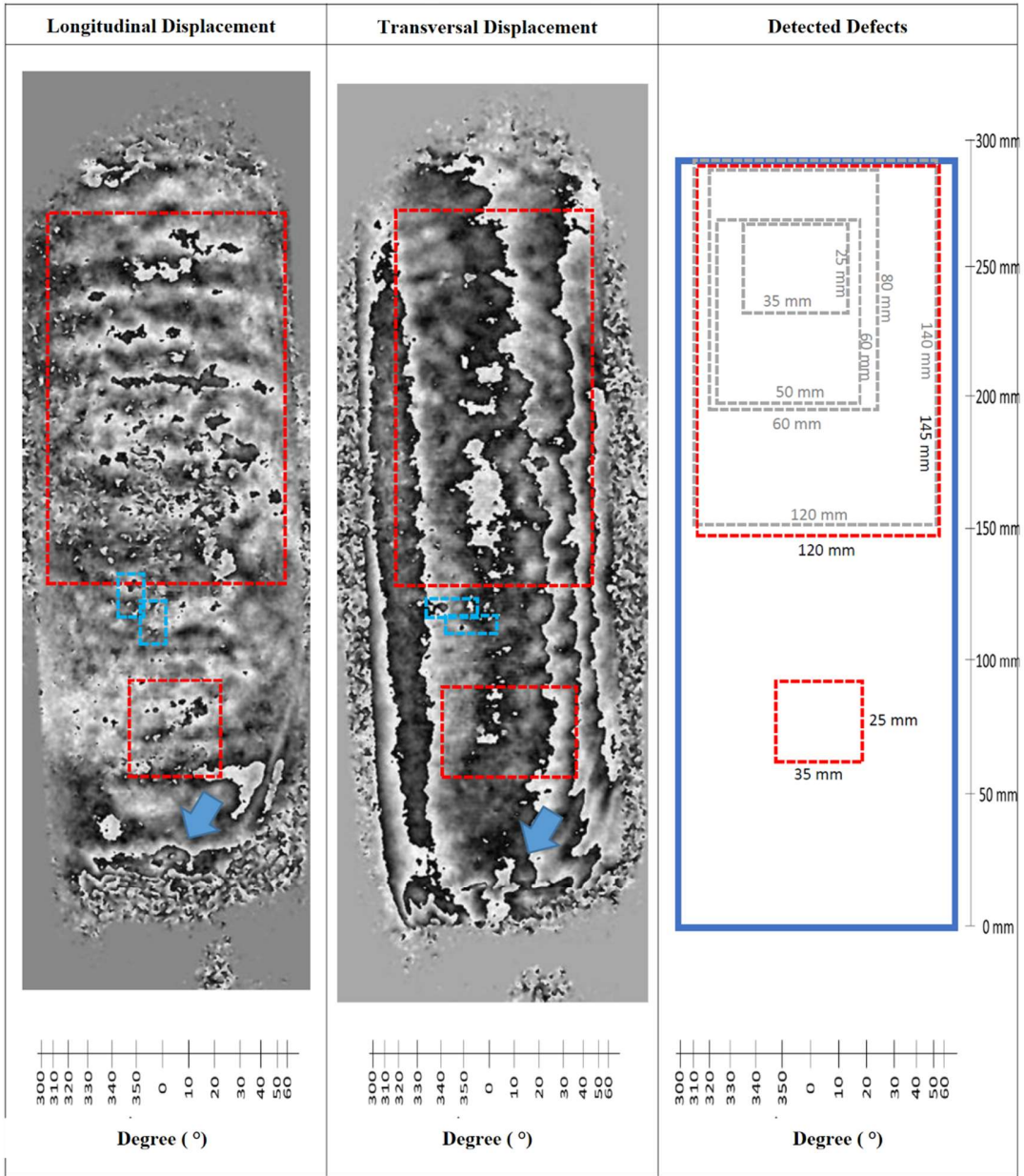
In general, the type of defects and their indications provided by the technique are very similar to what other authors have previously found. Soares et al. [11] found evidence of similar defects in onshore and offshore pipeline inspections, in repaired pipelines very closely related to the ones in this work, both in terms of materials and thickness.



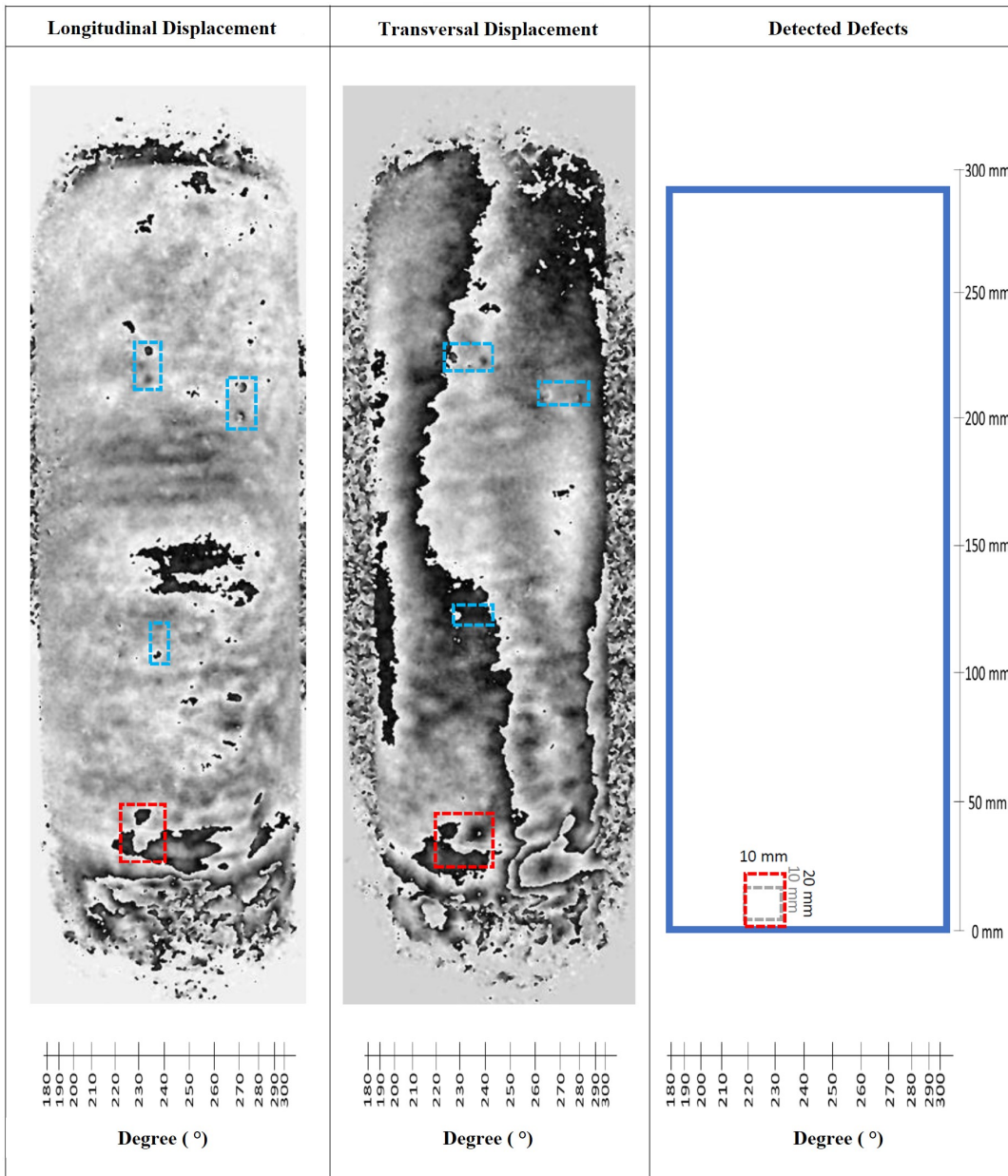
(a)



(b)



(c)



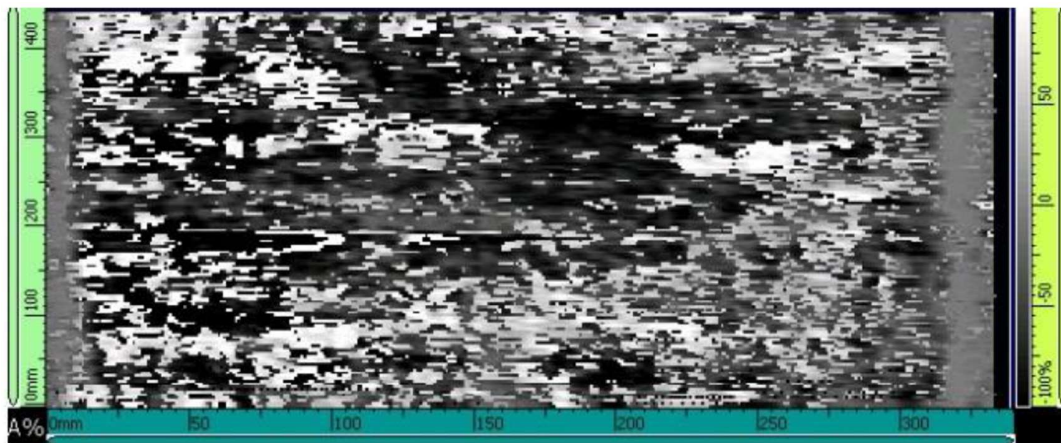
(d)

Figure 35: Shearography results showing the evolution of detections through time. Grey dashed lines represent past detections, while red dashed lines represent the last inspection performed. Blue dashed lines are surface defects. (a) Pipe 6, position 240°; (b) Pipe 7, position 0°; (c) Pipe 12, position 0° - blue arrow at the bottom indicates an area of possible defect detections in the future, based on fringe movements; d) Pipe 16, position 240°.

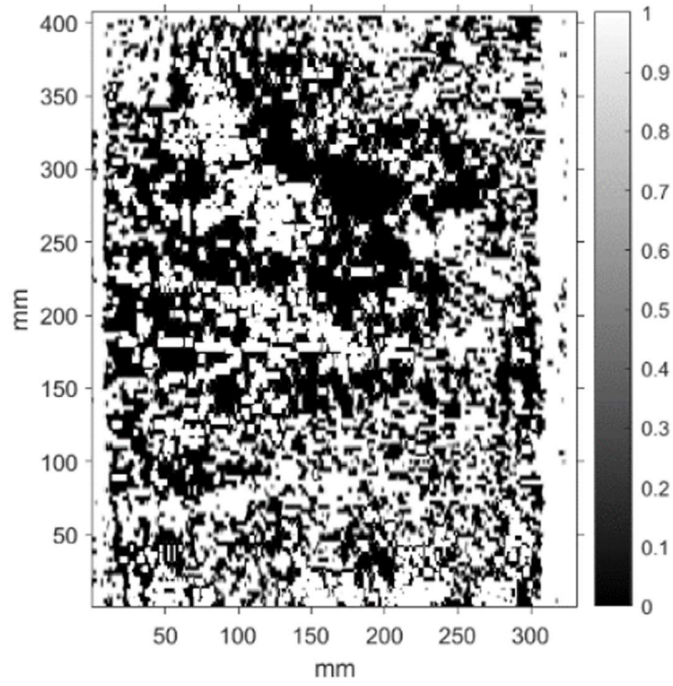
#### 4.1.2.2. Ultrasound

In Figure 36, the data analysis workflow for the ultrasound inspection is presented. For each specimen, the original C-Scan (Figure 36 a) obtained directly from the Ominiscan equipment without any signal or image processing was presented. For a more detailed analysis of the signal corresponding to the repair regions, Matlab software version 2018 was used with a proprietary routine developed by LNDC. For the analysis routine, it was necessary to insert the images from the C-Scan from the equipment (Figure 36 a), and from the initial analysis in Matlab, proceed with the selection of the signals of interest, binarization (Figure 36 b), and identification of regions with characteristics associated with discontinuities, which are delimited by the blue area (Figure 36 c).

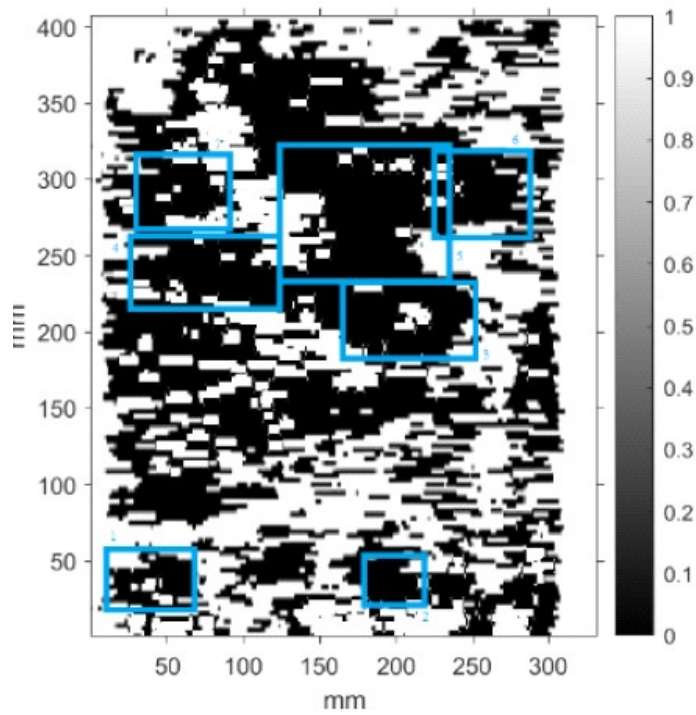
Table 15, Table 16 and Table 17 show the detections for all the samples before ageing began (T0), with the pipes as fabricated. Unexpectedly, In the case of ultrasound, all pipes showed defective areas. Most indications happened in areas close to or on the edges.



(a)



(b)



(c)

Figure 36: Ultrasound image processing workflow: a) C-Scan straight out of the equipment; b) binarized image; c) binarized image with defect indications.

Table 15: Ultrasound defect detections in pipes pre-ageing, for pipes to be conditioned in chamber 1.

| Pipe | Defects | At/near borders | Towards the middle | Observations  |
|------|---------|-----------------|--------------------|---|
| 1    | Yes     | 4               | 2                  | Multiple indications, mostly medium to large sizes.   |
| 2    | Yes     | 3               | 0                  | One very big indication at a border, 2 small/medium sized near borders.   |
| 7    | Yes     | 2               | 4                  | A cluster of small/medium defects that spans from the middle of the repair towards one of the borders. One detached medium detection towards the middle.                              |
| 8    | Yes     | 5               | 1                  | A cluster of medium to large defects located at one of the borders, with one detached small/medium indication at the other border. A detached indication at the middle of the repair. |
| 14   | Yes     | 1               | 1                  | Two small/medium detections.  |
| 15   | Yes     | 1               | 2                  | A single cluster of medium and large defects going from the middle of the repair towards one of the borders.  |
| 19   | Yes     | 1               | -                  | One large indication at one of the borders, going towards the middle of the repair.   |
| 20   | Yes     | 3               | -                  | One very large and two large indications at and/or near one of the borders, going towards the middle.   |

Table 16: Ultrasound defect detections in pipes pre-ageing, for pipes to be conditioned in chamber 2.

| Pipe | Defects | At/near borders | Towards the middle | Observations   |
|------|---------|-----------------|--------------------|--|
| 3    | Yes     | 4               | 1                  | Multiple small to medium sized indications.  |
| 5    | Yes     | 2               | 1                  | A large and a small indication very close together at a border, one medium sized indication towards the middle.                                      |
| 9    | Yes     | 1               | 2                  | Two medium sized indications towards the middle of the repair. One medium indication near the border region.   |
| 10   | Yes     | -               | 2                  | One large and one medium indication in the middle of the repair.   |
| 16   | Yes     | 3               | 0                  | A single cluster of small/medium indications in one of the borders.  |
| 17   | Yes     | 2               | 0                  | A very large indication going from the middle of the repair to near of the borders and a medium one at the opposite border.                          |
| 21   | Yes     | 1               | -                  | One very large indication going from one border to near the opposite border.   |
| 22   | Yes     | 2               | 2                  | Three medium/large sized and a very large indication towards the middle of the repair, but some of them reach areas close to the borders or borders. |

Table 17: Ultrasound defect detections in pipes pre-ageing, for pipes to be conditioned in chamber 3.

| Pipe | Defects | At/near borders | Towards the middle | Observations  |
|------|---------|-----------------|--------------------|---|
| 6    | Yes     | 3               | 1                  | Three medium sized indications close together at one border. A medium/large sized indication detached towards the middle.   |
| 11   | Yes     | 4               | 1                  | A cluster of medium and large indications going from the middle of the repair towards one of the borders. A smaller cluster of medium indications near the opposite border. |
| 12   | Yes     | 3               | 1                  | One large indication in the middle and three medium sized indications near or at the borders.   |
| 13   | Yes     | 2               | -                  | Two very large indications at one of the borders. One goes parallel to the border while the other is perpendicular, going from the border towards the middle of the repair. |
| 18   | Yes     | 2               | 1                  | A very large indication going from one border towards the middle. Two medium sized indications, one near a border and one towards the middle                                |
| 23   | Yes     | 2               | 2                  | One small and one medium sized indications at opposing borders. Two small/medium indications in the middle.   |
| 24   | Yes     | 3               | 1                  | One cluster of small/medium indications at one border and a cluster of medium/large defects at the opposite border, but a little more towards the middle of the repair.     |
| 25   | Yes     | 2               | 0                  | One small indication at each border.  |

Continuous monitoring showed that most of the increase in detections happened from the beginning of testing up to T2, as seen in Table 18, Table 19 and Table 20. As observed in shearography, the sharp increase in detections at the beginning of ageing coincided with the period of highest water/moisture absorption rate in the absorption samples, highlighting a relationship between moisture and defect propagation.

After this interval, detections remained constant with few exceptions, such as pipes 6 and 8, which were conditioned in chambers 3 (70 °C) and 1 (35 °C) respectively, that showed a significant, albeit punctual, increase in detections in T4. Again, like shearography, most of the defect growth occurred before saturation was reached, further confirming the moisture/defect propagation relationship hypothesis.

During the last round of inspections, significant increases were also observed in pipes 12 and 14, which were conditioned in chambers 3 (70 °C) and 1 (35 °C) respectively. This may have been an indication of significant damage to the steel pipe/composite interface by water absorption, causing loss of adhesion and/or propagation effects of edge corrosion propagation, which at this ageing point was very

severe. Taking into account the results for UT in the reference pipe, where detection at the edges was more uncertain, this hypothesis needs to be further validated.

From the beginning of the tests until around T2/T3 (between 2,000 h and 3,000 h) the mass gain rate was very high, as observed in the absorption samples. This created a scenario where damage, especially at the edges of the repairs, could have happened more easily through water ingress or interface absorption, and, as such, 16 out of the 24 pipes had new defects appearing from T0 to T1. After T1, only samples 8 and 12 developed new defects at T4 and T9, respectively. After T2, only pipes 6, 8, 12 (new defect) and 14 had detected area growth greater than 10%, since the samples showed a less intense moisture absorption rate, as they were approaching saturation. During this period, the growth was mainly caused by small clusters of defects that coalesced.

Table 18: Ultrasound detection during periodic inspections in chamber 1.

| Pipes | Area Detected (mm <sup>2</sup> ) |                  |                 |                |                 |                |                |       |       |                |
|-------|----------------------------------|------------------|-----------------|----------------|-----------------|----------------|----------------|-------|-------|----------------|
|       | T0                               | T1               | T2              | T3             | T4              | T5             | T6             | T7    | T8    | T9             |
| 1     | 15470                            | 20964<br>(+36%)  | 24235<br>(+16%) | 25569<br>(+6%) | 25622           | 25622          | 25622          | 25622 | 25622 | 25622          |
| 2     | 14260                            | 31030<br>(+118%) | 38450<br>(+24%) | 38450          | 38450           | 38450          | 38450          | 38450 | 38450 | 38450          |
| 7     | 6371                             | 14833<br>(+133%) | 15932<br>(+7%)  | 15932          | 15932           | 15932          | 17374<br>(+9%) | 17374 | 17374 | 17374          |
| 8     | 16363                            | 16533<br>(+1%)   | 16789<br>(+2%)  | 16789          | 26145<br>(+56%) | 26145          | 26145          | 26145 | 26145 | 26145          |
| 14    | 1705                             | 2415<br>(+42%)   | 2485<br>(+3%)   | 2485           | 2485            | 2485           | 2485           | 2485  | 2485  | 2905<br>(+17%) |
| 15    | 13845                            | 18482<br>(+33%)  | 21814<br>(+18%) | 21814          | 21814           | 22684<br>(+4%) | 22684          | 22684 | 22684 | 22684          |
| 19    | 8160                             | 13211<br>(+62%)  | (+2%)           | 13480          | 13480           | 13480          | 13480          | 13480 | 13480 | 13647<br>(+1%) |
| 20    | 21977                            | 28270<br>(+29%)  | 31398<br>(+11%) | 31398          | 31398           | 31398          | 31398          | 31398 | 31398 | 31398          |

Table 19: Ultrasound detection during periodic inspections in chamber 2.

| Pipes | Area Detected (mm <sup>2</sup> ) |                  |                 |                |       |                |       |       |       |       |
|-------|----------------------------------|------------------|-----------------|----------------|-------|----------------|-------|-------|-------|-------|
|       | T0                               | T1               | T2              | T3             | T4    | T5             | T6    | T7    | T8    | T9    |
| 3     | 4280                             | 24850<br>(+481%) | 27198<br>(+9%)  | 27367<br>(+1%) | 27367 | 27367          | 27367 | 27367 | 27367 | 27367 |
| 5     | 9429                             | 9486<br>(+1%)    | 10109<br>(+7%)  | 10109          | 10109 | 10109          | 10109 | 10109 | 10109 | 10109 |
| 9     | 4306                             | 12840<br>(+198%) | 19932<br>(+55%) | 19932          | 19932 | 19932          | 19932 | 19932 | 19932 | 19932 |
| 10    | 4996                             | 18472<br>(+270%) | 20448<br>(+11%) | 20448          | 20448 | 20448          | 20448 | 20448 | 20448 | 20448 |
| 16    | 1066                             | 1477<br>(+39%)   | 2320<br>(+57%)  | 2494<br>(+8%)  | 2494  | 2494           | 2494  | 2494  | 2494  | 2494  |
| 17    | 15694                            | 18744<br>(+19%)  | 21604<br>(+15%) | 21604          | 21604 | 21931<br>(+2%) | 21931 | 21931 | 21931 | 21931 |
| 21    | 13230                            | 28422<br>(+115%) | 30370<br>(+7%)  | 30370          | 30370 | 30370          | 30370 | 30370 | 30370 | 30370 |
| 22    | 22347                            | 26233<br>(+17%)  | 32876<br>(+25%) | 33349<br>(+1%) | 33349 | 33349          | 33349 | 33349 | 33349 | 33349 |

Table 20: Ultrasound detection during periodic inspections in chamber 3.

| Pipes | Area Detected (mm <sup>2</sup> ) |                  |                  |                  |                  |       |       |       |       |                 |
|-------|----------------------------------|------------------|------------------|------------------|------------------|-------|-------|-------|-------|-----------------|
|       | T0                               | T1               | T2               | T3               | T4               | T5    | T6    | T7    | T8    | T9              |
| 6     | 5535                             | 12436<br>(+125%) | 15178<br>(+22%)  | 15178            | 37430<br>(+147%) | 37430 | 37430 | 37430 | 37430 | 38159<br>(+2%)  |
| 11    | 12551                            | 23724<br>(+89%)  | 23751<br>(+0,1%) | 23856<br>(+0,4%) | 23856            | 23856 | 23856 | 23856 | 23856 | 23856           |
| 12    | 5807                             | 6465<br>(+11%)   | 9787<br>(+51%)   | 9787             | 9787             | 9787  | 9787  | 9787  | 9787  | 11698<br>(+20%) |
| 13    | 28656                            | 30380<br>(+6%)   | 30934<br>(+2%)   | 30934            | 30934            | 30934 | 30934 | 30934 | 30934 | 30294<br>(-2%)  |
| 18    | 14716                            | 17724<br>(+20%)  | 18696<br>(+5%)   | 18948<br>(+1%)   | 19008            | 19008 | 19008 | 19008 | 19008 | 19008           |
| 23    | 5043                             | 8161<br>(+62%)   | 8891<br>(+9%)    | 8948<br>(+1%)    | 8948             | 8948  | 8948  | 8948  | 8948  | 8948            |
| 24    | 7466                             | 7782<br>(+4%)    | 8960<br>(+15%)   | 9001             | 9001             | 9001  | 9001  | 9001  | 9001  | 9001            |
| 25    | 1521                             | 6305<br>(+315%)  | 6581<br>(+4%)    | 6581             | 6581             | 6581  | 6581  | 6581  | 6581  | 6581            |

### 4.1.3. Comparison

When compared, shearography and ultrasound differed significantly in relation to the detected damaged area. For as-manufactured samples, shearography detected far fewer flaws than ultrasound. Shearography found 10 pipes with indications, only 1 of which had indications larger than 10% of defective area. Ultrasound found that all 24 pipes had some type of indication, with 11 having more than 10% defective area detected. On average, for UT, the defective areas represented 9.83 % of the surface area of the samples, with pipe 13 showing more than 25 % of damaged area. This is a stark contrast when compared to shearography, where average defective area was 0.76 % and the pipe with the largest defective area detected was #6 with 14.26% at T0. The sample with the largest area detected for UT, #13, did not show indications during SH inspection and the sample with the largest area detected for SH, pipe #6, had 5% of its area initially considered defective by UT.

After ageing, the average damaged area increased to 18.97% for UT and 4.31% for SH, while pipes #2 and #6, from chambers 1 (35 °C) and 3 (70 °C), respectively, had the largest area detected with about 35% each for UT and pipe #6 remained the most defective sample for SH, with 72.64% of damaged area. A comparison of detections for both T0 and T9 is shown in Figure 37. Compared to SH, UT appeared to overestimate the area, and the number of defects present in the samples both before and during ageing.

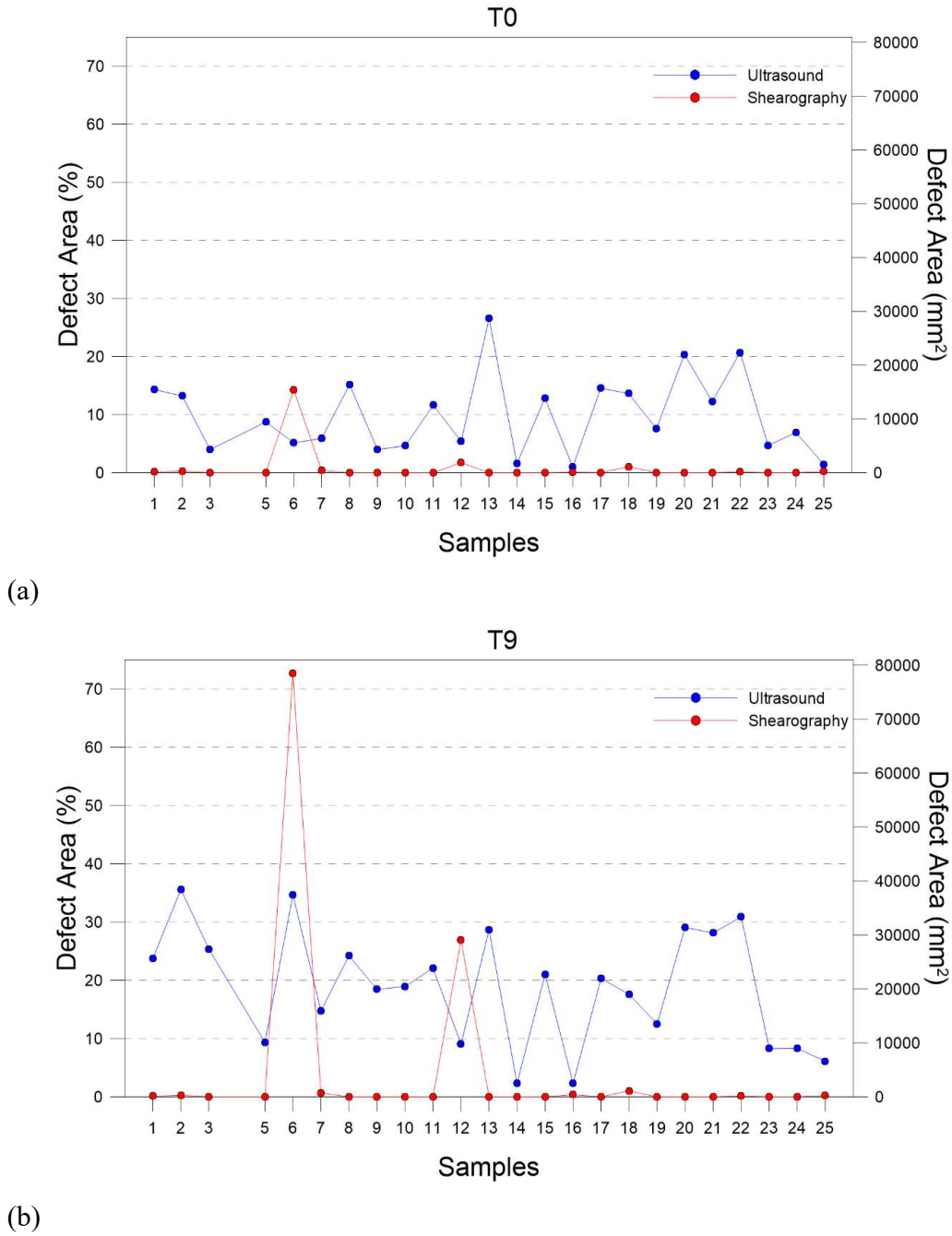
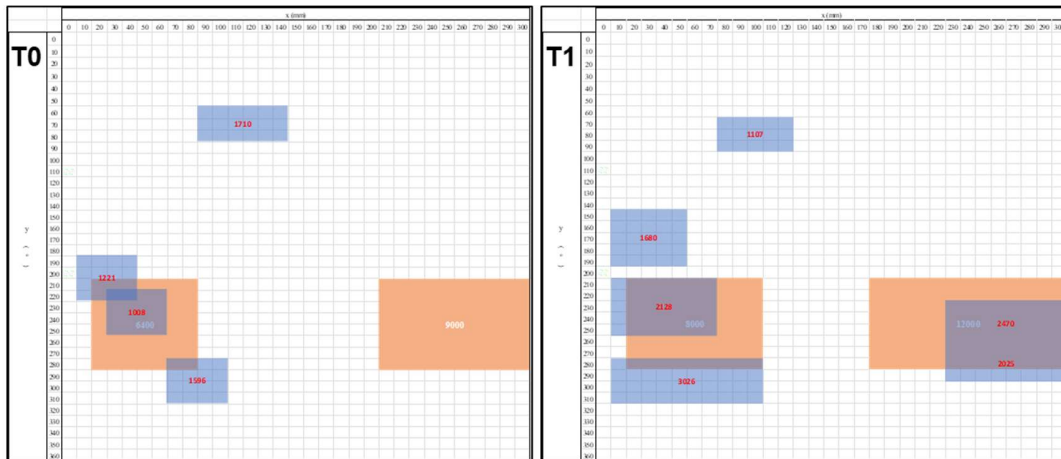


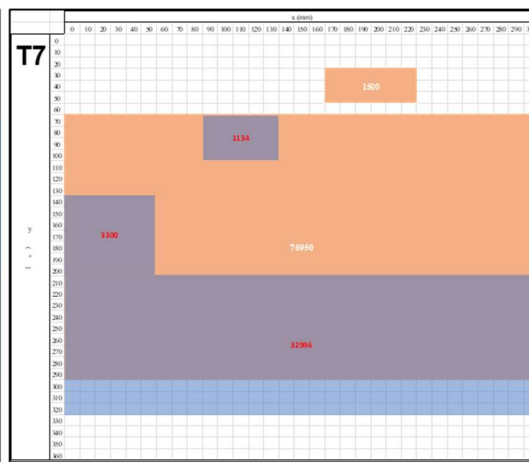
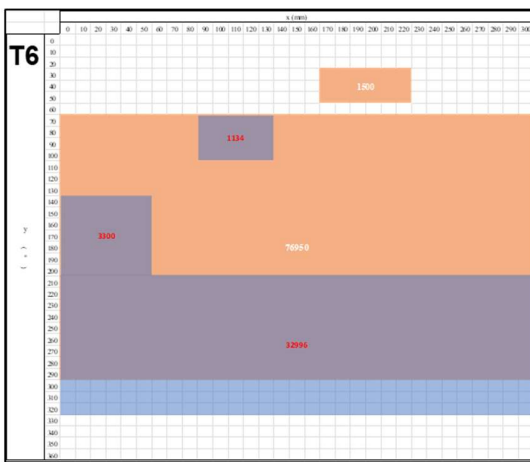
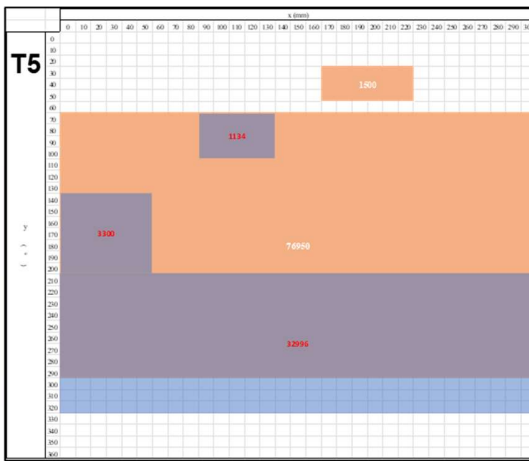
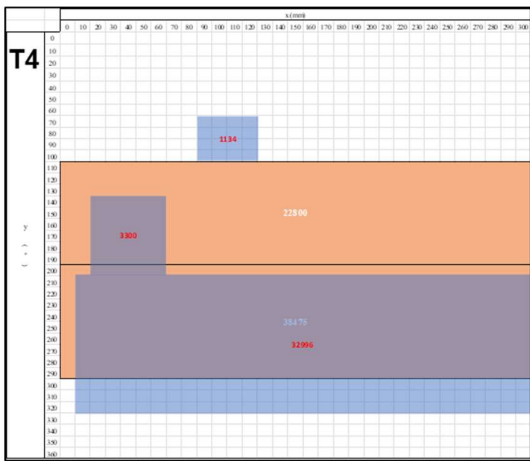
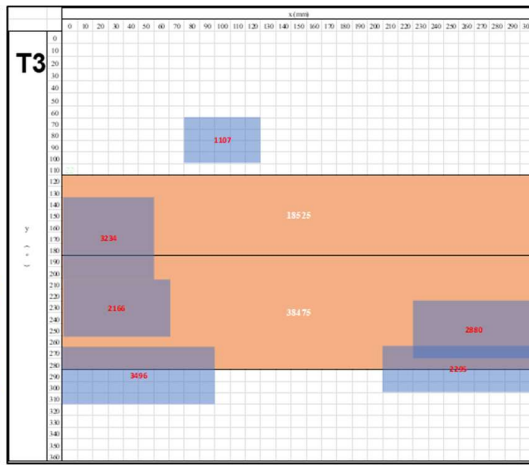
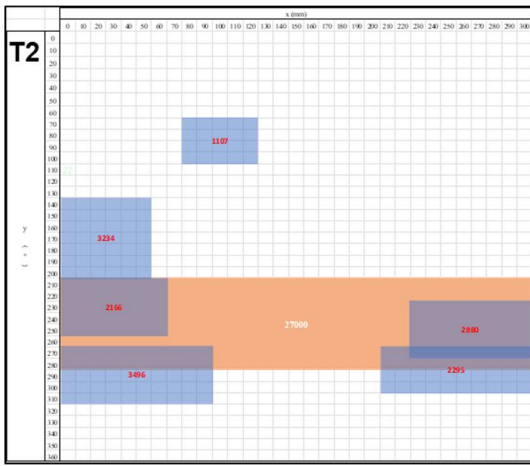
Figure 37: Comparison between UT and SH detections at a) T0; b) T9.

Figure 38 shows the detections for both techniques in sample #6. Larger images are also available at the Appendix A for better visualization. On this pipe, especially, both techniques detected similar defective areas as inspections were performed over time. In both cases, the initial detections were concentrated on the edges of the repair

at T0 and T1. At T2 shearography had already detected the defects from both edges coalescing, while UT would only observe this phenomenon at T4. Around T5 both techniques had already reached a point where the detections became stable, as previously discussed, once samples got closer to saturation. UT and SH detections were concentrated in the same two thirds of the pipe area, with the region around 0° practically free of detections. In the areas where the techniques found defects, SH indicated a much larger area as being defective.

One hypothesis that might explain this difference is that the criterion used by UT is focused only on the interface region between the steel pipe and the composite repair. Because of the gate applied for analysis, only defects in this region would have been detected, while defects that might have been present throughout the thickness of the composite repair would not have been detected. This is not the case with SH, where any defects that could be somewhere just below the surface of the repair and the steel pipe would overlap and appear to the operator as one single defective area. In the case of pipe #6, as it appeared to be a very defective sample, defects could be in the entire thickness of the material and not restricted to the interface, so SH presented a much larger indication.





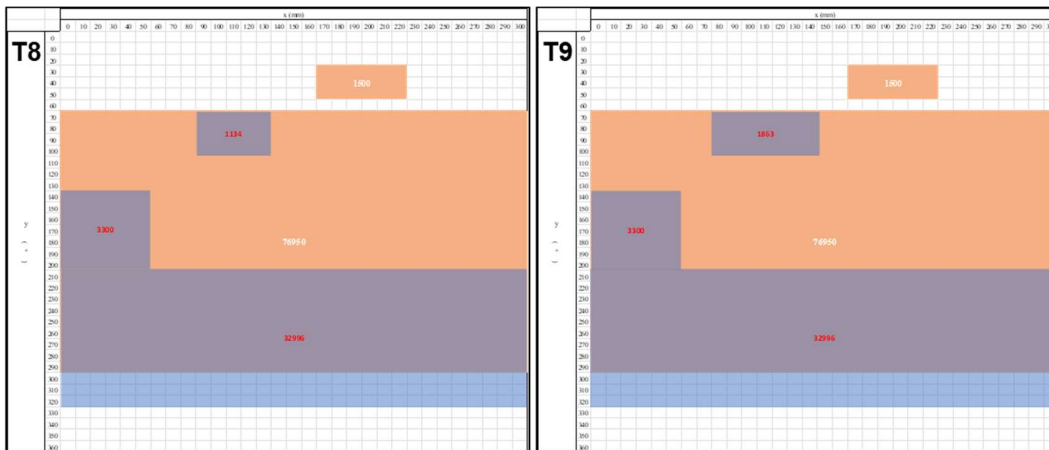


Figure 38: Evolution of detections for pipe number 6 as seen by Shearography, in orange, and Ultrasound, in blue. Numbers inside indications represent the defective area in mm<sup>2</sup>.

In general, SH seemed to be more reliable than UT, although definitive results are only possible after a destructive test of the samples (“dissection”). SH performed significantly better than UT in the reference pipe qualification, especially in the edges of the repair, where most defect indications were concentrated and which had the smallest sizes. Also, in some instances, UT detections shrank or vanished and, although this did not significantly affect overall results of the technique, it is an indication that performance is not as repeatable as SH.

From a deployment perspective, SH showed immediate application with a much consolidated methodology and field equipment. The technique also is more versatile, allowing for inspection of carbon-fiber reinforced repairs as well, which were not tested in this work but is important as there are many repairs of this type in the field. Ultrasound showed similar productivity and has a much larger support network than Shearography, as it is a more widespread NDT. The main limitations for field applications showed by UT were the methodology for the specific case of GFRP inspection and the necessity of a coupling media, which can limit certain field inspections. Also, surface preparation is not a limiting factor for either technique.

Table 21: NDT quantitative analysis.

| Quantitative Analysis                            | Technique  |  |
|--|--|--|
|  | Shearography   | Ultrasound   |
| Inspection time per sample (incl. surface prep.) | Aprox. 40 min  | Aprox. 50 min  |
| Couplant   | No   | Yes  |
| Fiber-glass reinforcements                       | Yes  | Yes  |
| Carbon-fiber reinforcements                      | Yes  | No   |
| Surface preparation                              | Powder spray if surface is glossy                    | Clean possible couplant contaminants on the surface                          |
| Main advantages                                  | Already used for field inspections with good results | Consolidated network of service providers and equipment manufacturers        |
| Main limitations                                 | Scarce service providers and equipment manufacturers | Methodology needs development for reliable application, material limitations |

#### 4.2. Life in service prediction

A methodology was proposed to predict the growth of the damaged area, based on the experimental data provided by the NDT inspections. The Phani-Bose model was used to establish long-term property retention, which, in this case, was the undamaged area, as a function of operating temperature and time.

The first step was to subtract the defective areas detected by each technique and then average the values obtained for all samples in a given chamber. Then, the maximum retention of 100% was set as the average of the undamaged areas in all samples from each chamber at T0, according to Table 22 and Table 23, for UT and SH respectively.

Table 22: Average remaining area and property retention over time for UT inspected samples.

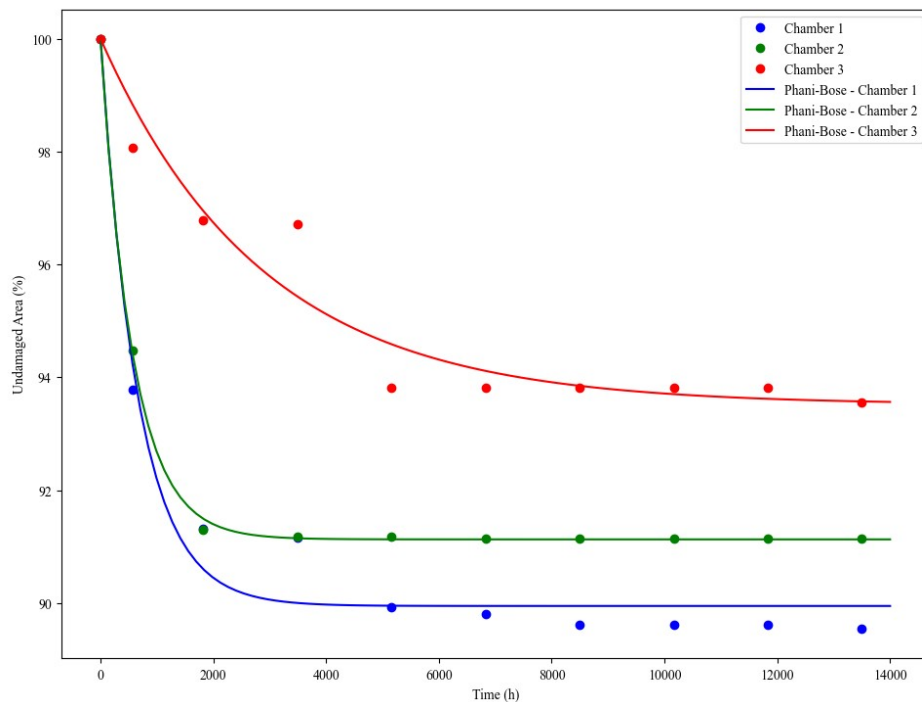
| UT<br>Time (h) | Chamber 1                                 |                             |               | Chamber 2                                 |                             |               | Chamber 3                                 |                             |               |
|----------------|---|-----------------------------|---------------|---|-----------------------------|---------------|---|-----------------------------|---------------|
|                | Average Remaining Area (mm <sup>2</sup> ) | Std. Dev (mm <sup>2</sup> ) | Retention (%) | Average Remaining Area (mm <sup>2</sup> ) | Std. Dev (mm <sup>2</sup> ) | Retention (%) | Average Remaining Area (mm <sup>2</sup> ) | Std. Dev (mm <sup>2</sup> ) | Retention (%) |
| 0              | 88.64                                     | 5.58                        | 100.00        | 91.28                                     | 6.24                        | 100.00        | 90.59                                     | 7.44                        | 100.00        |
| 570            | 83.13                                     | 7.76                        | 93.79         | 83.74                                     | 7.98                        | 94.47         | 86.92                                     | 7.80                        | 98.06         |
| 1820           | 80.95                                     | 9.63                        | 91.33         | 80.92                                     | 8.88                        | 91.29         | 85.79                                     | 7.43                        | 96.78         |
| 3490           | 80.80                                     | 9.69                        | 91.15         | 80.82                                     | 8.92                        | 91.18         | 85.74                                     | 7.45                        | 96.72         |
| 5160           | 79.71                                     | 9.71                        | 89.92         | 80.82                                     | 8.92                        | 91.18         | 83.15                                     | 10.04                       | 93.81         |
| 6830           | 79.61                                     | 9.71                        | 89.81         | 80.79                                     | 8.93                        | 91.14         | 83.15                                     | 10.04                       | 93.81         |
| 8500           | 79.44                                     | 9.62                        | 89.62         | 80.79                                     | 8.93                        | 91.14         | 83.15                                     | 10.04                       | 93.81         |
| 10170          | 79.44                                     | 9.62                        | 89.62         | 80.79                                     | 8.93                        | 91.14         | 83.15                                     | 10.04                       | 93.81         |
| 11840          | 79.44                                     | 9.62                        | 89.62         | 80.79                                     | 8.93                        | 91.14         | 83.15                                     | 10.04                       | 93.81         |
| 13500          | 79.37                                     | 9.51                        | 89.54         | 80.79                                     | 8.93                        | 91.14         | 82.92                                     | 9.95                        | 93.55         |

Table 23: Average remaining area and property retention over time for SH inspected samples.

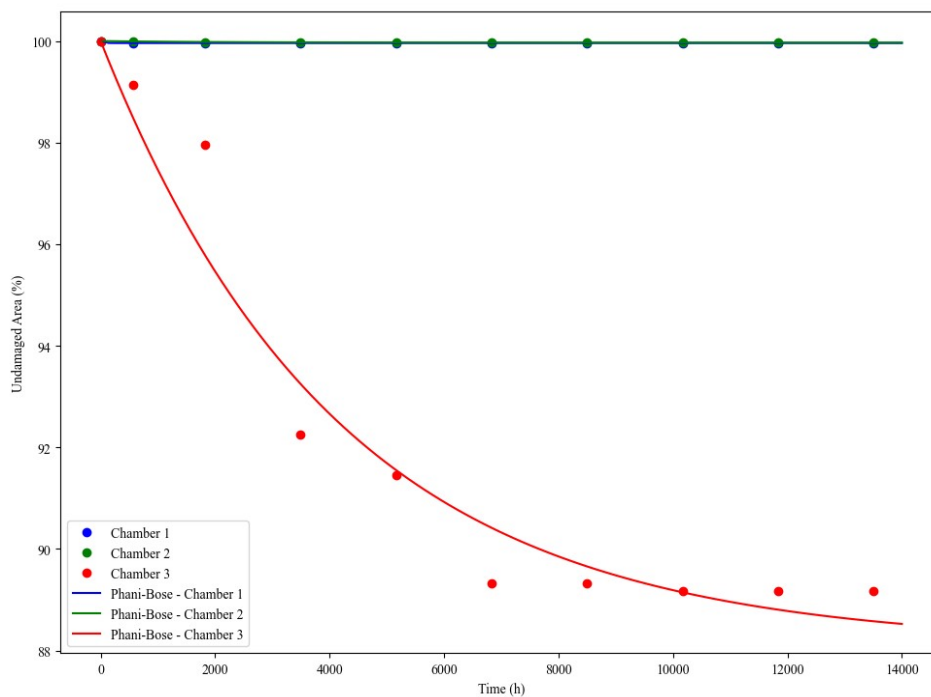
| SH<br>Time (h) | Chamber 1                                 |                             |               | Chamber 2                                 |                             |               | Chamber 3                                 |                             |               |
|----------------|---|-----------------------------|---------------|---|-----------------------------|---------------|---|-----------------------------|---------------|
|                | Average Remaining Area (mm <sup>2</sup> ) | Std. Dev (mm <sup>2</sup> ) | Retention (%) | Average Remaining Area (mm <sup>2</sup> ) | Std. Dev (mm <sup>2</sup> ) | Retention (%) | Average Remaining Area (mm <sup>2</sup> ) | Std. Dev (mm <sup>2</sup> ) | Retention (%) |
| 0              | 99.90                                     | 0.14                        | 100.00        | 99.97                                     | 0.05                        | 100.00        | 97.85                                     | 4.61                        | 100.00        |
| 570            | 99.86                                     | 31.38                       | 99.96         | 99.97                                     | 31.41                       | 100.00        | 96.99                                     | 34.20                       | 99.13         |
| 1820           | 99.86                                     | 0.23                        | 99.96         | 99.95                                     | 0.10                        | 99.98         | 95.85                                     | 8.19                        | 97.96         |
| 3490           | 99.86                                     | 0.23                        | 99.96         | 99.93                                     | 0.12                        | 99.97         | 90.26                                     | 18.02                       | 92.25         |
| 5160           | 99.86                                     | 0.23                        | 99.96         | 99.93                                     | 0.12                        | 99.97         | 89.49                                     | 19.42                       | 91.46         |
| 6830           | 99.86                                     | 0.23                        | 99.96         | 99.93                                     | 0.12                        | 99.97         | 87.40                                     | 24.32                       | 89.32         |
| 8500           | 99.86                                     | 0.23                        | 99.96         | 99.93                                     | 0.12                        | 99.97         | 87.40                                     | 24.32                       | 89.32         |
| 10170          | 99.86                                     | 0.23                        | 99.96         | 99.93                                     | 0.12                        | 99.97         | 87.26                                     | 24.40                       | 89.18         |
| 11840          | 99.86                                     | 0.23                        | 99.96         | 99.93                                     | 0.12                        | 99.97         | 87.26                                     | 24.40                       | 89.18         |
| 13500          | 99.86                                     | 0.23                        | 99.96         | 99.93                                     | 0.12                        | 99.97         | 87.26                                     | 24.40                       | 89.18         |

The Phani-Bose equation (Eq. 6) was used to fit the curves to the retention values as a function of time for both techniques (Figure 39) and the values for  $S_{\infty}$  and  $\tau$ , as well as the  $R^2$  for the fitted curves are given in Table 24.

The parameters  $S_{\infty}$  and  $\tau$  represent the average undamaged area at infinity and the time required for this retention to be reached at a given temperature, respectively. The fit was very good, with  $R^2 > 0.9$  for all datasets indicating that the Phani-Bose model accurately describes the behavior exhibited during testing.



(a)



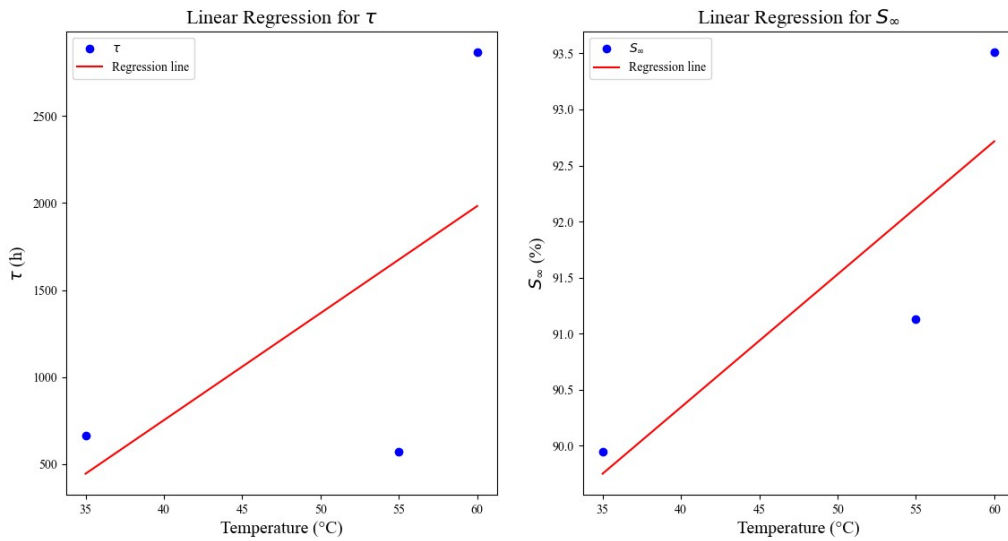
(b)

Figure 39: Experimental data and fitted curves for property retentions as a function of time in: a) UT inspection; b) SH inspection. The points for chambers 1 and 2 are almost completely overlapped, due to the similarity of the undamaged area retention values for both.

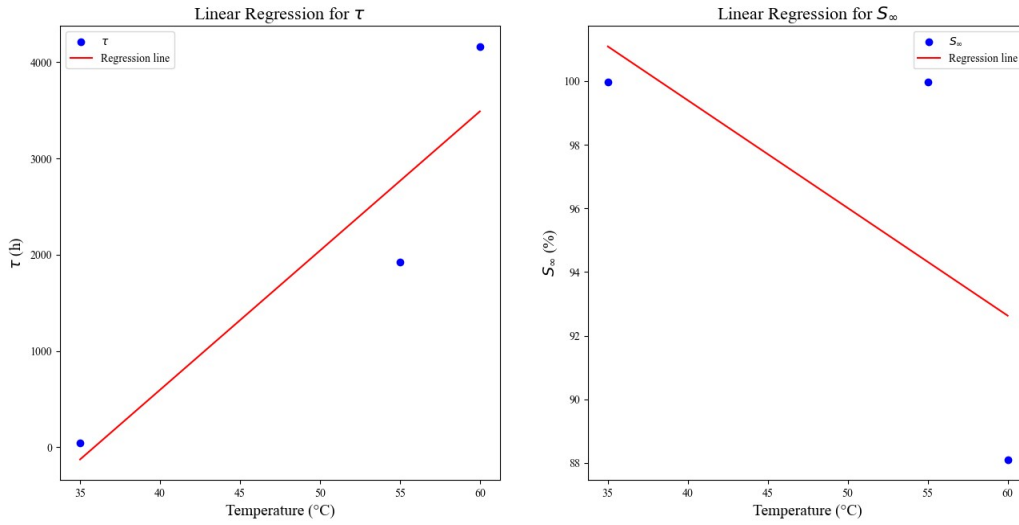
Table 24: Phani-Bose model parameters for Shearography and Ultrasound inspected samples.

| Parameters       | Shearography |           |           | Ultrasound |           |           |
|------------------|--------------|-----------|-----------|------------|-----------|-----------|
|                  | Chamber 1    | Chamber 2 | Chamber 3 | Chamber 1  | Chamber 2 | Chamber 3 |
| $S_{\infty}$ (%) | 99.96        | 99.97     | 88.11     | 89.95      | 91.13     | 93.51     |
| $\tau$ (h)       | 41.8         | 1922.77   | 4162.49   | 666.1      | 571.26    | 2866.35   |
| $R^2$            | 1            | 0.94      | 0.957     | 0.974      | 0.999     | 0.937     |

After that, both  $S_{\infty}$  and  $\tau$  were plotted as a function of temperature, Figure 40. A Python script was used to apply a linear regression method for each dataset. The parameters were listed in Table 25. With the parameters determined, the equations of the fitted curves for  $S_{\infty}$  and  $\tau$  describe how each of the variable behaves with changes in temperature, thus allowing the estimation of the effective long-term repaired area given a certain period of time and operating temperature.



(a)



(b)

Figure 40:  $S_{\infty}$  and  $\tau$  plots based on data from: a) UT inspection; b) SH inspection

Table 25: Linear regression parameters and  $R^2$  for  $S_{\infty}$  and  $\tau$  in each NDT.

| y=ax+b | Shearography |          | Ultrasound   |          |
|--------|--------------|----------|--------------|----------|
|        | $S_{\infty}$ | $\tau$   | $S_{\infty}$ | $\tau$   |
| a      | -0.34        | 144.61   | 0.12         | 61.51    |
| b      | 112.93       | -5187.89 | 85.60        | -1707.57 |
| $R^2$  | 0.428        | 0.859    | 0.748        | 0.392    |

Although the fit was good for some of the parameters, the information provided by the  $S_{\infty}$  and  $\tau$  plots did not reflect the expected behavior in real life. The variable  $S_{\infty}$  is expected to decrease as temperature increases, because high operating temperatures tend to accelerate degradation mechanisms and lower the property retention over time. This unexpected behavior was mainly caused due to insufficient data for each ageing condition, as only 8 pipes were analyzed from each chamber and, of these, few showed significant damage growth during the testing period. Additionally, in the case of UT, chambers 1 and 2, despite having less severe conditions than chamber 3, had a greater average damaged area at T0, which greatly affects damage propagation and may have distorted the results.

In a parallel research within the author’s research group (not yet published), the same methodology was used to estimate the retention of properties in other types of samples with success. Double-Lap Shear (DLS) and composite samples were aged under the same conditions, but with a much larger sample pool. With the results, a tool was developed (Figure 41) to help predict long-term retention of properties as a function of either temperature and time or temperature and target retention, in which case the time necessary to reach the target is calculated.

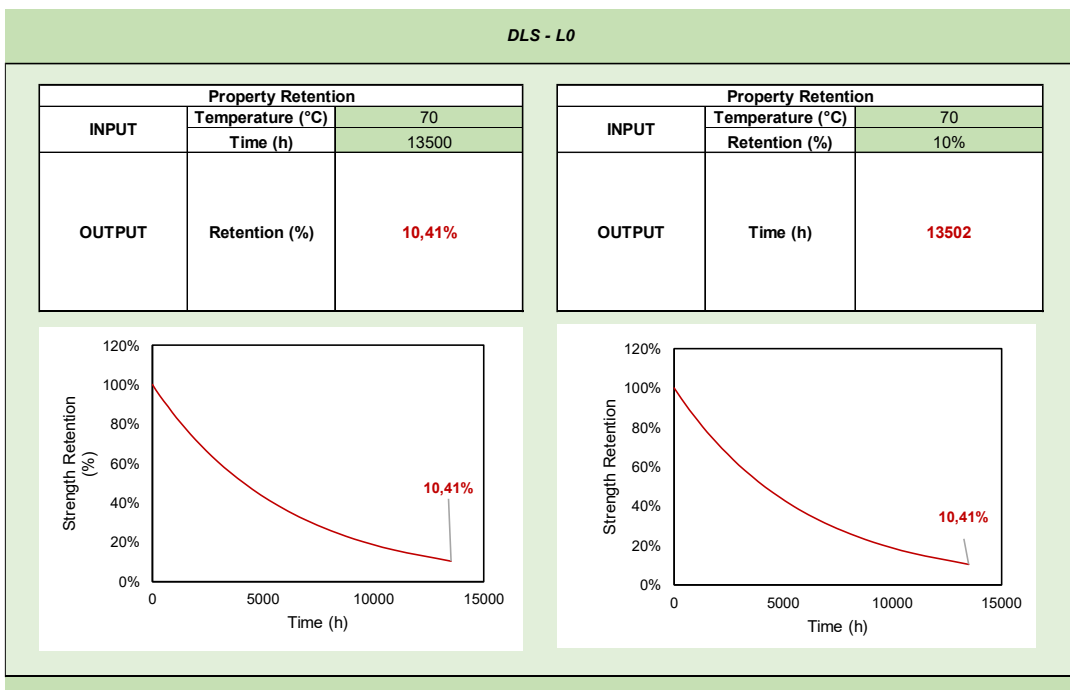


Figure 41: Property retention tool for DLS samples calculating both retention as a function of temperature and time and time to reach a certain retention as a function of temperature.

The same approach was tested with NDT results on pipe samples with some degree of success, but more data needs to be input into the model for the results to be reliable enough for use in the field. A screenshot of the tool can be seen in Figure 42.

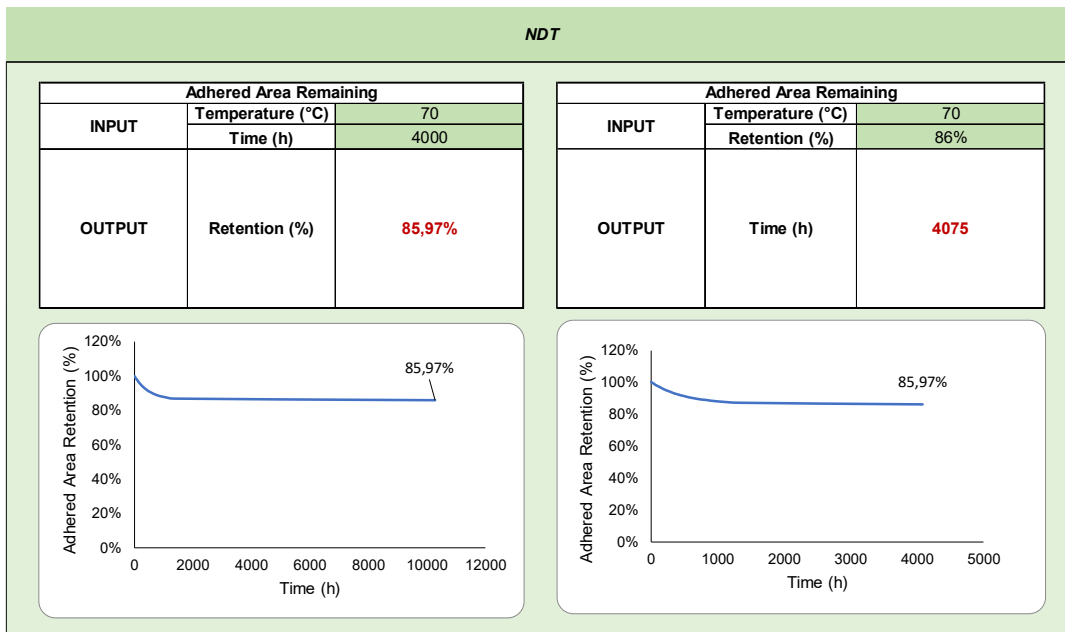


Figure 42: Initial attempts at developing a property retention tool for effective repair length, based on the Phani-Bose methodology.

Although it shows great potential, there are noteworthy limitations to this method. Firstly, it assumes that the undamaged area of the pipes will stabilize and stay at a retention plateau indefinitely. Since corrosion propagation throughout the edges of the repair does not necessarily stop, it would be incorrect to expect undamaged area to always stop decreasing indefinitely. With that said, during this experiment, the behavior displayed by the samples did show signs of stabilization in the timeframe analyzed. Also, the model does not take into account every degradation mechanism independently, such as interface degradation, water absorption by the composite, hydrolysis of the polymeric matrix and corrosion propagation.

## 5. Conclusions

In this work, shearography and ultrasound inspections were used to identify and monitor defects in samples of repaired pipeline. The repaired pipes were aged and the techniques were employed to periodically identify growth and initiation of defects. Also, the results of each technique were correlated with moisture absorption data provided by samples that were aged in parallel with the pipe samples. Additionally, the first step towards developing a methodology for life-in-service predictions for effective repair areas was presented. Below are the main conclusions:

- Both techniques were able to detect artificial Teflon defects with some capacity. Shearography was able to detect a greater percentage of the total, including smaller ones at the edges of the repaired area that ultrasound was not able to;
- Both techniques were able to identify possible defects present in the samples as fabricated. Shearography identified far fewer samples with indications than ultrasound, which found indications of defects in all as fabricated samples. This result indicates that ultrasound might have overestimated defect detection;
- Both techniques were able to monitor growth and initiation of defects periodically during ageing. Shearography indications were more repeatable, showing consistent defect positioning and size, whereas ultrasound showed, in some instances, defect indications diminishing or vanishing, but that did not affect the overall analysis;
- In general, shearography has proven to be a more ready-to-use technique. Ultrasound showed good results with the methodology used, but there is room for development in order to explore the full potential of the technique;
- The main factor for damage propagation seemed to be the presence of defects before ageing. Indications of new defects occurred less than expected during ageing, with most of the increase of damaged area being the growth of indications present at the first inspection, mainly in the case of Shearography. Ultrasound did show more new defect indications than shearography but still less than expected;

- Defect growth and initiation occurred preferentially in regions close to or on the edges of the repaired area, which could be caused by more accentuated moisture absorption in that area;
- Defect growth showed a possible correlation with moisture absorption, with the most detections happening at periods of increased absorption by the composite and possibly across the steel pipe/composite interface;
- The methodology used for life-in-service prediction showed good potential to provide valuable information for integrity management of pipeline repairs, but needs to be further developed, especially through the evaluation of more samples.

## 6. Proposals for Future Developments

The methodology used for ultrasound inspections can still be developed to maximize the potential of the technique. The investigation of different gating procedures, focusing on different reflections from the repaired pipe sample could yield interesting results. Different criteria besides phase inversion could also be explored, as well as the application of the phase inversion criterion could be further developed for a better performance in this specific type of sample, which is not usual for UT. Additionally, the use of phased arrays could also greatly benefit the inspection, providing more accurate data in this difficult scenario for the technique.

For service life predictions, more samples should be inspected and their data input into the model to make it more accurate. This tool, when fully developed, can significantly assist the integrity management strategies of operators of repaired pipeline for safer operation and possibility of revalidation of repairs already in service. The model also can be used in conjunction with the ISO 24817 at the design stage as a way to take into consideration the expected degradation of the repair over the expected lifetime of operation. Both repair length and thickness can be optimized using the proposed methodology.

The data collected during NDT inspections during this work could also be used to establish an adjust parameter for a more accurate service life prediction based on DLS and composite samples, as mentioned previously. Results from accelerated ageing in DLS type samples represent a very conservative scenario due to the characteristics of the samples, while the plateau behavior found in composite property retention plots does not accurately reflect the degradation process that the repair undergoes in the field. By combining these information with the damage growth data provided by the NDTs, one could compare growth rates and achieve a result that is at the same time less conservative and closer to reality in a unified model, providing a basis for extending the service life of a repair in the field.

An evaluation of the samples by computerized tomography and/or destructive sectioning of the repairs to verify the defect detections by NDTs would also be very important to establish the accuracy of the techniques. The information provided by this

test can help to more accurately assess the limitations and strengths of each technique and also help develop more efficient methodologies regarding damage propagation and steel pipe/composite adhesion.

## 7. References

- [1] J.A. Beavers, N.G. Thompson, External Corrosion of Oil and Natural Gas Pipelines, in: Corrosion: Environments and Industries, ASM International, 2006: pp. 1015–1025. <https://doi.org/10.31399/asm.hb.v13c.a0004213>.
- [2] V.A. Perrut, Estudo do comportamento estático e à fadiga de junta colada compósito polimérico e aço em diferentes tratamentos de superfície e sujeitos à névoa salina aplicada como reparo na indústria do petróleo, PhD, COPPE/UFRJ, 2018.
- [3] W. Ma, J. Luo, K. Cai, Discussion about application of composite repair technique in pipeline engineering, in: Adv Mat Res, 2011: pp. 185–188. <https://doi.org/10.4028/www.scientific.net/AMR.311-313.185>.
- [4] L.C. Hollaway, J. Cadei, Progress in the technique of upgrading metallic structures with advanced polymer composites, Progress in Structural Engineering and Materials. 4 (2002) 131–148. <https://doi.org/10.1002/pse.112>.
- [5] K.S. Lim, S.N.A. Azraai, N.M. Noor, N. Yahaya, An Overview of Corroded Pipe Repair Techniques Using Composite Materials, International Journal of Materials and Metallurgical Engineering. 10 (2016) 19–25. [scholar.waset.org/1307-6892/10003226](http://scholar.waset.org/1307-6892/10003226) (accessed January 25, 2023).
- [6] L. Cercone, J.D. Lockwood, Review of FRP Composite Materials for Pipeline Repair, in: Pipelines, ASCE, Houston, TX, 2005: pp. 1001–1013. <https://doi.org/https://doi.org/10.1061/9780784408001>.
- [7] W.D. Callister, Materials Science and Engineering: An Introduction, 7th ed., John Wiley & Sons, Inc., 2007.
- [8] R.F. Gibson, Principles of Composite Material Mechanics, Fourth, CRC Press, Boca Raton, FL, 1994. <https://doi.org/10.2214/ajr.159.6.1442392>.
- [9] ASTM, Standard Practice for Operating Salt Spray (Fog) Apparatus, ASTM International, 2019. <https://doi.org/10.1520/B0117-19>.

- [10] Prokem, <https://www.prokem.org/offshore/>, (2023). <https://www.prokem.org/offshore/> (accessed April 13, 2023).
- [11] S.D. Soares, A.L. Fampa, A. Albertazzi, A. V. Fantin, D.P. Willemann, M.E. Benedet, F.A. Silva, Shearography Inspection to Assess the Structural Integrity of Composite Repairs in Metallic Piping, in: Offshore Technology Conference, OTC, 2018. <https://doi.org/10.4043/28825-MS>.
- [12] W.M. Alobaidi, E.A. Alkuam, H.M. Al-Rizzo, E. Sandgren, Applications of Ultrasonic Techniques in Oil and Gas Pipeline Industries: A Review, *American Journal of Operations Research*. 05 (2015) 274–287. <https://doi.org/10.4236/ajor.2015.54021>.
- [13] M.E. Benedet, A.V. Fantin, D.P. Willemann, A.A. Gonçalves Júnior, C.R. Schmitz, A.L.F.S. d’Almeida, S.D. Soares, L.D.M. Lana, V.A. Perrut, The use of Shearography technique to evaluate polymeric composite repairs - case study, *Matéria (Rio de Janeiro)*. 22 (2017). <https://doi.org/10.1590/s1517-707620170002.0241>.
- [14] M.E. Benedet, D.P. Willemann, A. V Fantin, C.R. Schmitz, F.Z. Broetto, A. Albertazzi, G. Jr, F. Dias, F. Martins, A. Lúcia, F.S. D’Almeida, Detecção de defeitos em revestimentos compósitos de tubulações metálicas - desafios da inspeção, in: CONAENDI & IEV, 2020.
- [15] F.J. Macedo, M.E. Benedet, A.V. Fantin, D.P. Willemann, F.A.A. da Silva, A. Albertazzi, Inspection of defects of composite materials in inner cylindrical surfaces using endoscopic shearography, *Opt Lasers Eng*. 104 (2018) 100–108. <https://doi.org/10.1016/j.optlaseng.2017.06.005>.
- [16] T. Hasiotis, E. Badogiannis, N.G. Tsouvalis, Application of ultrasonic C-scan techniques for tracing defects in laminated composite materials, *Strojnicki Vestnik/Journal of Mechanical Engineering*. 57 (2011) 192–203. <https://doi.org/10.5545/sv-jme.2010.170>.
- [17] G. Wróbel, S. Pawlak, A comparison study of the pulse-echo and through-transmission ultrasonics in glass/epoxy composites, *Journal of Achievements in Materials and Manufacturing Engineering*. 22 (2007) 51–54.

- [18] H. Trétout, D. David, F. Thevenot, Review of Advanced NDT Methods for Composite Aerospace Structures, in: Proceedings of the Int. Symp. on Advanced Materials for Lightweight Structures, Noordwijk, 1994: pp. 629–634. <https://www.researchgate.net/publication/275271264>.
- [19] Iowa State University Center for Nondestructive Evaluation (CNDE), Ultrasonic Testing, (2021). <https://www.nde-ed.org/NDETechniques/Ultrasonics/index.xhtml> (accessed March 22, 2023).
- [20] F. Aparecido Alves da, A. Alves da Silva, A. Albertazzi Gonçalves Júnior, D. Pedro Willemann, Colar de múltiplos sensores de shearografia para inspeção de reparos e uniões de materiais compósitos, Mestrado, Universidade Federal de Santa Catarina (UFSC), 2016.
- [21] T. Nelligan, D. Kass, Ultrasonic Testing of Fiberglass and Carbon Fiber Composites, (2011). <https://www.qualitymag.com/articles/92050-ultrasonic-testing-of-fiberglass-and-carbon-fiber-composites> (accessed April 13, 2023).
- [22] G. Wu, Z.-Q. Dong, X. Wang, Y. Zhu, Z.-S. Wu, Prediction of Long-Term Performance and Durability of BFRP Bars under the Combined Effect of Sustained Load and Corrosive Solutions, *Journal of Composites for Construction*. 19 (2015). [https://doi.org/10.1061/\(asce\)cc.1943-5614.0000517](https://doi.org/10.1061/(asce)cc.1943-5614.0000517).
- [23] J.F. Davalos, Y. Chen, I. Ray, Long-term durability prediction models for GFRP bars in concrete environment, *J Compos Mater*. 46 (2012) 1899–1914. <https://doi.org/10.1177/0021998311427777>.
- [24] K.K. Phani, N.R. Bose, Temperature Dependence of Hydrothermal Ageing of CSM-Laminate During Water Immersion, *Compos Sci Technol*. 29 (1987) 79–87.
- [25] K.K. Phani, N.R. Bose, Hydrothermal ageing of CSM-laminate during water immersion-an acousto-ultrasonic study, *J Mater Sci*. 21 (1986) 3633–3637.

- [26] MarketsandMarkets, Composites Market by Fiber Type (Glass Fiber Composites, Carbon Fiber Composites, Natural Fiber Composites), Resin Type (Thermoset Composites, Thermoplastic Composites), Manufacturing Process, End-use Industry and Region - Global Forecast to 2027, 2022. <https://www.marketsandmarkets.com/Market-Reports/composite-market-200051282.html> (accessed February 20, 2023).
- [27] S. Sajan, D. Philip Selvaraj, A review on polymer matrix composite materials and their applications, in: *Mater Today Proc*, Elsevier Ltd, 2021: pp. 5493–5498. <https://doi.org/10.1016/j.matpr.2021.08.034>.
- [28] T.A. Sebaey, Design of oil and gas composite pipes for energy production, in: *Energy Procedia*, Elsevier Ltd, 2019: pp. 146–155. <https://doi.org/10.1016/j.egypro.2019.04.016>.
- [29] F.G. Alabtah, E. Mahdi, F.F. Eliyan, The use of fiber reinforced polymeric composites in pipelines: A review, *Compos Struct.* 276 (2021). <https://doi.org/10.1016/j.compstruct.2021.114595>.
- [30] P. Feraboli, Composite Materials Strength Determination Within the Current Certification Methodology for Aircraft Structures, *J Aircr.* 46 (2009) 1365–1374. <https://doi.org/10.2514/1.41286>.
- [31] L.J. Love, V. Kunc, O. Rios, C.E. Duty, A.M. Elliott, B.K. Post, R.J. Smith, C.A. Blue, The importance of carbon fiber to polymer additive manufacturing, *J Mater Res.* 29 (2014) 1893–1898. <https://doi.org/10.1557/jmr.2014.212>.
- [32] P. Feraboli, A. Masini, A. Bonfatti, Advanced composites for the body and chassis of a production high performance car, *International Journal of Vehicle Design.* 44 (2007) 233–246. <https://doi.org/10.1504/IJVD.2007.013641>.
- [33] W.K. Goertzen, M.R. Kessler, Dynamic mechanical analysis of carbon/epoxy composites for structural pipeline repair, *Compos B Eng.* 38 (2007) 1–9. <https://doi.org/10.1016/j.compositesb.2006.06.002>.

- [34] H.S. da Costa Mattos, J.M.L. Reis, L.M. Paim, M.L. da Silva, F.C. Amorim, V.A. Perrut, Analysis of a glass fibre reinforced polyurethane composite repair system for corroded pipelines at elevated temperatures, *Compos Struct.* 114 (2014) 117–123. <https://doi.org/10.1016/j.compstruct.2014.04.015>.
- [35] Z. Li, X. Jiang, H. Hopman, L. Zhu, Z. Liu, External surface cracked offshore steel pipes reinforced with composite repair system subjected to cyclic bending: An experimental investigation, *Theoretical and Applied Fracture Mechanics.* 109 (2020). <https://doi.org/10.1016/j.tafmec.2020.102703>.
- [36] M. Shamsuddoha, L.P. Djukic, M.M. Islam, T. Aravinthan, A. Manalo, Mechanical and thermal properties of glass fiber–vinyl ester resin composite for pipeline repair exposed to hot-wet conditioning, *J Compos Mater.* 51 (2017) 1605–1617. <https://doi.org/10.1177/0021998316661869>.
- [37] N. Saeed, H. Ronagh, A. Virk, Composite repair of pipelines, considering the effect of live pressure-analytical and numerical models with respect to ISO/TS 24817 and ASME PCC-2, *Compos B Eng.* 58 (2014) 605–610. <https://doi.org/10.1016/j.compositesb.2013.10.035>.
- [38] A. Eidaninezhad, P. Ziyaei, A. Zare, An overview of marine pipeline repair methods, in: 8th International Offshore Industries Conference, Sharif University of Technology, Tehran, 2019.
- [39] International Organization for Standardization, Petroleum, petrochemical and natural gas industries - Composite repairs for pipework - Qualification and design, installation, testing and inspection, 2017. [www.iso.org](http://www.iso.org).
- [40] ASME, Repair of Pressure Equipment and Piping, American Society of Mechanical Engineers, 2022. <http://cstools.asme.org>.
- [41] B.E. Sar, S. Fréour, P. Davies, F. Jacquemin, Coupling moisture diffusion and internal mechanical states in polymers - A thermodynamical approach, *European Journal of Mechanics, A/Solids.* 36 (2012) 38–43. <https://doi.org/10.1016/j.euromechsol.2012.02.009>.

- [42] F.B. Boukhoulda, L. Guillaumat, J.L. Lataillade, E. Adda-Bedia, A. Lousdad, Aging-impact coupling based analysis upon glass/polyester composite material in hygrothermal environment, *Mater Des.* 32 (2011) 4080–4087. <https://doi.org/10.1016/j.matdes.2011.03.009>.
- [43] S. Sugiman, A.D. Crocombe, I.A. Aschroft, Experimental and numerical investigation of the static response of environmentally aged adhesively bonded joints, *Int J Adhes Adhes.* 40 (2013) 224–237. <https://doi.org/10.1016/j.ijadhadh.2012.08.007>.
- [44] M. Dawood, S. Rizkalla, Environmental durability of a CFRP system for strengthening steel structures, *Constr Build Mater.* 24 (2010) 1682–1689. <https://doi.org/10.1016/j.conbuildmat.2010.02.023>.
- [45] A. Altalmas, A. el Refai, F. Abed, Bond degradation of basalt fiber-reinforced polymer (BFRP) bars exposed to accelerated aging conditions, *Constr Build Mater.* 81 (2015) 162–171. <https://doi.org/10.1016/j.conbuildmat.2015.02.036>.
- [46] M. Lettieri, M. Frigione, Effects of humid environment on thermal and mechanical properties of a cold-curing structural epoxy adhesive, *Constr Build Mater.* 30 (2012) 753–760. <https://doi.org/10.1016/j.conbuildmat.2011.12.077>.
- [47] Y. Joliff, L. Belec, J.F. Chailan, Modified water diffusion kinetics in an unidirectional glass/fibre composite due to the interphase area: Experimental, analytical and numerical approach, *Compos Struct.* 97 (2013) 296–303. <https://doi.org/10.1016/j.compstruct.2012.09.044>.
- [48] L.F.M. da Silva, R.J.C. Carbas, G.W. Critchlow, M.A.V. Figueiredo, K. Brown, Effect of material, geometry, surface treatment and environment on the shear strength of single lap joints, *Int J Adhes Adhes.* 29 (2009) 621–632. <https://doi.org/10.1016/j.ijadhadh.2009.02.012>.
- [49] X. Jiang, H. Kolstein, F.S.K. Bijlaard, Moisture diffusion in glass-fiber-reinforced polymer composite bridge under hot/wet environment, *Compos B Eng.* 45 (2013) 407–416. <https://doi.org/10.1016/j.compositesb.2012.04.067>.

- [50] T.-C. Nguyen, Y. Bai, X.-L. Zhao, R. Al-Mahaidi, Effects of ultraviolet radiation and associated elevated temperature on mechanical performance of steel/CFRP double strap joints, *Compos Struct.* 94 (2012) 3563–3573. <https://doi.org/10.1016/j.compstruct.2012.05.036>.
- [51] D. Borrie, H.B. Liu, X.L. Zhao, R.K. Singh Raman, Y. Bai, Bond durability of fatigued CFRP-steel double-lap joints pre-exposed to marine environment, *Compos Struct.* 131 (2015) 799–809. <https://doi.org/10.1016/j.compstruct.2015.06.021>.
- [52] E. Poodts, G. Minak, A. Zucchelli, Impact of sea-water on the quasi static and fatigue flexural properties of GFRP, *Compos Struct.* 97 (2013) 222–230. <https://doi.org/10.1016/j.compstruct.2012.10.021>.
- [53] A. Siriruk, D. Penumadu, Degradation in fatigue behavior of carbon fiber-vinyl ester based composites due to sea environment, *Compos B Eng.* 61 (2014) 94–98. <https://doi.org/10.1016/j.compositesb.2014.01.030>.
- [54] P.S.C. Vieira, G.A.S. da Silva, B.J. Lopes, J.R.M. D’Almeida, A.H. da Silva, D.C.T. Cardoso, Hygrothermal aging of steel/FRP pipe repair systems: A literature review, *International Journal of Pressure Vessels and Piping.* 201 (2023). <https://doi.org/10.1016/j.ijpvp.2022.104881>.
- [55] N. Tual, N. Carrere, P. Davies, T. Bonnemains, E. Lolive, Characterization of sea water ageing effects on mechanical properties of carbon/epoxy composites for tidal turbine blades, *Compos Part A Appl Sci Manuf.* 78 (2015) 380–389. <https://doi.org/10.1016/j.compositesa.2015.08.035>.
- [56] R. Guo, G. Xian, F. Li, C. Li, B. Hong, Hygrothermal resistance of pultruded carbon, glass and carbon/glass hybrid fiber reinforced epoxy composites, *Constr Build Mater.* 315 (2022). <https://doi.org/10.1016/j.conbuildmat.2021.125710>.
- [57] N. Sateesh, P.S. Rao, D.V. Ravishanker, K. Satyanarayana, Effect of Moisture on GFRP Composite Materials, *Mater Today Proc.* 2 (2015) 2902–2908. <https://doi.org/10.1016/j.matpr.2015.07.252>.
- [58] I.F. Soykok, O. Sayman, A. Pasinli, Effects of hot water aging on failure behavior of mechanically fastened glass fiber/epoxy composite joints,

- Compos B Eng. 54 (2013) 59–70.  
<https://doi.org/10.1016/j.compositesb.2013.04.073>.
- [59] A.P. Chakraverty, U.K. Mohanty, S.C. Mishra, A. Satapathy, Sea Water Ageing of GFRP Composites and the Dissolved salts, IOP Conf Ser Mater Sci Eng. 75 (2015) 012029. <https://doi.org/10.1088/1757-899X/75/1/012029>.
- [60] A. Toscano, G. Pitarresi, M. Scafidi, M. di Filippo, G. Spadaro, S. Alessi, Water diffusion and swelling stresses in highly crosslinked epoxy matrices, Polym Degrad Stab. 133 (2016) 255–263.  
<https://doi.org/10.1016/j.polymdegradstab.2016.09.004>.
- [61] S. Alessi, D. Conduruta, G. Pitarresi, C. Dispenza, G. Spadaro, Accelerated ageing due to moisture absorption of thermally cured epoxy resin/polyethersulphone blends. Thermal, mechanical and morphological behaviour, Polym Degrad Stab. 96 (2011) 642–648.  
<https://doi.org/10.1016/j.polymdegradstab.2010.12.027>.
- [62] L.R. Xu, A. Krishnan, H. Ning, U. Vaidya, A seawater tank approach to evaluate the dynamic failure and durability of E-glass/vinyl ester marine composites, Compos B Eng. 43 (2012) 2480–2486.  
<https://doi.org/10.1016/j.compositesb.2011.08.039>.
- [63] A. Afshar, M. Alkhader, C.S. Korach, F.P. Chiang, Effect of long-term exposure to marine environments on the flexural properties of carbon fiber vinylester composites, Compos Struct. 126 (2015) 72–77.  
<https://doi.org/10.1016/j.compstruct.2015.02.008>.
- [64] G. Dell’Anno, R. Lees, Effect of water immersion on the interlaminar and flexural performance of low cost liquid resin infused carbon fabric composites, Compos B Eng. 43 (2012) 1368–1373.  
<https://doi.org/10.1016/j.compositesb.2011.08.037>.
- [65] R. Pal, H.N. Narasimha Murthy, M. Sreejith, K.R. Vishnu Mahesh, M. Krishna, S.C. Sharma, Effect of laminate thickness on moisture diffusion of polymer matrix composites in artificial seawater ageing, Front Mater Sci. 6 (2012) 225–235. <https://doi.org/10.1007/s11706-012-0177-1>.

- [66] A.M. Visco, N. Campo, P. Cianciafara, Comparison of seawater absorption properties of thermoset resins based composites, *Compos Part A Appl Sci Manuf.* 42 (2011) 123–130. <https://doi.org/10.1016/j.compositesa.2010.10.009>.
- [67] A. Naceri, An analysis of moisture diffusion according to Fick's law and the tensile mechanical behavior of a glass-fabric-reinforced composite, *Mechanics of Composite Materials.* 45 (2009) 331–336. <https://doi.org/10.1007/s11029-009-9080-y>.
- [68] Z.A. Oguz, A. Erklig, Ö.Y. Bozkurt, Degradation of hybrid aramid/glass/epoxy composites hydrothermally aged in distilled water, *J Compos Mater.* 55 (2021) 2043–2060. <https://doi.org/10.1177/0021998320984237>.
- [69] L.C. Bank, T.R. Gentry, B.P. Thompson, J.S. Russell, Model Specification for Composites for Civil Engineering Structures, *Transp Res Rec.* 1814 (2002) 227–236.
- [70] T. Peret, A. Clement, S. Freour, F. Jacquemin, Numerical transient hygro-elastic analyses of reinforced Fickian and non-Fickian polymers, *Compos Struct.* 116 (2014) 395–403. <https://doi.org/10.1016/j.compstruct.2014.05.026>.
- [71] W.P. da Silva, C.M.D.P.S. E Silva, V.S.O. Farias, A.G.B. Lima, Effect of the geometry on the description of the water absorption by composite materials using diffusion models, *Materwiss Werksttech.* 42 (2011) 747–752. <https://doi.org/10.1002/mawe.201100800>.
- [72] M. Ounaies, M. Harchay, F. Dammak, H. ben Daly, Prediction of hygrothermal behavior of polyester/glass fiber composite in dissymmetric absorption, *J Compos Mater.* 52 (2018) 4001–4007. <https://doi.org/10.1177/0021998318773458>.
- [73] J.C. Arnold, S.M. Alston, F. Korkees, An assessment of methods to determine the directional moisture diffusion coefficients of composite materials, *Compos Part A Appl Sci Manuf.* 55 (2013) 120–128. <https://doi.org/10.1016/j.compositesa.2013.08.012>.

- [74] M.D. Placette, X. Fan, J.H. Zhao, D. Edwards, Dual stage modeling of moisture absorption and desorption in epoxy mold compounds, *Microelectronics Reliability*. 52 (2012) 1401–1408. <https://doi.org/10.1016/j.microrel.2012.03.008>.
- [75] N. Coniglio, K. Nguyen, R. Kurji, E. Gamboa, Characterizing water sorption in 100% solids epoxy coatings, *Prog Org Coat*. 76 (2013) 1168–1177. <https://doi.org/10.1016/j.porgcoat.2013.03.011>.
- [76] Y. Chen, J.F. Davalos, I. Ray, Durability Prediction for GFRP Reinforcing Bars Using Short-Term Data of Accelerated Aging Tests, *Journal of Composites for Construction*. 10 (2006) 279–286. [https://doi.org/10.1061/\(ASCE\)1090-0268\(2006\)10:4\(279\)](https://doi.org/10.1061/(ASCE)1090-0268(2006)10:4(279)).
- [77] L. Sang, C. Wang, Y. Wang, W. Hou, Effects of hydrothermal aging on moisture absorption and property prediction of short carbon fiber reinforced polyamide 6 composites, *Compos B Eng*. 153 (2018) 306–314. <https://doi.org/10.1016/j.compositesb.2018.08.138>.
- [78] Z. Wang, X.L. Zhao, G. Xian, G. Wu, R.K. Singh Raman, S. Al-Saadi, A. Haque, Long-term durability of basalt- and glass-fibre reinforced polymer (BFRP/GFRP) bars in seawater and sea sand concrete environment, *Constr Build Mater*. 139 (2017) 467–489. <https://doi.org/10.1016/j.conbuildmat.2017.02.038>.
- [79] Y. Chen, J.F. Davalos, I. Ray, H.Y. Kim, Accelerated aging tests for evaluations of durability performance of FRP reinforcing bars for concrete structures, *Compos Struct*. 78 (2007) 101–111. <https://doi.org/10.1016/j.compstruct.2005.08.015>.
- [80] N. Guerhazi, A. ben Tarjem, I. Ksouri, H.F. Ayedi, On the durability of FRP composites for aircraft structures in hygrothermal conditioning, *Compos B Eng*. 85 (2013) 294–304. <https://doi.org/10.1016/j.compositesb.2015.09.035>.
- [81] X. Jiang, H. Kolstein, F.S.K. Bijlaard, Moisture diffusion and hygrothermal aging in pultruded fibre reinforced polymer composites of

- bridge decks, *Mater Des.* 37 (2012) 304–312. <https://doi.org/10.1016/j.matdes.2012.01.017>.
- [82] B. Benmokrane, P. Wang, T. Minh Ton-That, H. Rahman, J.-F. Robert, Durability of Glass Fiber-Reinforced Polymer Reinforcing Bars in Concrete Environment, *Journal of Composites for Construction.* 6 (2002) 143–153. <https://doi.org/10.1061/ASCE1090-026820026:3143>.
- [83] F. Guo, S. Al-Saadi, R.K. Singh Raman, X.L. Zhao, Durability of fiber reinforced polymer (FRP) in simulated seawater sea sand concrete (SWSSC) environment, *Corros Sci.* 141 (2018) 1–13. <https://doi.org/10.1016/j.corsci.2018.06.022>.
- [84] G. Nossoni, Modeling the Corrosion Rate of Steel Reinforcement in FRP-Wrapped Concrete, *Journal of Composites for Construction.* 20 (2016). [https://doi.org/10.1061/\(asce\)cc.1943-5614.0000625](https://doi.org/10.1061/(asce)cc.1943-5614.0000625).
- [85] I. Panaitescu, T. Koch, V.M. Archodoulaki, Effects of temperature, humidity and automotive fluids exposure on glass fiber/polyurethane composites, *Polym Compos.* 40 (2019) 2357–2367. <https://doi.org/10.1002/pc.25094>.
- [86] N. Guerhazi, K. Elleuch, H.F. Ayedi, The effect of time and aging temperature on structural and mechanical properties of pipeline coating, *Mater Des.* 30 (2009) 2006–2010. <https://doi.org/10.1016/j.matdes.2008.09.003>.
- [87] A.P. Chakraverty, U.K. Mohanty, S.C. Mishra, A. Satapathy, Sea water ageing of GFRP composites and the dissolved salts, in: *IOP Conf Ser Mater Sci Eng*, Institute of Physics Publishing, 2015. <https://doi.org/10.1088/1757-899X/75/1/012029>.
- [88] J.M. Sousa, J.R. Correia, J. Gonilha, S. Cabral-Fonseca, J.P. Firmo, T. Keller, Durability of adhesively bonded joints between pultruded GFRP adherends under hygrothermal and natural ageing, *Compos B Eng.* 158 (2019) 475–488. <https://doi.org/10.1016/j.compositesb.2018.09.060>.

- [89] M.A.G. Silva, B.S. da Fonseca, H. Biscaia, On estimates of durability of FRP based on accelerated tests, *Compos Struct.* 116 (2014) 377–387. <https://doi.org/10.1016/j.compstruct.2014.05.022>.
- [90] E.S. Barrera, A.V. Fantin, D.P. Willemann, M.E. Benedet, A. Albertazzi Gonçalves, Multiple-aperture one-shot shearography for simultaneous measurements in three shearing directions, *Opt Lasers Eng.* 111 (2018) 86–92. <https://doi.org/10.1016/j.optlaseng.2018.07.018>.
- [91] R. Sirohi, Shearography and its applications – a chronological review, *Light: Advanced Manufacturing.* 3 (2022) 1. <https://doi.org/10.37188/lam.2022.001>.
- [92] A.R. al Jabri, K.M. Abedin, S.M.M. Rahman, High spatial-resolution digital phase-stepping shearography, *J Imaging.* 7 (2021). <https://doi.org/10.3390/jimaging7100192>.
- [93] Laser Technology Inc., Our NDT Technology, (n.d.). <https://www.laserndt.com/ndt-technology/> (accessed March 25, 2023).
- [94] A. Alves, Inspeção com shearografia em corpos de prova tubulares reparados com material compósito - estudo de caso para dimensionamento de defeitos, *ABENDI.* (2020) 36–45.
- [95] M.E. Benedet, A.V. Fantin, D.P. Willemann, A.A. Gonçalves Júnior, C.R. Schmitz, A.L.F.S. d’Almeida, S.D. Soares, L.D.M. Lana, V.A. Perrut, The use of Shearography technique to evaluate polymeric composite repairs - case study, *Matéria (Rio de Janeiro).* 22 (2017). <https://doi.org/10.1590/s1517-707620170002.0241>.
- [96] F.J. Macedo, M.E. Benedet, A.V. Fantin, D.P. Willemann, F.A.A. da Silva, A. Albertazzi, Inspection of defects of composite materials in inner cylindrical surfaces using endoscopic shearography, *Opt Lasers Eng.* 104 (2018) 100–108. <https://doi.org/10.1016/j.optlaseng.2017.06.005>.
- [97] Á. da Silva Paes, D. Pedro Willemann, A. Vieira Fantin, A. Albertazzi Gonçalves Júnior, M. Eduardo Benedet, V. Azevedo Perrut, A. Lúcia Fampa Seabra, S. Damasceno Soares, Estimativa do Tamanho de Defeitos em Tubos de Aço Perfurados e Revestidos Com Material Compósito

- Utilizando Shearografia, in: CONAENDI & IEV, ABENDI, São Paulo, 2014.
- [98] A. Ettemeyer, Laser shearography for inspection of pipelines, *Nuclear Engineering and Design*. 160 (1996) 237–240. [https://doi.org/10.1016/0029-5493\(95\)01103-X](https://doi.org/10.1016/0029-5493(95)01103-X).
- [99] C.Y. Chang, K. Srinivasan, W.C. Wang, G.P. Ganapathy, D.R. Vincent, N. Deepa, Quality assessment of tire shearography images via ensemble hybrid faster region-based convnets, *Electronics (Switzerland)*. 9 (2020). <https://doi.org/10.3390/electronics9010045>.
- [100] M.Y. Yusof, T.M. Loganathan, I. Burhan, W.S.W. Abdullah, M.N.I. Mohamed, I.M.Z. Abidin, N. Zakaria, Shearography Technique on Inspection of Advanced Aircraft Composite Material, in: *IOP Conf Ser Mater Sci Eng*, Institute of Physics Publishing, 2019. <https://doi.org/10.1088/1757-899X/554/1/012009>.
- [101] M. Georges, C. Srajbr, P. Menner, J. Koch, A. Dillenz, Thermography and Shearography Inspection of Composite Hybrid Sandwich Structure Made of CFRP and GFRP Core and Titanium Skins, in: *The 18th International Conference on Experimental Mechanics*, MDPI, Basel Switzerland, 2018: p. 484. <https://doi.org/10.3390/ICEM18-05384>.
- [102] B.C.F. Oliveira, A.A. Seibert, D. Staub, A. Albertazzi, Square-pulse shearography inspections of metallic parts repaired with a glass fiber reinforced polymer using pressure, radiation, vibration, and induction loading methods, *International Journal of Pressure Vessels and Piping*. 187 (2020). <https://doi.org/10.1016/j.ijpvp.2020.104187>.
- [103] Á. da Silva Paes, Proposta de procedimento para estimativa do tamanho de defeitos em tubos de aço perfurados e revestidos com materiais compósitos utilizando shearografia, UFSC, 2013.
- [104] N. Tao, A. Anisimov, M. Elenbaas, R.M. Groves, Shearography non-destructive testing of a composite ship hull section subjected to multiple impacts, in: A. Vassilopoulos, V. Michaud (Eds.), *Proceedings of the 20th European Conference on Composite Materials - Composites Meet*

- Sustainability: Vol 3 - Characterization, EPFL Lausanne, Composite Construction Laboratory, Lausanne, 2022.  
[https://doi.org/https://doi.org/10.5075/epfl-298799\\_978-2-9701614-0-0](https://doi.org/https://doi.org/10.5075/epfl-298799_978-2-9701614-0-0).
- [105] R. Růžek, R. Lohonka, J. Jironč, Ultrasonic C-scan and shearography NDI techniques evaluation of impact defects identification, *NDT and E International*. 39 (2006) 132–142.  
<https://doi.org/10.1016/j.ndteint.2005.07.012>.
- [106] F.P. García Márquez, A.M. Peco Chacón, A review of non-destructive testing on wind turbines blades, *Renew Energy*. 161 (2020) 998–1010.  
<https://doi.org/10.1016/j.renene.2020.07.145>.
- [107] H. Al-Rizzo, W. Alobaidi, E. Sandgren, A Survey on Benchmark Defects Encountered in the Oil Pipe Industries, *Int J Sci Eng Res*. 6 (2015) 844–853. <http://www.ijser.org>.
- [108] F. Honarvar, A. Varvani-Farahani, A review of ultrasonic testing applications in additive manufacturing: Defect evaluation, material characterization, and process control, *Ultrasonics*. 108 (2020).  
<https://doi.org/10.1016/j.ultras.2020.106227>.
- [109] ASTN, *Nondestructive Testing Handbook, Vol. 7: Ultrasonic Testing (UT)*, 3rd ed., 2007.
- [110] A. Yamani, M. Bettayeb, U. Qidwai, C.H. Chen, GUI-based toolbox in matlab for deconvolution of ultrasonic nondestructive testing signals for defect identification, in: *AIP Conf Proc*, AIP, 2000: pp. 757–764.  
<https://doi.org/10.1063/1.1306123>.
- [111] M. Ma, H. Cao, M. Jiang, L. Sun, L. Zhang, F. Zhang, Q. Sui, A. Tian, J. Liang, L. Jia, High precision detection method for delamination defects in carbon fiber composite laminates based on ultrasonic technique and signal correlation algorithm, *Materials*. 13 (2020).  
<https://doi.org/10.3390/ma13173840>.
- [112] K. Berketis, D. Tzetzis, P.J. Hogg, Impact damage detection and degradation monitoring of wet GFRP composites using noncontact

- ultrasonics, *Polym Compos.* 30 (2009) 1043–1049. <https://doi.org/10.1002/pc.20652>.
- [113] F. Schadow, D. Brackrock, M. Gaal, T. Heckel, Ultrasonic Inspection and Data Analysis of Glass-and Carbon-Fibre-Reinforced Plastics, in: *Procedia Structural Integrity*, Elsevier B.V., 2017: pp. 299–306. <https://doi.org/10.1016/j.prostr.2017.11.092>.
- [114] J. Chang, C. Zheng, Q.Q. Ni, The ultrasonic wave propagation in composite material and its characteristic evaluation, *Compos Struct.* 75 (2006) 451–456. <https://doi.org/10.1016/j.compstruct.2006.04.040>.
- [115] R.D. Adams, P. Cawley, Defect types and non-destructive testing techniques for composites and bonded joints, *Constr Build Mater.* 3 (1989) 170–183. [https://doi.org/10.1016/0950-0618\(89\)90011-1](https://doi.org/10.1016/0950-0618(89)90011-1).
- [116] R. Tamborrino, D. Palumbo, U. Galietti, P. Aversa, S. Chiozzi, V.A.M. Luprano, Assessment of the effect of defects on mechanical properties of adhesive bonded joints by using non destructive methods, *Compos B Eng.* 91 (2016) 337–345. <https://doi.org/10.1016/j.compositesb.2016.01.059>.
- [117] M. Kersemans, E. Verboven, J. Segers, S. Hedayatrasa, W. Van Paepegem, Non-Destructive Testing of Composites by Ultrasound, Local Defect Resonance and Thermography, in: *The 18th International Conference on Experimental Mechanics*, MDPI, Basel Switzerland, 2018: p. 554. <https://doi.org/10.3390/ICEM18-05464>.
- [118] I. Ehrlich, H. Dinnebier, C. Jost, Comparison of impact delaminations in CFRP using different test methods, *Journal of Achievements in Materials and Manufacturing Engineering.* 73 (2015) 128–138.
- [119] P. Li, X. Gao, Y. Luo, H. Kong, Z. Zhao, Z. Zhang, Defect monitoring of CFRP with ultrasonic C-scan method, in: *Adv Mat Res*, 2011: pp. 5343–5348. <https://doi.org/10.4028/www.scientific.net/AMR.243-249.5343>.
- [120] C.C. Tsao, H. Hocheng, Computerized tomography and C-Scan for measuring delamination in the drilling of composite materials using various drills, *Int J Mach Tools Manuf.* 45 (2005) 1282–1287. <https://doi.org/10.1016/j.ijmachtools.2005.01.009>.

- [121] P.D. De Almeida, G.R. Pereira, Phased array inspection of glass fiber reinforced polymers pipeline joints, *Journal of Materials Research and Technology*. 8 (2019) 4736–4740. <https://doi.org/10.1016/j.jmrt.2019.08.020>.
- [122] E.E. Franco, J.M. Meza, F. Buiochi, Measurement of elastic properties of materials by the ultrasonic through-transmission technique medición de las propiedades elásticas de materiales por el método de transmisión ultrasónica, *Dyna (Medellin)*. 78 (2011) 59–64.
- [123] R. Cui, F. Lanza di Scalea, On the identification of the elastic properties of composites by ultrasonic guided waves and optimization algorithm, *Compos Struct*. 223 (2019). <https://doi.org/10.1016/j.compstruct.2019.110969>.
- [124] F. Lionetto, A. Maffezzoli, Polymer characterization by ultrasonic wave propagation, *Advances in Polymer Technology*. 27 (2008) 63–73. <https://doi.org/10.1002/adv.20124>.
- [125] P.D. De Almeida, J.M. Alcoforado Rebello, G.R. Pereira, S.D. Soares, R. Fernandez, Ultrasonic inspection of adhesive joints of composite pipelines, in: *AIP Conf Proc*, American Institute of Physics Inc., 2014: pp. 1069–1076. <https://doi.org/10.1063/1.4864939>.
- [126] Petrobras - CONTEC, Revestimento Externo de Tubulação e Instalações Terrestres, Petrobras CONTEC, Brazil, 2019.
- [127] ASTM International, Standard Practice for Cyclic Salt Fog / UV Exposure of Painted Metal , ( Alternating Exposures in a Fog / Dry Cabinet and a UV / Condensation Cabinet ), 2005. <https://doi.org/10.1520/D5894-10.2>.
- [128] ASTM International, Standard Specification for Reagent Water, 2006. <https://doi.org/10.1520/D1193-99E01>.
- [129] M. Zhang, B. Sun, B. Gu, Accelerated thermal ageing of epoxy resin and 3-D carbon fiber/epoxy braided composites, *Compos Part A Appl Sci Manuf*. 85 (2016) 163–171. <https://doi.org/10.1016/j.compositesa.2016.03.028>.

- [130] ASTM International, Standard Test Method for Moisture Absorption Properties and Equilibrium Conditioning of Polymer Matrix Composite Materials, 2020. [https://doi.org/10.1520/D5229\\_D5229M-20](https://doi.org/10.1520/D5229_D5229M-20).
- [131] ASTM International, Standard Test Method for Water Absorption of Plastics, Cambridge University Press, 2018. [www.astm.org](http://www.astm.org) (accessed March 27, 2023).

# Appendix A

